ULTRA-SENSITIVE AND SELECTIVE WHISPERING GALLERY MODE MICROTOROID CHEMICAL SENSOR

by

Cheng Li

A Dissertation Submitted to the Faculty of the

JAMES C. WYANT COLLEGE OF OPTICAL SCIENCES

In Partial Fulfillment of the Requirements

For the Degree of

DOCTOR OF PHILOSOPHY

In the Graduate College

THE UNIVERSITY OF ARIZONA

2022

THE UNIVERSITY OF ARIZONA
GRADUATE COLLEGE

As members of the Dissertation Committee, we certify that we have read the dissertation prepared by: Cheng Li
titled: Ultra-Sensitive and Selective Whispering Gallery Mode Microtoroid Chemical Sensor

and recommend that it be accepted as fulfilling the dissertation requirement for the Degree of Doctor of Philosophy.

Judith Su — Date: May 1, 2022

Euan Mcleod — Date: May 1, 2022

M. Kolesik — Date: May 2, 2022

Final approval and acceptance of this dissertation is contingent upon the candidate's submission of the final copies of the dissertation to the Graduate College.

I hereby certify that I have read this dissertation prepared under my direction and recommend that it be accepted as fulfilling the dissertation requirement.

Judith Su — Date: May 1, 2022
Judith Su
Dissertation Committee Chair
Optical Sciences

ACKNOWLEDGEMENTS

First and foremost, I would like to thank my advisor, Professor Judith Su, for her help and guidance throughout my PhD research and dissertation. When someone asks me why I decided to pursue a PhD, I would say that my advisor was one of the main factors. She is very nice, has a lot of ideas, and will provide sufficient financial support. She made it possible for me to really put my verbal passion for optics into actual research projects. She would give me opportunities and be willing to create opportunities for me to learn new things and never limited my new thoughts on research. In her busy schedule, she still finds time to discuss and follow up on my projects and make suggestions, just as the laser in the FLOWER system precisely tracks the resonance of the toroid. She has provided me with the chance to participate in interdisciplinary and intergroup project collaborations and to communicate and present at international conferences. She is a great mentor in academics and a good friend in life.

Secondly, I would like to thank Professor Euan McLeod, who could almost be considered as my second advisor during my PhD. His strong theoretical background and extensive knowledge made me discover something new in every meeting and discussion. I still remember one of the discussions in his office at the beginning of my simulation project, where he started from the very basic Maxwell's equations and patiently guided me through the derivation. I am very grateful to this professor couple, whose attitude towards research will be a lifetime benefit to me.

Then, I would like to thank Professor Kolesik for his participation in my comprehensive examination and dissertation defense, and Professor Liang for being the chair of my comprehensive exam committee. I would like to thank the wonderful teachers who taught me at the College of Optics, especially Prof. Masud Mansuripur, Prof. Khanh Kieu, Prof. Jason Jones,

Prof. Mahmoud Fallahi, and Prof. Linran Fan. I have enjoyed my classes here so much that I kept taking classes until my fifth year of PhD hoping to learn more in the ocean of optics.

During my thesis work, I have enjoyed interacting with the other colleagues in my group, Dr. Lei Chen, Dr. Phuong-Diem Nguyen, Dr. Jeffrey Melzer, Adley Gin, Shuang Hao, Sartanee Suebka, Gwangho Choi, Yisha Tang, Chang Ge, Zhouyang Min, etc. In particular, Lei Chen, we have been an excellent team since the early days of my joining the research group. we shared all research resources and often discussed problems until the early morning. My first project and my first published paper also had her significant participation. I would like to thank Adley and Shuang for not only helping me with my research but also for being good workout partners in the gym. Thanks to Chang and Yisha for working together as a small group for gas sensing. Thanks to Sand for constantly providing new solutions and trying them out while working together.

I would also like to thank my friends I have met in Tucson, Zhenye, Yi, Wenhan, Ted, Xianyue, Pengfei, Cheng, and our friendship over the years, sorry I can't list everyone by name. Thank you all for your help and support, for helping me get out of my emotional slump, and for sharing my happiness. Thanks to my long distance supporting friends, He, Junge, Chen, KD, Boston, Shaomin, and everyone in my WeChat groups! Thanks to all of you who live in different time zones and allow me to speak up at any time.

Finally, I would like to thank some special people. I would like to thank my mom, Xiaoxu Cheng, for her endless love, support, and encouragement. I would like to thank my grandfather Weizhou Cheng and my grandmother Yunhua Zu for raising me, never imagining that the spirit of my grandfather, who is a mechanical engineer, would live on in me in another form in the path of science. I am sad that my grandmother could not see me wearing the doctoral suit, I will miss you forever. I am fortunate to have met Xiaodi Xu in 2019 who has lit up my life for the past three

years, thanks to her constant love and care, and thanks to her thousands of hours of classical music harp performances. I wish our photoacoustics could be coupled beautifully in the coming decades. Thanks to my two cats Diana and Bruce for their emotional support and never-tired meowing! They are as much important to me as Schrodinger's cat.

The University of Arizona in Tucson is a quiet and comfortable place to study, and I'm even starting to enjoy the hot summer weather here. This is also a place where I have made some progress in fitness. I am mentally and physically ready for the next phase! I love Tucson, U of A, College of Optics, the memories here, and every one of you. This thesis is dedicated to all of you.

Cheng in Tucson

Apr 11, 2022

DEDICATION

To my mother: Xiaoxu Cheng

To my grandparents: Weizhou Cheng and Yunhua Zu

TABLE OF CONTENTS

LIST OF FIGURES

LIST OF TABLES

LIST OF PUBLICATIONS

[1] **C. Li**, M. H. Teimourpour, E. McLeod, and J. Su, "Enhanced whispering gallery mode sensors," in *Chemical, Biological, Radiological, Nuclear, and Explosives (CBRNE) Sensing XIX*, May 2018, vol. 10629, pp. 79–85. doi: 10.1117/12.2304556.

[2] **C. Li**, L. Chen, E. McLeod, and J. Su, "Dark mode plasmonic optical microcavity biochemical sensor," *Photon. Res.*, vol. 7, no. 8, p. 939, Aug. 2019, doi: 10.1364/PRJ.7.000939.

[3] L. Chen, **C. Li**, Y.-M. Liu, J. Su, and E. McLeod, "Simulating robust far-field coupling to traveling waves in large three-dimensional nanostructured high-Q microresonators," *Photon. Res.*, vol. 7, no. 9, p. 967, Sep. 2019, doi: 10.1364/PRJ.7.000967.

[4] L. Chen, **C. Li**, Y. Liu, J. Su, and E. McLeod, "Three-Dimensional Simulation of Particle-Induced Mode Splitting in Large Toroidal Microresonators," *Sensors*, vol. 20, no. 18, Art. no. 18, Jan. 2020, doi: 10.3390/s20185420.

[5] A. Gin, P. Nguyen, J. Melzer, **C. Li**, J. Su, "Label-free, real-time monitoring of membrane binding events at attomolar concentrations using frequency-locked optical microresonators," (In preparation).

[6] **C. Li**, T. Lohrey, P. Nguyen, Z. Min, Y. Tang, C. Ge, Z. Sercel, E. McLeod, B. Stoltz, and J. Su, "Part-per-trillion trace selective gas detection using frequency locked whispering gallery mode microtoroids," Mar. 2022, doi: 10.26434/chemrxiv-2022-606xv.

[7] **C. Li**, S. Suebka, J. Su, "Temperature calibration of whispering gallery mode biochemical sensor using OFDR," (In preparation).

ABSTRACT

Optical Whispering gallery mode (WGM) microresonators, which benefit from an ultra-high quality (Q) factor and small mode volume to significantly enhance light-matter interaction, stand out from other sensors, and are utilized in a variety of biochemical sensing or physical parameter detection applications. Physical or chemical reactions occurring in the evanescent field of the polymer-treated microtoroid equatorial plane will be translated into variations of the WGM spectra, which will, in turn, be recorded and analyzed through techniques such as frequency locking, balanced detection, and post data processing. The overall platform is known as the Frequency-locked optical whispering evanescent resonator (FLOWER) system. The performance and characteristics of ultra-sensitive and selective WGM gas sensors are evaluated and demonstrated in this dissertation. Two approaches to further improve the system are proposed, one based on plasmonic near-field enhancement to improve the sensitivity and the other on a fiber metrology method using Rayleigh backscattering to eliminate the thermal noise of the sensing system. Finally, another sensing application using the dual-FLOWER system for particle shape analysis is introduced.

1 INTRODUCTION

1.1 Whispering Gallery Mode microcavity history and application

On the well-known Echo Wall at the Temple of Heaven in Beijing, China, two people whispering sideways to the wall can hear each other very clearly even when they are far apart (Fig 1.1). The principle is that sound waves can be continuously reflected on a curved and smooth wall with little loss, so that sound can travel a long distance along the wall. This effect is known as whispering gallery mode (WGM) in the field of acoustics.[1]–[3] Similar to the reflection of sound waves on a wall, total internal reflection (TIR) occurs at the boundary between the two media when light is incident from a light-dense medium to a thinner medium with a sufficiently large angle of incidence. An optical whispering gallery mode then appears at the interface of the curved high-refractive-index medium. At the closed cavity boundary, the light can be trapped inside the cavity to maintain a stable traveling wave transmission pattern.

Figure 1.1. Echo Wall of the Temple of Heaven in Beijing.

In 1977, Ashkin et al. first observed the radiation pressure enhancement effect caused by the WGM in an optical tweezer experiment manipulating a tiny spherical water droplet. [4] In 1980, Professor Chang's group at Yale University directly detected the resonance peaks corresponding to the high-Q WGM in the fluorescence spectra of a dye-impregnated polystyrene microsphere. [5] However, the instability of droplets limits the further development of the optical WGM. It was until 1989 that Braginsky et al. in Russia successfully fabricated a stable solid glass microsphere cavity by fusing a glass fiber and demonstrated a Q factor of up to 10^8 in a $150\ \mu m$ diameter sphere. [6] The relatively simple fabrication method and stability of the cavity were rapidly promoted, and a large number of experimental research groups were devoted to the field of WGM. In 1992, McCall et al prepared a microdisk cavity on a semiconductor chip, further reducing the size and dimension of the microcavity to achieve a low-threshold laser with continuous optical pumping and electrical injection, starting the development of an integrated photonics device in the whispering gallery mode. [7]

Although traditional Fabry-Perot (FP) cavities can also achieve high quality factors and are widely used in many fields. Their large cavity sizes, high cost of high reflectivity mirrors, and the need for complex stabilization devices all severely limit the use of FP cavities. The all-solid medium whispering gallery mode microcavity supports a very stable high-Q resonance mode and it also has the advantages of small size and convenient fabrication, attracting more and more people to join the research of whispering gallery mode microcavity. With the development of modern micro-nano processing technology and the advancement in material fabrication methods, the whispering gallery mode has been implemented in microcavities of various materials, including various glasses, polymers, crystals, and semiconductors, and the shape of the cavity is also varied, such as spherical, toroidal, polygonal cylindrical, etc.

The high Q of WGM and its ability to be integrated on a chip gives it great potential for many optical applications, such as efficient filters, highly sensitive sensors, low threshold lasers, nonlinear effects[8], signal delayers, etc. In this regard, Vahala's group at Caltech has done extensive breakthrough works, proposing low-threshold Raman lasers [9], [10], single-molecule detection[11], and other applications for the first time. These cavities can be fabricated using standard semiconductor processes[12], [13], allowing for efficient and accurate mass production of not only individual high-quality cavities but also arrays of inter-coupled cavities. It is interesting to note that the whispering gallery mode can also be interconnected with other optoelectronic devices via waveguides, which are expected to be used for practical applications such as high-speed optical signal processing and environmental detection. [14]–[16]

On the other hand, due to the very small volume of the microcavity mode, even a single photon can generate a super intense electric field in the cavity and can interact strongly with other physical systems.[17] Studies on cavity optomechanics and cavity quantum electrodynamics (QED) have demonstrated coherent photon-atom and photon-phonon interactions.[18] Using these coherent interactions, quantum states can be transmitted to each other in different physical systems, promising applications for the storage and manipulation of quantum states. The strong interactions between light and atoms or media in microcavities can be used to realize nonlinear optical effects at the single-photon scale.

This dissertation is mainly focusing on the WGM sensing application and its sensitivity improvement. Due to the high Q factor, the disturbance of the external environment will cause a significant change in the position of the spectral lines in the WGM microcavity, which can be easily observed, thus enabling the detection of some specific parameters. For the optical mode in the microcavity, the majority of energy is confined within the dielectric cavity, and there is a part

of energy in the environment outside the microcavity (air or liquid, etc.), which we call the evanescent field of the WGM. This part of the energy is distributed on the outer surface of the microcavity with a few hundred nanometers tail. When the external ambient changes or nanoparticles or biomolecules adhere to the surface of the microcavity, the frequency shift of the resonance mode is generated from the evanescent field interaction.

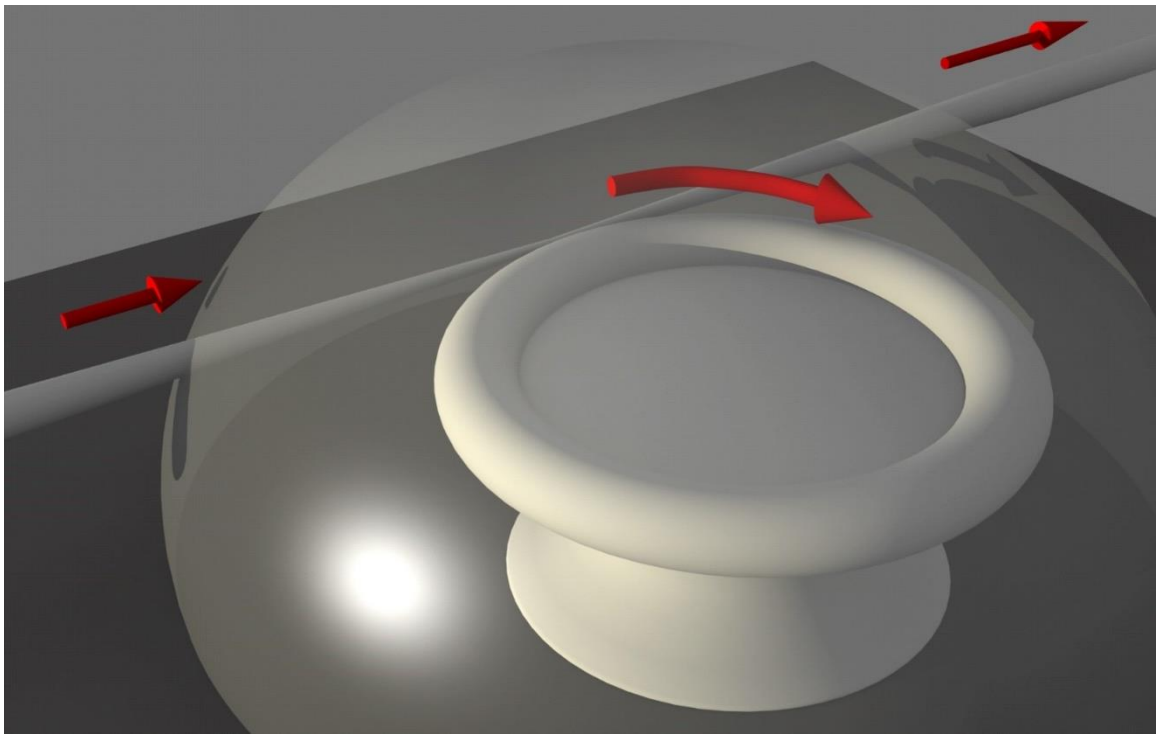

Figure 1.2. Schematic of tapered fiber coupled to a microtoroid.

A schematic of a typical whispering gallery mode biosensor is given in Fig. 1.2. The microcavity and waveguide are immersed in a specific liquid environment that contains the biomolecules to be detected. This type of microcavity requires surface functionalization to allow the biomolecules to be attracted to the surface of the microcavity. The possibility of using microsphere cavities to detect protein molecules was already achieved in 2002 [19] and was theoretically predicted to enable the detection of single protein molecules [20]. In 2008, Vollmer

et al [80] utilized a glass microsphere to experimentally detect a single virus molecule with a radius of approximately 47 nm and a mass of $5.2 \times 10^{-16} g$, as inferred from the measured frequency shift of WGM. In 2011, the Vahala group at Caltech further improved the detection sensitivity by using a high-Q microtoroid cavity, enabling the detection of single molecules with a radius of 12.5 nm. [21] Further, with the combination of laser frequency locking, balanced detection, and data processing techniques to reduce the noise level of the WGM sensing system, Su reported in her PhD study on the detection of a wide range of nanoscale objects, from nanoparticles with a radius of 100 to 2.5 nm, to exosomes, ribosomes, and single protein molecules (mouse immunoglobulin G and human interleukin-2). [22]

In this work, the same frequency-locked system is continued to be implemented in the field of gas sensing to achieve selective gas detection at very low concentrations. In addition, two methods to improve the system are proposed, one is a method to enhance sensitivity based on the near-field enhancement of the plasmonic, and the other is a fiber optical metrology technique to calibrate or eliminate the thermal noise of the WGM sensor. Finally, another sensing application for particle shape analysis using the WGM sensor has been proposed.

1.2 Chapter overview and collaborative work

The results presented by the author in this dissertation were done in large part in collaboration with his colleagues. The results of each chapter are listed below, with the relative contributions noted.

Chapter 2 provides a detailed discussion on the theory part of the WGM microtoroid, from the wave equation to perturbation theory. The Finite Element Method (FEM) and boundary

solution for solving mode inside the microtoroid cavity are explained. The simulation methods and results compared to the analytical solutions are present. Coupled mode theory (CMT) as an efficient method for analyzing electromagnetic wave propagation is also introduced. Studying these theories helps readers to have a better understanding of the WGM microcavities used for biochemical sensing. Finally, three dominant sensing mechanisms of WGM are described, including mode shift, mode splitting, and mode broadening. Mode shift is mainly applied in this dissertation, as well as the frequency locking technique, which can greatly enhance the sensitivity and suppress the noise in the experiment.

Chapter 3 discusses a hybrid plasmonic-WGM system for sensitivity enhancement using dark mode. Unlike the bright mode demonstrated in other experiments, the rationally designed lateral dark mode in gold trimer brings higher near-field enhancement without sacrificing the Q. A new figure of merit known as a combined enhancement factor is proposed to quantify the limit of detection and resolution of the hybrid system. Eigenmodes of the gold plasmonic model with different structures are demonstrated, as well as their extinction cross-sections. An entire 3-dimensional model of microtoroid is built in COMSOL using the finite element method (FEM). Finally, the effects of the coupling of the toroid cavity to the plasmonic structure on the sensitivity are analyzed and validated. This chapter has appeared in *Photonics Research* [23] by the author in collaboration with Dr. Lei Chen. In addition, they have developed a wedge model of microtoroid using Floquet boundary condition that can effectively model grating-toroid coupling [24], which can also be used for the simulation of mode splitting [25]. These two projects are not discussed in detail in this dissertation.

Chapter 4 investigates an ultra-high sensitivity and selectivity chemical gas sensor using polymer-treated WGM microtoroid. The chemical synthesis of the coating, the fabrication of the

silica microtoroid on a silicon chip, the coating procedure, the construction and testing of the sensing system, and the post-processing of the data are all covered in detail. Additionally, the author compares and discusses the existing high sensitivity sensing technologies with WGM gas sensors separately. The project is a cross-disciplinary, cross-group collaboration that involves the *Stoltz* group at *Caltech* and the *McLeod* group at *the University of Arizona*. This chapter is submitted to *ACS Applied Materials & Interfaces* and *Chemrxiv*. [26]

Chapter 5 describes a temperature drift noise correction method using Rayleigh backward scattering following the gas sensing system in Chapter 4. Firstly, the author points out that in existing systems, the non-contact measurement of temperature sensors cannot accurately monitor the actual temperature of the toroid. Then, a temperature measurement method using the fiber contact coupled to the toroid is proposed. This method is known as optical frequency domain reflectometry (OFDR) as well as frequency-modulated continuous wave (FMCW). The author collaborated with his colleague *Sartanee Suebka* to perform the experiment. She was primarily responsible for an ADC circuit design and signal debugging. This work still needs to be further improved for the WGM sensing experiment.

Chapter 6 presents another application of the WGM microcavity for particle shape analysis. This work follows closely the theoretical work in Chapter 3 on the particle polarizability tensor. The authors experimentally constructed a dual-FLOWER system for the observation of two modes with different polarizations interacting with particles. Nanosized gold spheres and rods are measured with different axial dimensions by this method.

2 BASIC THEORY OF WGM MICROTOROID

This section begins by presenting how to obtain the whispering-gallery mode of the toroidal cavity and its important parameters by solving the wave equation. Then the perturbation theory and the analytical solution of the cavity model are investigated. After that, the mode shift sensing mechanism will be described, containing variations of resonance conditions as well as a detailed perturbation theory. In addition, the basics of coupling theory and plasmon will be introduced, together with the basic concepts of nanophotonics and how plasmonic structures enhances WGM detection.

2.1 Basic properties of microcavity

2.1.1 Resonance conditions

In an optical WGM, total internal reflection confines light in a round-shaped cavity in these resonators, causing it to follow the perimeter of the device. When the one roundtrip optical path is approximately equal to an integer multiple of the wavelength (see Eq. 2.1), the phase-matching condition is satisfied. And equally spaced resonant modes are generated, which can be expressed as:

$$m\lambda = 2\pi \mathrm{R}_p n_{eff} \tag{2.1}$$

where λ is the wavelength of the light in free space,

R_p is the principal radius of the microcavity, which is the sum of major radius R and minor radius a,

n_{eff} is the effective refractive index of the resonance mode, it can also be expressed as $n_{eff} = \frac{\beta}{k}$, where β is the propagation constant and k is the wavenumber.

This electromagnetic field mode is called an optical whispering gallery mode.

2.1.2 Quality factor

The important parameter to measure the quality of a resonator is its quality factor (Q) [27], which is defined as:

$$Q = \omega\frac{E}{P} = \omega\tau = \frac{\lambda_{Res}}{\lambda_{FWHM}} = \frac{Re(\lambda_{eigen})}{2\,Im(\lambda_{eigen})} \tag{2.2}$$

where ω is the angular frequency of the mode, E is the energy of the light field in the cavity, P is the energy loss rate, τ is the lifetime of the photon of the corresponding mode, λ_{Res} is the resonance wavelength and λ_{FWHM} is the linewidth.

In terms of energy, a higher Q means a lower energy dissipation and a longer photon lifetime. And from a spectral point of view, higher quality factors correspond to narrower resonances, whose central resonance frequency can be more precisely determined and tracked[17], [28]–[30]. The linewidth can also be obtained from the eigenvalue solution of the resonator, i.e. $\lambda_{FWHM} = 2\,Im(\lambda_{eigen})$. Obviously, the higher the Q-factor, the stronger the interaction between the confined light field and the material, otherwise the interaction will be weaker.

Back to the energy perspective, it can be seen from the above Eq. 2.2 that the Q-factor of the whispering gallery mode microcavity is inversely proportional to the energy loss. The total intrinsic loss is mainly composed of radiation loss, absorption loss, and scattering loss as follows:

$$\frac{1}{Q_{int}} = \frac{1}{Q_{rad}} + \frac{1}{Q_{abs}} + \frac{1}{Q_{sca}} \tag{2.3}$$

The radiation loss (Q_{rad}) comes from the tunneling probability of the light when it is totally reflected on the surface of the curved medium. Q_{rad} increases exponentially with R. When the cavity is large enough, radiation loss is negligible. Absorption loss (Q_{abs}) originates from the absorption of electromagnetic waves by the dielectric material that constitutes the microcavity and its surroundings, and Q_{abs} are not the same at different wavelengths. Scattering loss (Q_{sca}) is derived from the surface roughness of the microcavities during fabrication and the internal defects of the medium. They all scatter light and cause losses. This loss can be reduced with the CO_2 laser reflowing process during the microcavity fabrication.

In addition to the intrinsic losses of the microcavity, it is necessary to apply external coupling devices, such as taper fiber and waveguide, to stimulate and collect the whispering gallery mode in the experiment, so additional losses will be introduced, corresponding to Q_{ext}. The Q-factor obtained in the experimental measurement is:

$$\frac{1}{Q_{tot}} = \frac{1}{Q_{int}} + \frac{1}{Q_{ext}} \tag{2.4}$$

In general, the coupling device can ensure effective coupling, the introduced losses are very small. So, the microcavities can still maintain high Q, which enables precision resonance tracking.

2.1.3 Mode volume of microtoroids

In many applications, in addition to considering the lifetime of photons, mode volume (V_m) is also a very important parameter, which is corresponding to the spatial confinement of the mode. Mode volume can be expressed as:

$$V_m = \int_V \frac{\varepsilon_r \, |\boldsymbol{E}_0|^2 dV}{\varepsilon_r |\boldsymbol{E}_0|^2_{max}} \tag{2.5}$$

where $\mathbf{E}_0$ is the electric field for an unperturbed WGM, $|\mathbf{E}_0|^2_{max}$ is the maximum intensity within the unperturbed toroid, ε_r is the dielectric constant of silica[31] which is the square of the material refractive index. This formula integrates over all space including the evanescent field region. One of the calculation methods is to calculate the mode area first, i.e. to integrate the electric field intensity over the cross section, and then multiply it by the circumference of the toroid to obtain an approximate result. In the following chapter, the exact solution of the mode volume would be calculated using the finite element method (FEM), i.e. COMSOL Multiphysics.

As one of the important parameters in perturbation theory, mode volume directly affects the light-matter interaction and thus the WGM sensor performance. In short, the smaller the mode volume, the greater the intensity of the local electromagnetic field caused by the same energy light, so the stronger the interaction between light and matter.

2.2 Analytical solutions for the field distribution of the WGM

Using classical electromagnetic theory, we can obtain the field distribution of the whispering gallery mode by solving the Maxwell equations under the specific boundary condition.

Typically, in the Cartesian coordinate system, a wave propagating in the waveguide along the z-direction has the form:

$$\boldsymbol{E}(x,y,z,t) = \boldsymbol{E}(x,y)e^{j(\omega t-\beta z)} \tag{2.6}$$

where $\boldsymbol{k} = \frac{\omega}{c} = \frac{2\pi\nu}{c}$ is the wave vector in free space, $k = |\boldsymbol{k}|$ is the wavenumber, c is the speed of light in a vacuum, ω is the angular frequency, and n is the refractive index of the material, respectively. And β is the propagation constant, appearing as well in the previously mentioned resonance condition (2.1). The electric field can be derived from the Helmholtz equation:

$$\nabla \times (\nabla \times \boldsymbol{E}) - n^2\boldsymbol{k}^2\boldsymbol{E} = 0 \tag{2.7}$$

which corresponds to the eigenvalue $\lambda = -j\beta$.

The electric field propagates mainly along the z-axis, while in the x-y plane it decays rapidly as a function of the cladding radius. Thus, the electric field at the edge of the cladding can be set to zero as a boundary condition.

For the cavity mode analysis in the toroidal coordinate system, the wave propagates in the azimuthal direction **θ** instead of z-direction with the following form:

$$\boldsymbol{E}(r,\phi,\theta,t) = \boldsymbol{E}(r,\phi)e^{j(\omega t-\beta r_{eff}\theta)} \tag{2.8}$$

where r_{eff} is an average radius for the mode in the cross-section ($r-\phi$ plane). The radius r_{eff} is usually located between the principal radius ($R_p = R + a$) and the major radius (R). The corresponding eigenvalue, in this case, would be $\lambda = -j\beta r_{eff}$, the details will be explained later in the COMSOL mode analysis section. In this case, the mode will radiate in the $r-\phi$ plane of the waveguide cross section and a reflection-free boundary condition is necessary to be created.

Here an approximate analytical solution to the mode of the bending fiber will be presented. More details can be found in [32]–[34].

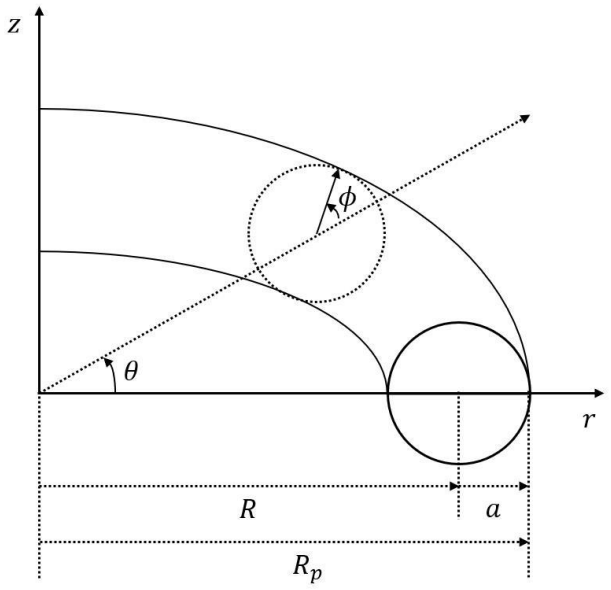

Figure 2.1. Toroidal coordinate system ($\boldsymbol{r}, \boldsymbol{\phi}, \boldsymbol{\theta}$), here $\boldsymbol{R}$ is major radius, $\boldsymbol{a}$ is minor radius, $\boldsymbol{R_p}$ is principal radius

Under the two-dimensional approximation (see Fig 2.1), the vector Maxwell equations are reduced to scalar Helmholtz equations as follows:

$$\nabla^2 \boldsymbol{\Psi} + n^2 \boldsymbol{k}^2 \boldsymbol{\Psi} = 0 \tag{2.9}$$

Similar to how Lamouroux et al. solved Maxwell's equation for mode in a bend fiber, the scalar Helmholtz equation can be simplified to the following wave equation for solving the transverse mode in a toroidal coordinate system[33]:

$$\left\{\frac{\partial^2}{\partial r^2} + \frac{1}{r}\frac{\partial}{\partial r} + \frac{1}{r^2}\frac{\partial^2}{\partial \phi^2} + k^2 n^2\right\}\Psi(r,\phi) + (1 + \delta\frac{r}{a}cos\phi)^{-2}(\frac{1}{4R^2} - \beta^2)\Psi(r,\phi) = 0 \tag{2.10}$$

The wave is propagating in the azimuthal direction, **θ**, with a given eigenfunction

$$\Psi_\theta = (1 + \frac{r}{a} cos\phi)^{-\frac{1}{2}} e^{-jm\theta} \tag{2.11}$$

where m is the azimuthal mode number. It describes the azimuthal variation of the cavity mode fields. Compared to the Eq. 2.8, the intrinsic propagation constant can be defined as $\beta = \frac{m}{r_{eff}}$. And it follows from the relation $n_{eff} = \frac{\beta}{k}$ that the solving of the propagation constant is the solving of the effective refractive index, and each eigenvalue corresponds to a confined eigenmode.

In solving the Eq. 2.10, it is natural to introduce another two integer mode numbers q, l to characterize the cavity mode field. The radial and polar mode numbers q and l determine the type of transverse mode field. In the toroidal microcavity system, the fundamental mode can be represented by q = 0, l = 0. And the inverse aspect ratio is defined as $\delta = \frac{a}{R}$, which will have a great impact on the perturbation expansion of E-field distribution.

Bring Eq. 2.11 back to the Eq. 2.10, the transverse electric (TE) field can be written as:

$$E_\phi = N(1 + \delta \frac{r}{a} cos\phi)^{-\frac{1}{2}} \Psi_E(r, \phi)\, e^{-jm\theta} \tag{2.12}$$

where the TE modes are defined as the mode with no electric field in the direction of propagation, which can be written as follows:

$$\begin{gathered} \boldsymbol{E} \approx \hat{\phi} E_\phi \\ E_r \approx 0 \\ E_\theta \approx 0 \end{gathered} \tag{2.13}$$

Similarly, the transverse magnetic (TM) field with no magnetic field in the direction of propagation can be solved as:

$$H_\phi = N(1+\delta\frac{r}{a}cos\phi)^{-\frac{1}{2}}\,\Psi_H(r,\phi)\,e^{-jm\theta} \tag{2.14}$$

with

$$\begin{aligned} \boldsymbol{H} &\approx \hat{\phi}H_\phi \\ H_r &\approx 0 \\ H_\theta &\approx 0 \end{aligned} \tag{2.15}$$

When δ is small enough ($\delta = \frac{a}{R} < 0.1$), we can write the following wave function in the perturbative form:

$$\Psi = \sum_i \delta^i\,\Psi^{(i)} \tag{2.16}$$

Expanding the result up to the second order. The electric field distribution in the cross section ($r-\phi$ plane) can be expressed as:

$$E(r,\phi) \approx (1+\delta\frac{r}{a}cos\phi)^{-\frac{1}{2}}\left[\Psi^{(0)}(r,\phi) + \delta\Psi^{(1)}(r,\phi) + \delta^2\Psi^{(2)}(r,\phi)\right] \tag{2.17}$$

After solving for the wave functions of each order and bringing them into Eq. 2.17, we can plot the electric field profile at 780 nm in the r − ϕ plane with a major radius of 45 um and a minor radius of 1 um (see Fig 2.2).

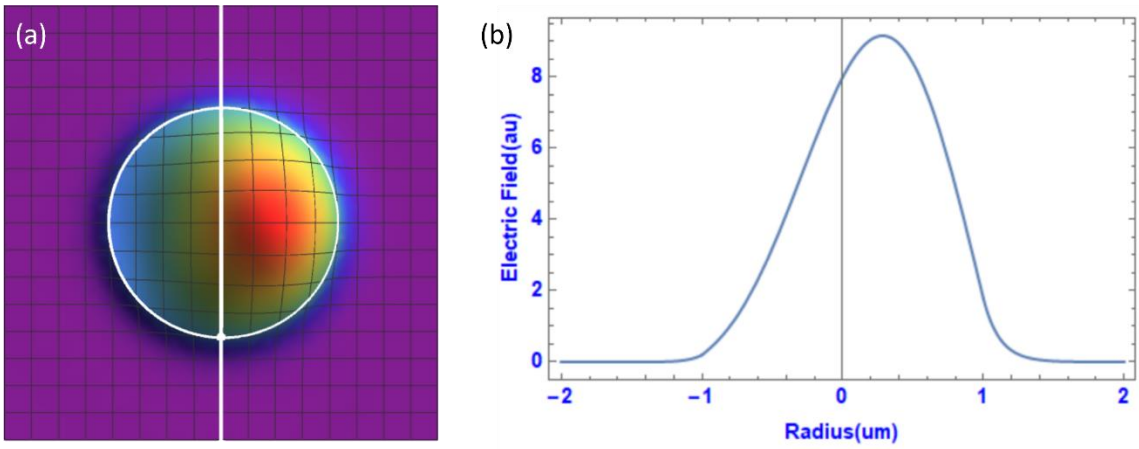

Figure 2.2. (a) Electric field distribution of fundamental TE mode in the cross section of toroidal coordinate system. The white circle stands for the boundary of the toroid. There is only one hotspot close to the boundary of the toroid. (b) E-field distribution along the r-axis.

The results for a minor radius of 2um are shown in Figure 2.3.

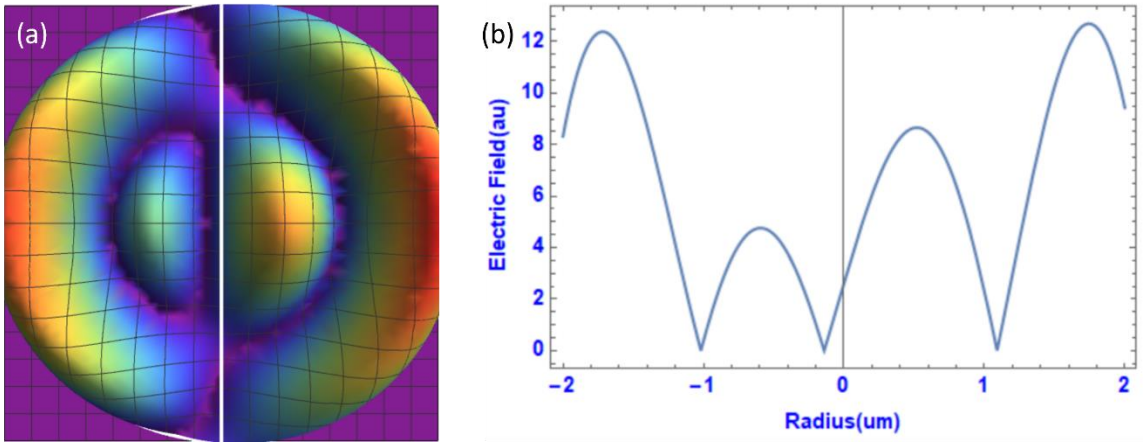

Figure 2.3. (a) Electric field distribution in the cross section of toroidal coordinate system. (b) E-field distribution along the r-axis.

Obviously, when the geometry changes, the corresponding electric field distribution is no longer a fundamental TE mode pattern, which may be caused by inaccurate estimation of some

parameters in Eq. 2.10. such as β, and n_{eff}, or by not introducing higher-order wave equations. To obtain more accurate results, we will use the COMSOL software based on the finite element method (FEM) for solving.

2.3 Mode analysis using finite element method (FEM) in COMSOL

2.3.1 Mode analysis of straight waveguide

As discussed in the last section, the mode analysis of the toroid cross section is the derivation of the propagation constant and the effective mode index. In this section, a detailed description of how to use COMSOL for model construction and analysis will be provided. It is worth mentioning that COMSOL Multiphysics used in this dissertation is version 5.3. In the FEM method, the entire system is decomposed into a number of subdomains, in each of which the partial differential equations (PDE) are solved by applying specific boundary conditions and finally recombined to complete the final calculation. One of the advantages of the FEM method is the ability to mesh and solve for curved structures.

Beginning with the mode distribution in the straight waveguide, in the electric field described in Eq. 2.6, it is well known that a confined mode of a straight waveguide needs to satisfy the condition:

$$n_{cladding} < n_{eff} < n_{core} \tag{2.18}$$

which means that the effective refractive index is in the range between the material refractive index of the core and the cladding. Furthermore, as n_{eff} approaches the upper limit of this interval, the wave is more confined.

In the Modal Wizard window in COMSOL, the spatial dimension and physics are selected for 2D (two-dimensional) and electromagnetic waves, frequency domain (ewfd), respectively. That is, the electric field component is composed of E_x, E_y, E_z.

Parameters are created in the Global Definitions as the following table:

Name	Expression	Value	Description
wl	780 [nm]	780 nm	Wavelength
f0	c_const/wl	384349305128205 1/s	Frequency
a	2 [um]	2 um	Minor radius
n_core	1.45	1.45	Refractive index of the core
n_clad	1	1	Refractive index of the cladding

Table 2.1. Parameters for a designed straight waveguide

Next, in the geometry, a circle with a 2 um radius is created for the core. And another circle with a 10um radius is built for the cladding as shown in Figure (2.4).

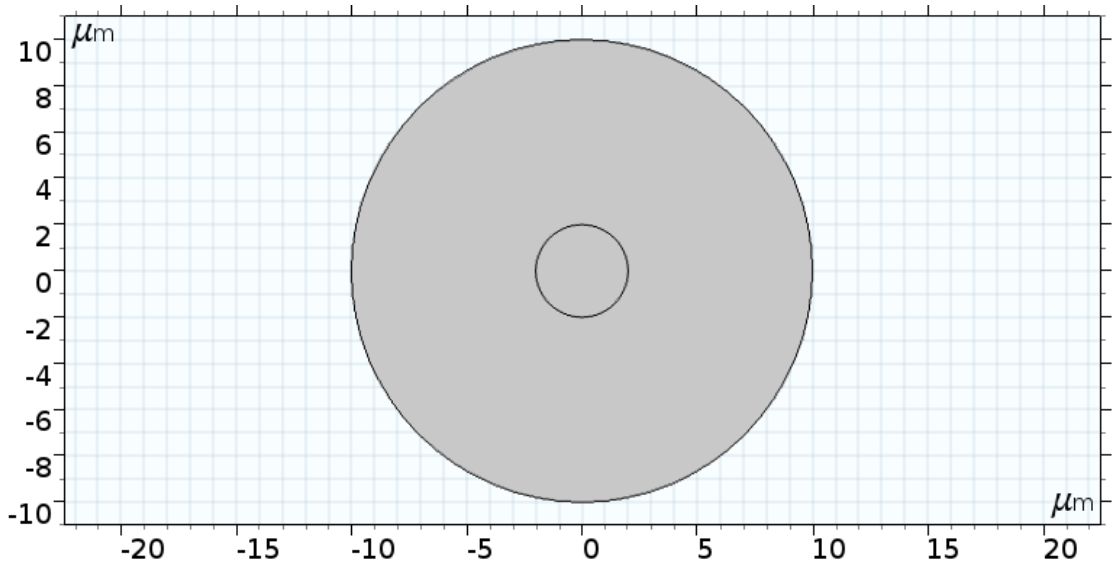

Figure 2.4. The geometry of straight waveguide (fiber) cross section in COMSOL

As discussed, since the wave mainly propagates along the z-direction, the mode evanescence rapidly from the core boundary in $x - y$ plane. As long as the cladding is large enough, the intensity of the mode radiation to the edge can be attenuated to almost zero, independent of the shape of the cladding. Fig. 2.5 shows a square cladding with 20 um side length.

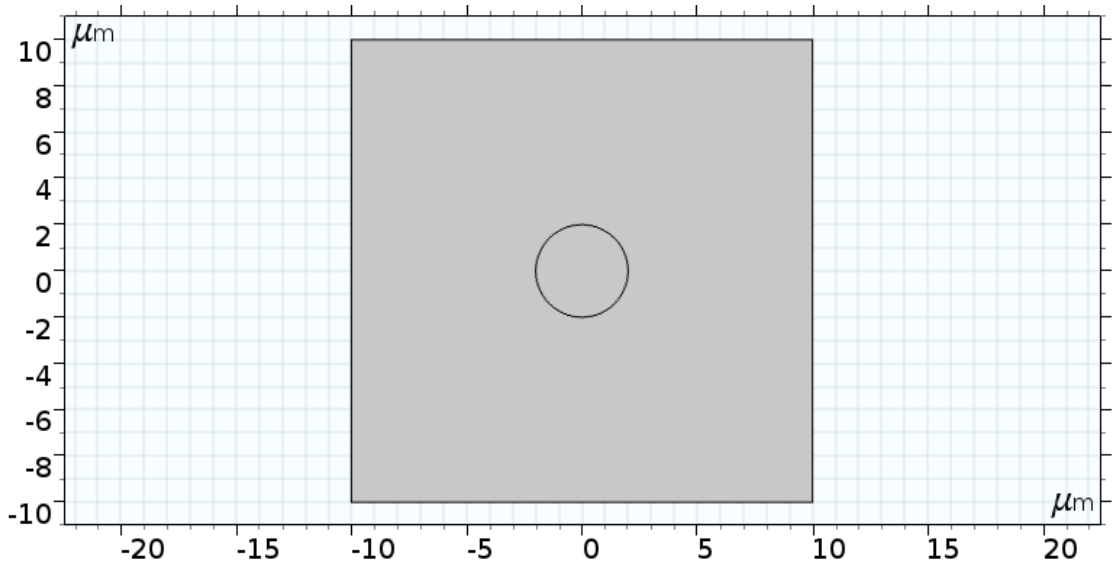

Figure 2.5. The geometry of straight waveguide (fiber) cross section with rectangular boundaries in COMSOL

For better comparison with the subsequent microtoroid mode for gas sensing, we set the core to silica with a refractive index of 1.45 and the cladding to air with a refractive index of 1 in the material parameters. The boundary condition of the outer edge of the cladding is set to the perfect electric conductor (PEC), which sets the tangential component of the electric field to zero in the following form:

$$\boldsymbol{n} \times \boldsymbol{E} = 0 \tag{2.19}$$

It leads to a perfect reflection of the wave propagating from the interior domain boundary, which is not desirable in most cases. Later the two non-reflective boundary conditions of scattering boundary condition (SBC) and perfectly matched layer (PML) will be introduced. The radiation of mode in the cross section of the straight waveguide is very weak, so the PEC can be used as a boundary condition for approximation.

In the mesh setting, free triangular is built for all domains and the mesh size of the core is predefined as "Extra fine" with a maximum element size of 0.4um which is similar to half wavelength in this case. The mesh size of the surrounding area is predefined as “Fine”. The constructed mesh is shown in Fig. 2.6.

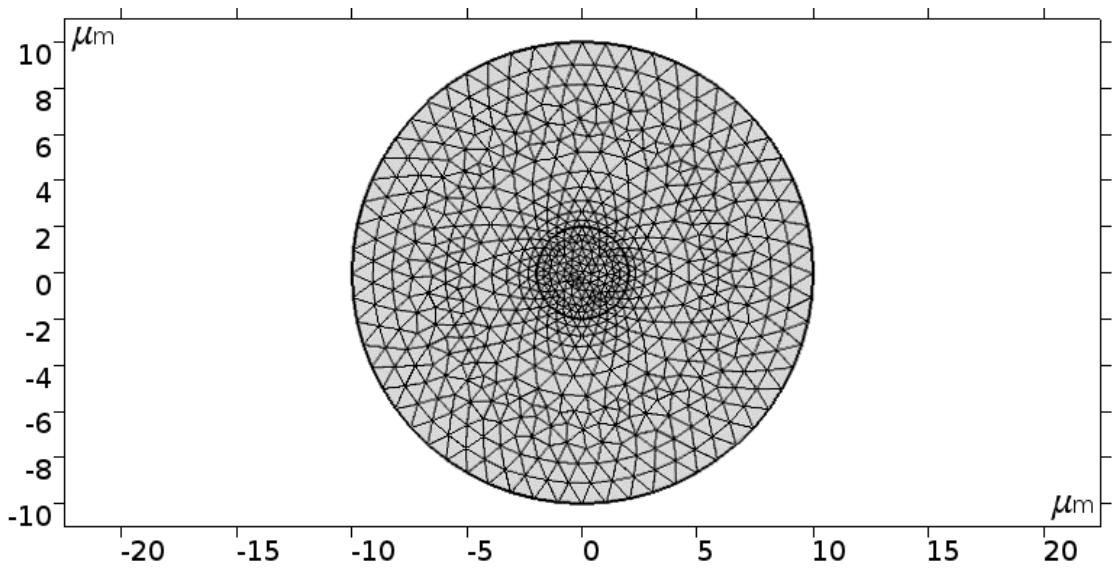

Figure 2.6. Mesh of straight waveguide (fiber) cross section in COMSOL

The 2D simulation in this case is not very demanding in terms of performance and does not require too much consideration of mesh optimization, even an extremely fine mesh can be computed without taking much time. In the subsequent 3D simulation, the mesh optimization for the confined mode will be discussed.

Mode analysis is then built in the COMSOL physics study session. Mode analysis frequency is set to f0 as defined in the global definition. The eigenvalue of the Helmholtz equation in Eq. 2.7 is solved to find the effective propagation constant β_{eff}, which is finally transformed into the effective mode index n_{eff}. Search for modes around the refractive index of n_{core}. The E-field distribution of fundamental mode corresponding to the highest n_{core} is shown below. Since the structure of the fiber core is symmetrical, the polarization direction of the mode is arbitrary.

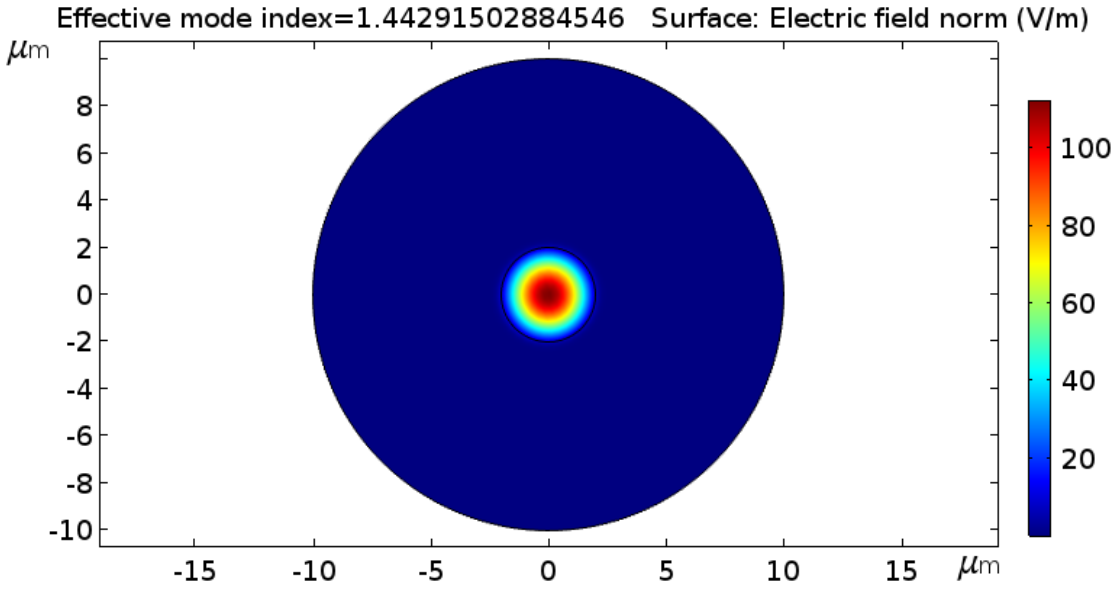

Figure 2.7. Normalized E-field distribution of fundamental mode with arbitrary polarization direction in straight fiber.

Then the case of the cladding with a square shape is resolved to obtain Fig. 2.8, it is clear that there is no difference in the electric field pattern, and the effective mode index obtained is exactly the same as the previous result in five decimal places, which is mainly related to the fine degree of the mesh.

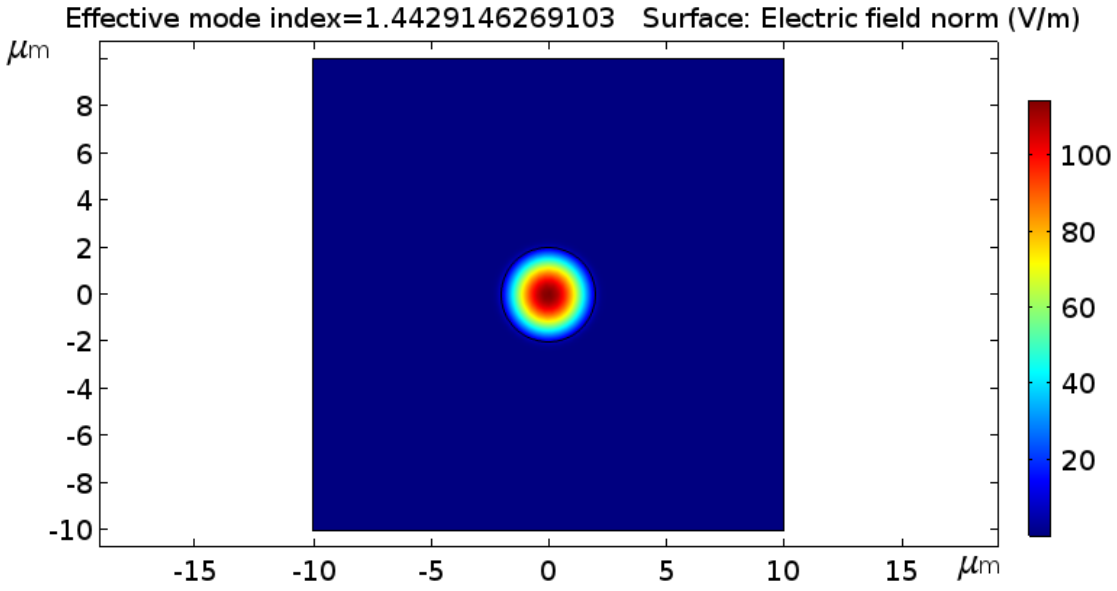

Figure 2.8. Normalized E-field distribution of fundamental mode with rectangular boundaries.

2.3.2 Mode analysis of WGM

Solving the WGM (bent fiber mode) in COMSOL is finding the solution of the Helmholtz equation (Eq. 2.8) in the cylindrical coordinate system. A two-dimensional (2D) axisymmetric mode analysis is performed here. The difference with the straight waveguide is that the eigenvalues $\lambda = -j\beta r_{eff}$ in this case, need to have the scale factor r_{eff}.

In the geometry, the cross-section of a microtoroid with a major radius of 45 um and a minor radius of 2 um is created. A square with a side length of 20 um and a 2 um layer is built for the background. The layer with 2 um thickness is used as PML for wave absorption. The

whole section is rotationally symmetric with $r = 0$ as the axis (Fig. 2.9). The material is still a core with a refractive index of 1.45 and an air background of 1.

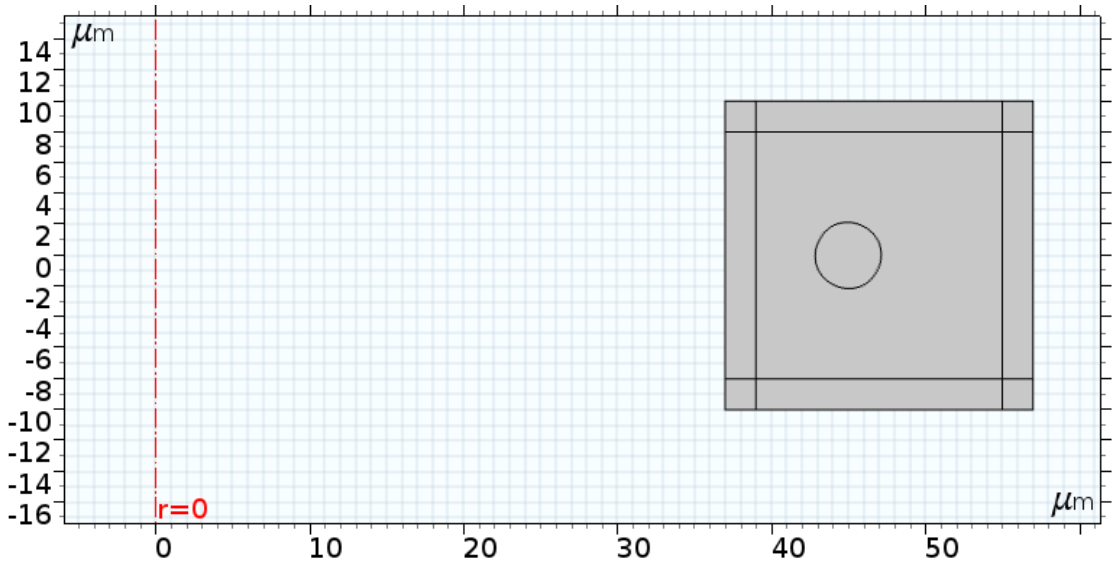

Figure 2.9. The geometry of WGM cross section with rectangular boundaries in COMSOL

As discussed in section 2.2, in the cross-section of a WGM (bend fiber mode), the wave is radiating in the radial direction. Due to the limited size of the model, it is very important to create a no reflection boundary condition to avoid the influence of radial wave reflection on the confined mode. The perfectly matched layer (PML) and the scattering boundary condition (SBC) are two common boundary conditions that are transparent to radiation.

Unlike common boundary conditions, PML is not applicable directly to a line boundary but a domain. The material of PML is the same as the surrounding area with a refractive index of 1. PML with cylindrical coordinates can be found in Definitions under Component Section, whose settings and selection domains are illustrated in the following figure.

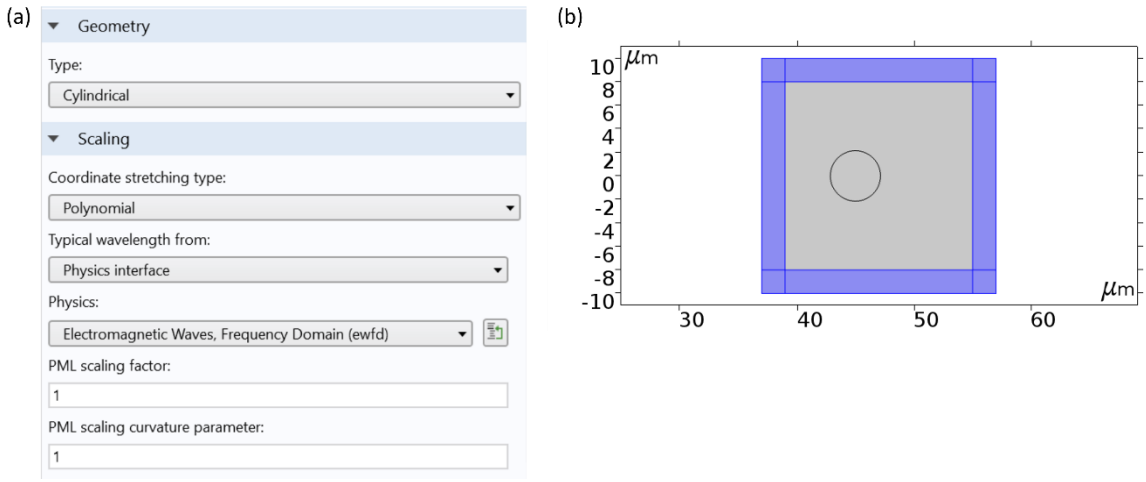

Figure 2.10. (a) The setting of PML. (b) The selected domain of PML

The SBC boundary condition is an approximation of the Sommerfeld radiation condition, whose second-order form can be expressed as:

$$\mathbf{n} \times (\nabla \times \mathbf{E}) - (jk + 1/(2r))\mathbf{n} \times (\mathbf{E} \times \mathbf{n}) - \frac{1}{2jk_0 + 1/r} \nabla \times [\mathbf{nn} \cdot (\nabla \times \mathbf{E})] = 0 \qquad (2.20)$$

The reflection of plane waves at first-order, second-order SBC, and PML with respect to the angle of incidence is shown in Fig. 2.11. It can be seen that in some models with small incidence angles, the performance of SBC and PML are almost the same. PML is more applicable to a wider range of angles and is more effective in weakening the reflection but has higher requirements for computational performance.

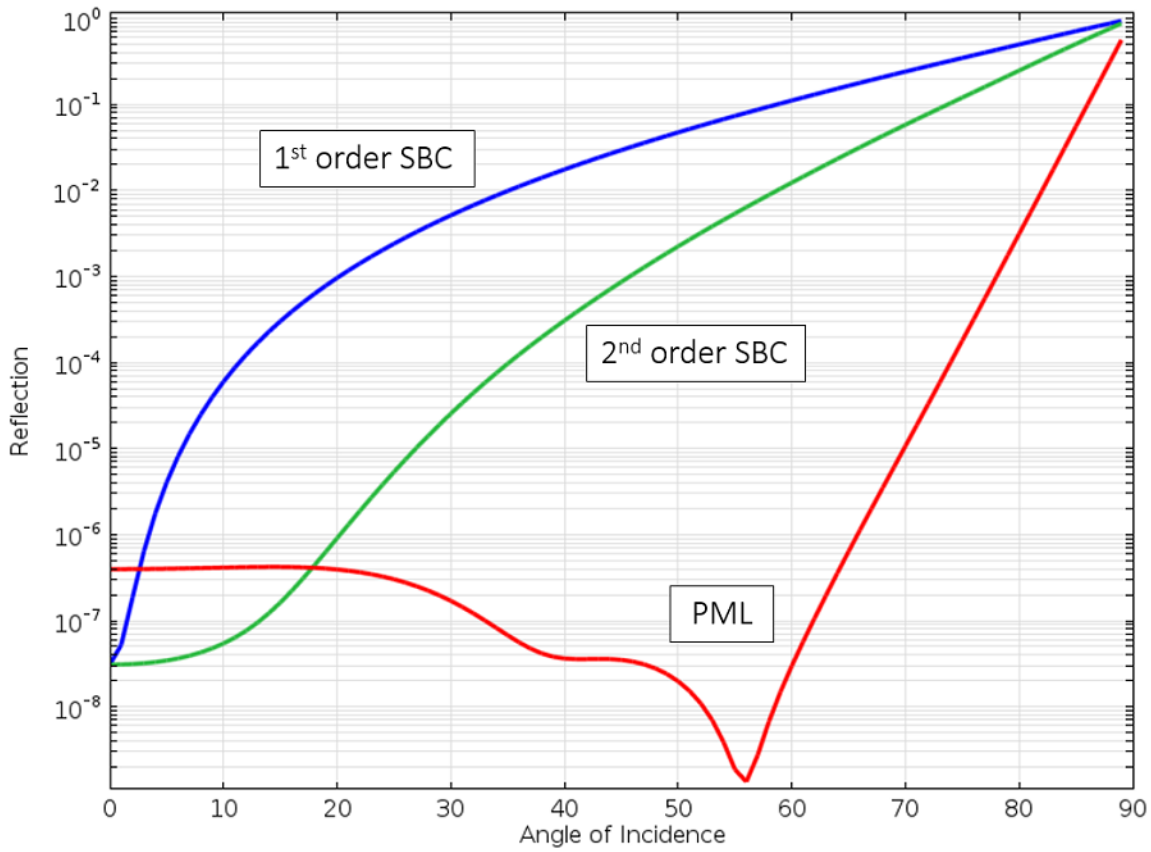

Figure 2.11. Reflection of a plane wave at the first- and second-order SBC and the PML with respect to the angle of incidence.[35]

The mesh is consistent with the setting of the straight waveguide, i.e., the core is predefined as “Extra fine” and the cladding is “Fine”. PML uses a mapping method to create the mesh with 5 distribution layers, as shown in Fig. 2.12.

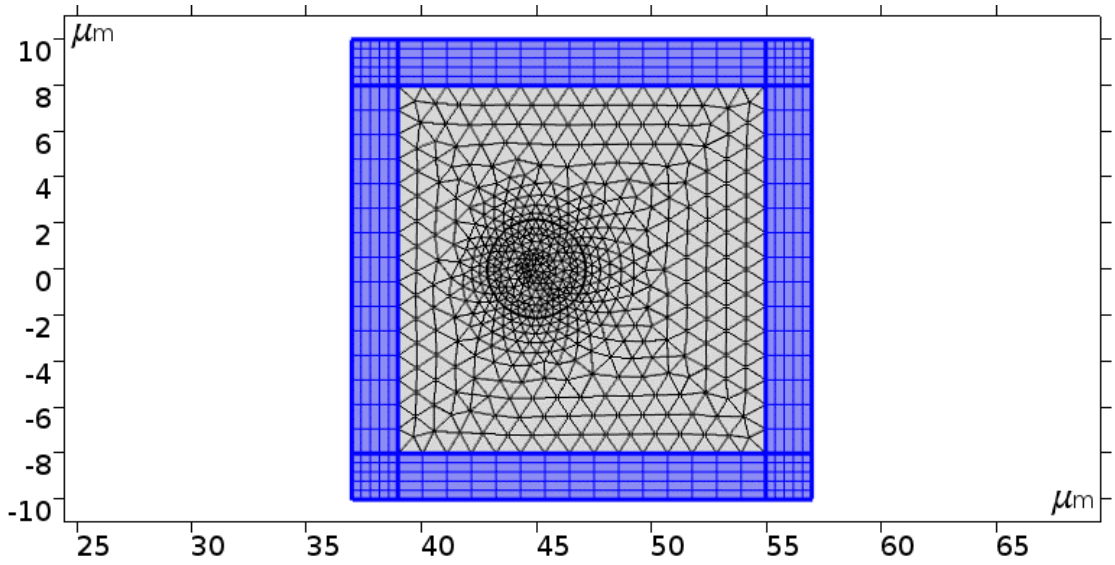

Figure 2.12. Mesh of WGM cross section in COMSOL

In the settings of mode analysis, because the mode is more confined around the equator of the toroid, the eigenvalues search for is approximately $n_{core} \times 47um$ which is scaled by the principal radius ($45\ um\ +\ 2\ um$). The fundamental TE mode profile and the normalized electric field amplitude along the radial direction are present in Fig. 2.13. The n_{eff} from this eigenvalue 6.6287×10^{-5} is 1.4255, which still satisfies the mode confinement condition in the waveguide.

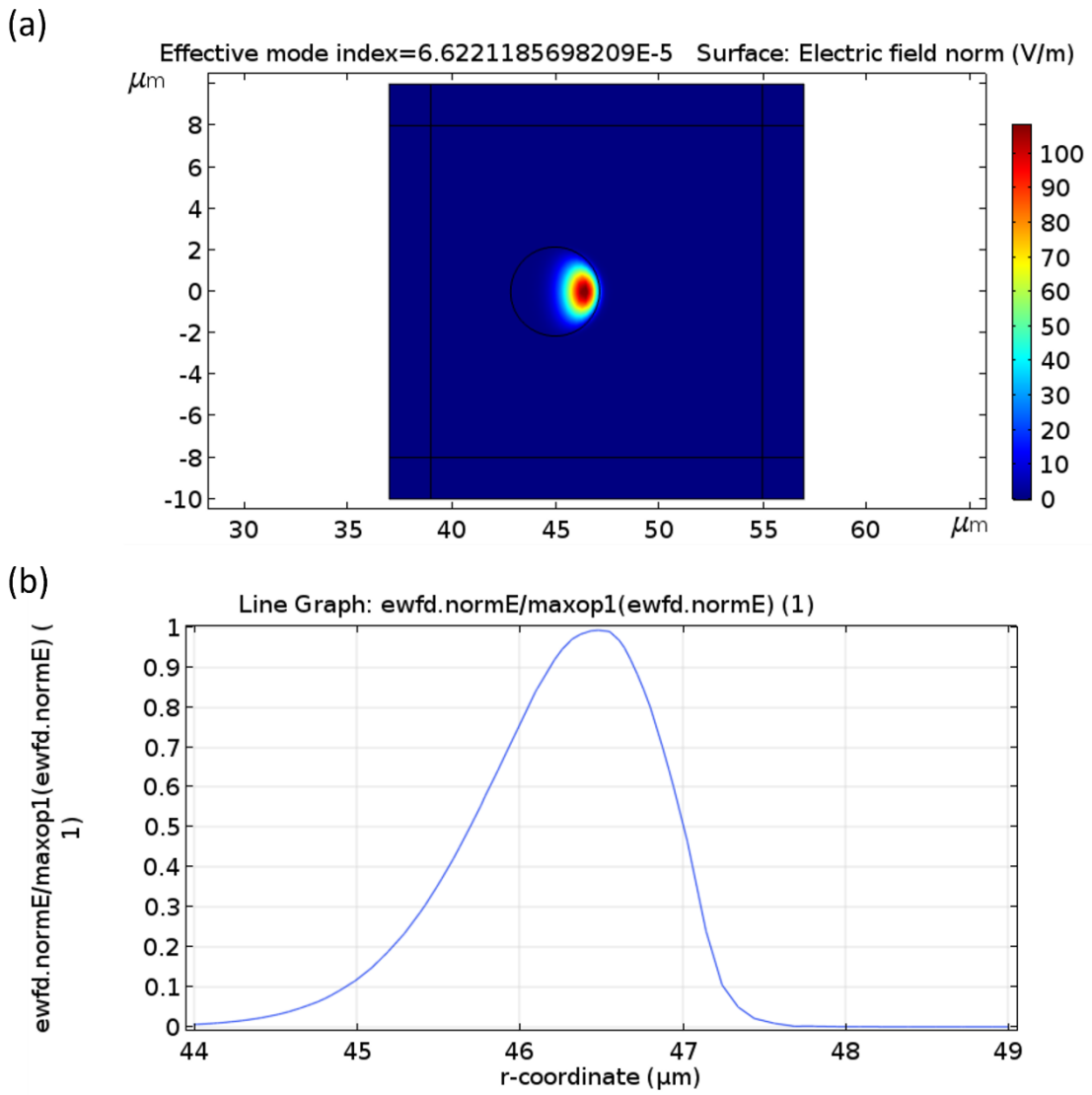

Figure 2.13. (a) Fundamental TE mode profile. (b) Normalized E-field amplitude along the radial axis.

This result has only one hotspot which is significantly more accurate than the mode pattern of the WGM with a minor radius of 2um in section 2.2. Further, the mode analysis was performed on the WGM with a minor radius of 1um, and the results are shown in Fig. 2.14. Its

evanescent tail can reach a few hundred nanometers outside the boundary $r = 46um$. This small minor radius can still trap almost all the energy in the cavity.

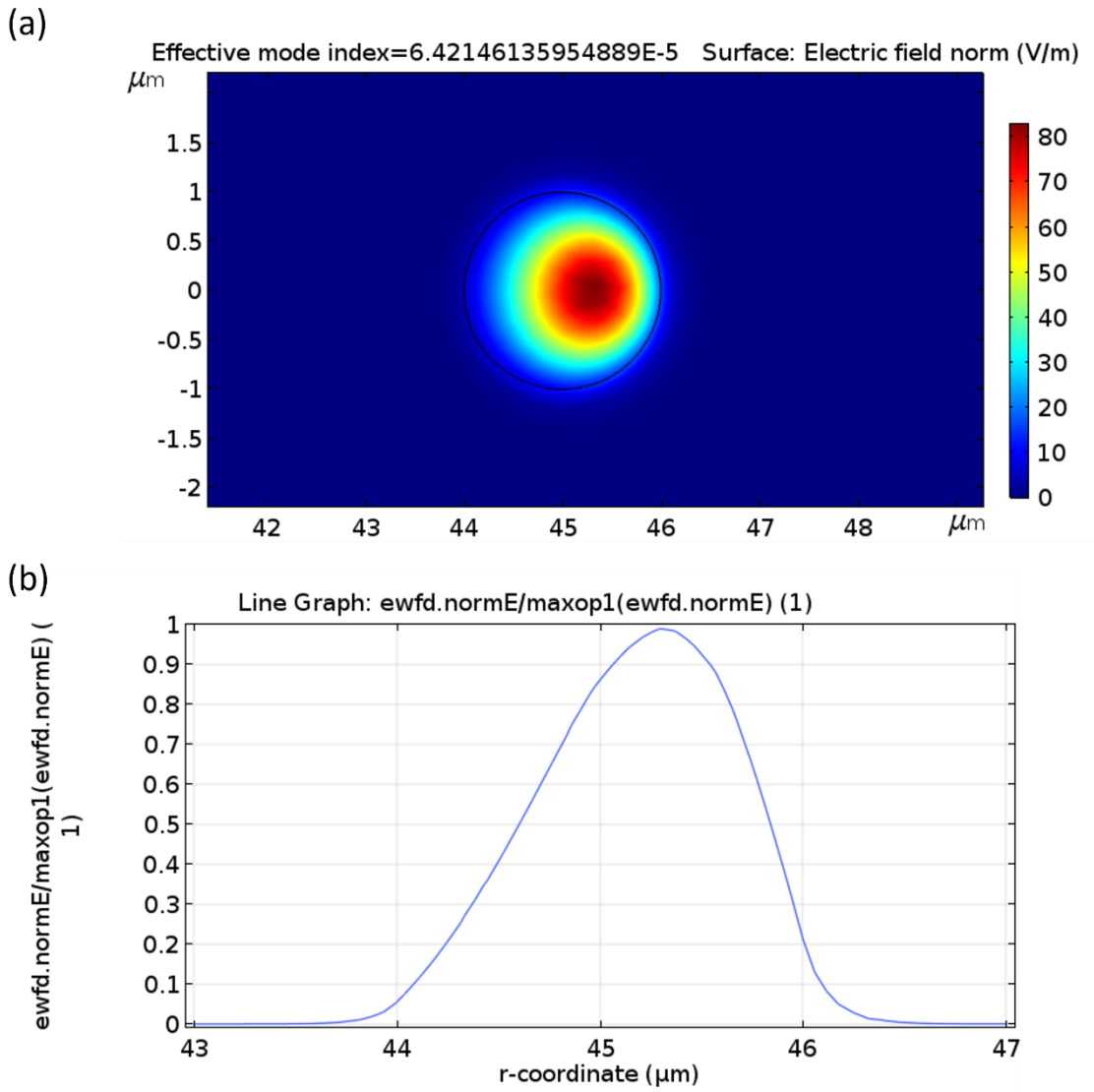

Figure 2.14. (a) Fundamental TE mode profile of WGM microtoroid with a minor radius of 1 um. (b) Normalized E-field amplitude along the radial axis.

Furthermore, in Fig. 2.15, the effective refractive index is found as a function of minor radius, and when the minor radius is less than 0.5 um, the fundamental mode of 780 nm can no longer be confined.

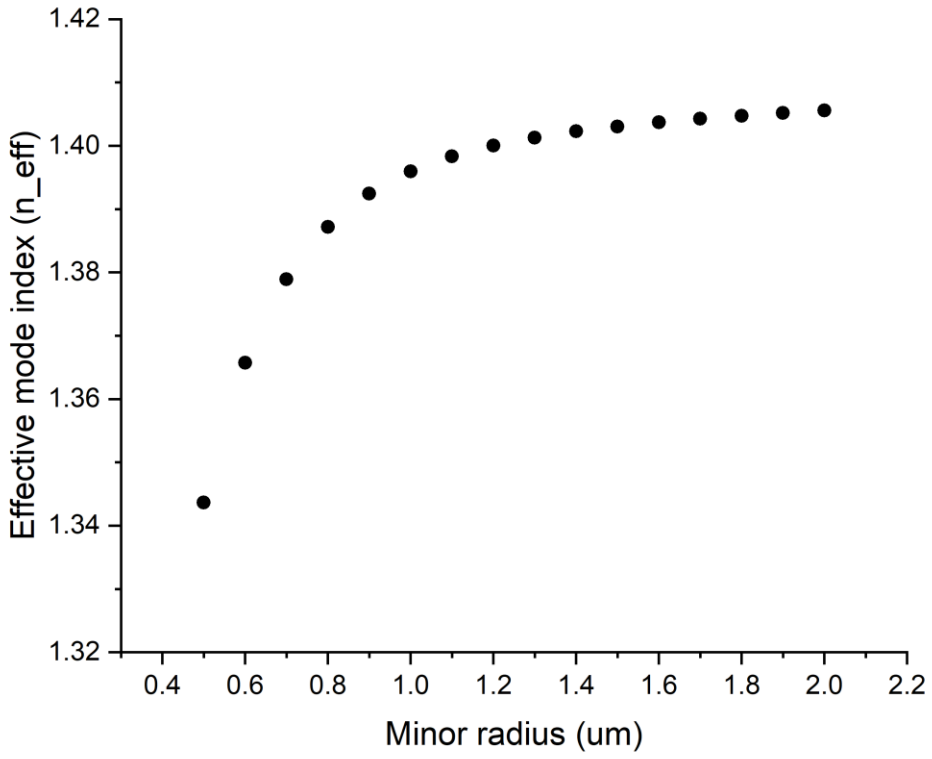

Figure 2.15. Relationship of the effective refractive index of the fundamental TE mode and the minor radius of the toroid cavity.

2.3.3 Eigenfrequency solver for WGM

Another technique to simulate WGM is to use eigenfrequency analysis, which solves for the entire model's eigenfrequency and eigenmode. Similarly, the Helmholtz equation is solved,

but with an unknown propagation in the out-of-plane dimension and a more general time-harmonic description of the field that includes the phase's complex characteristics.

$$\boldsymbol{E}(\boldsymbol{r},t) = Re\left(\widetilde{\boldsymbol{E}}(\boldsymbol{r})e^{-\lambda t}\right) \tag{2.21}$$

where the eigenvalue $\lambda = -j\omega + \delta$ has an imaginary component that represents the eigenfrequency and a real component that represents the damping. This approach can also be used to determine the Q as mentioned in section 2.1.2.

At this stage, the azimuth mode number needs to be estimated, i.e., variable m in Eq. 2.1 must be approximated as:

$$m = \frac{2\pi \mathrm{R}_p n_{eff}}{\lambda} \approx \frac{2\pi \mathrm{R}_p n_{\mathrm{core}}}{\lambda} \tag{2.22}$$

With a core refractive index of $1.45 + 10^{-8}i$ [27] and a principal radius of 47 um, the m at 780 nm can be obtained as about 549. This setting can be found at Out-of-Plane Wave Number under Electromagnetic Waves, Frequency Domain in COMSOL. The mode analysis will be replaced by the eigenfrequency solver in the study configuration. Fig. 2.16 depicts the fundamental TE mode of WGM that's been discovered. The corresponding Q of 7.27×10^6 is quite close to the experimental data, demonstrating that the imaginary part ($10^{-8}i$) of the refractive index representing the loss is valid.

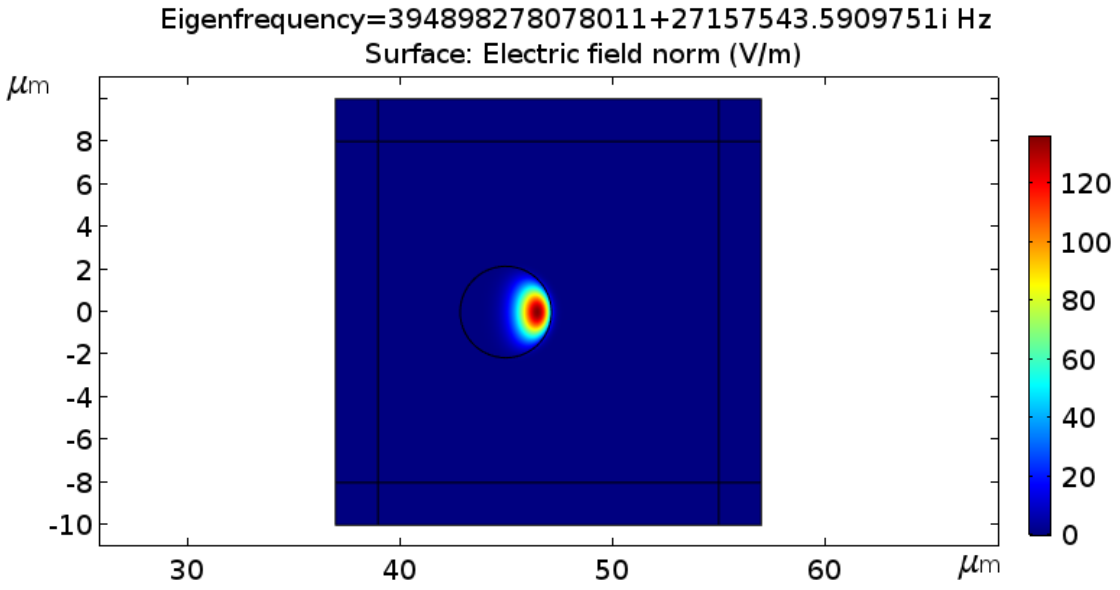

Figure 2.16. Fundamental TE mode pattern in WGM using eigenfrequency solver.

Since the subsequent biochemical applications, we mainly explore the mode shift mechanism of WGM, focusing on extremely small wavelength shifts $\Delta\lambda$ caused by tiny particles, the eigenfrequency is more applicable. This two-dimensional axisymmetric model using an eigenfrequency solver will also serve as an important reference for the three-dimensional model of WGM microtoroid.

2.4 Coupled mode theory (CMT)

In the research of whispering gallery mode cavities, many various coupling methods are now available, such as optical fiber (waveguide) coupling, free-space prism coupling, grating coupling, and so on. The confined WGM can be modulated and used in further applications. As a result, it is critical to investigate and analyze the coupling process. Coupled-mode theory (CMT)

has been commonly used as a mathematical tool for analyzing electromagnetic wave propagation and interaction with the medium. Here the two classical cases of coupled resonators and coupled waveguides will be studied, which correspond to the schemes of coupled-mode theory in time and space respectively. Finally, a waveguide-microring coupling model in COMSOL will be introduced. These discussions are further explained and applied in the following chapters.

2.4.1 Resonators coupling

Consider two lossless resonators that are weakly coupled. a_1 represents the amplitude in one resonator with the time dependence exp $(j\omega_1 t)$ and a_2 represents the amplitude in the other resonator with the time dependence exp $(j\omega_2 t)$, which stands for the positive frequency component of the electric field amplitude. They are subject to the following differential equations:

$$\frac{da_1}{dt} = j\omega_1 a_1 \tag{2.23}$$

$$\frac{da_2}{dt} = j\omega_2 a_2 \tag{2.24}$$

The time dependence of the two resonators alters when they are coupled weakly:

$$\frac{da_1}{dt} = j\omega_1 a_1 + j\kappa_{12} a_2 \tag{2.25}$$

$$\frac{da_2}{dt} = j\omega_2 a_2 + j\kappa_{21} a_1 \tag{2.26}$$

where κ_{12} and κ_{21} are the coupling coefficients. In general, we consider energy to be a positive value. To simplify the calculation, the energy of the mode is equal to the square of the normalized

electric field amplitude. The total energy of the two modes will be $W = |a_1|^2 + |a_2|^2$. Energy must be conserved in the situation of a lossless coupling:

$$\frac{\mathrm{dW}}{\mathrm{dt}} = \frac{\mathrm{d}(|a_1|^2 + |a_2|^2)}{\mathrm{dt}} = j\kappa_{12}\mathrm{a}_1^* a_2 + j\kappa_{21}a_2^* a_1 - j\kappa_{12}^* a_1 a_2^* - j\kappa_{21}^* a_2 a_1^* = 0 \qquad (2.27)$$

which is true only when $\kappa_{12} = \kappa_{21}^* = \kappa$.

With the combination of the two Eq. 2.25 and 2.26, the eigenfrequency of the coupled system can be determined as:

$$\omega = \frac{\omega_1 + \omega_2}{2} \pm \sqrt{(\frac{\omega_1 - \omega_2}{2})^2 + |\kappa|^2} \qquad (2.28)$$

It can be seen from the equation that when the two frequencies are different ($\omega_1 \neq \omega_2$), the introduction of the mode with ω_2 causes the detuning of ω_1. This frequency shift can be further explored and explained by perturbation theory, which has significant applications in the subsequent WGM biochemical sensing as well as plasmonic hybrid systems.

2.4.2 Waveguides coupling

Consider a system in which two modes propagate along the z-direction and have spatial component exp $(-j\beta_1 \mathrm{z})$ and exp $(-j\beta_2 z)$, respectively, where β_1 and β_2 are their independent propagation constants. When they propagate separately in their individual waveguides and at infinite distances, that is, with no coupling:

$$\frac{\mathrm{d}a_1}{\mathrm{dz}} = -j\beta_1 a_1 \qquad (2.29)$$

$$\frac{\mathrm{d}a_2}{\mathrm{dz}} = -j\beta_2 a_2 \tag{2.30}$$

When the two waveguides are brought close together, the two modes will couple with each other through evanescent field interactions, which can be expressed as:

$$\frac{\mathrm{d}a_1}{\mathrm{dz}} = -j\beta_1 a_1 - jK_{12}a_2 \tag{2.31}$$

$$\frac{\mathrm{d}a_2}{\mathrm{dz}} = -j\beta_2 a_2 - jK_{21}a_1 \tag{2.32}$$

where K_{12} and K_{21} are the coupling coefficients in space. For the waves to be able to interact with each other, the propagation constants β_1 and β_2 must be of the same sign and approximately equivalent. According to the law of power conservation, the total power of the two modes propagating along the z-axis spatially remains consistent:

$$\frac{\mathrm{d}\boldsymbol{P}}{\mathrm{dz}} = 0 \tag{2.33}$$

where $K_{12} = K_{21}^{*} = K$ is required. The power matrix $\boldsymbol{P} = \mathrm{diag}(1, \pm 1)$ where the symbols refer to the power flow of the two waves.

For the simplicity, it is assumed that:

$$a_1 = \mathrm{A}_1 \exp\{-j\frac{\beta_1 + \beta_2}{2}z\} \tag{2.34}$$

$$a_2 = A_2 \exp\{-j\frac{\beta_1 + \beta_2}{2}z\} \tag{2.35}$$

where A_1 and A_2 are the respective amplitudes of the two modes. Interactions of the two modes can be rewritten as:

$$\frac{\mathrm{dA}_1}{\mathrm{dz}} = -j\frac{\beta_1 - \beta_2}{2}\mathrm{A}_1 - jK_{12}\mathrm{A}_2 \tag{2.36}$$

$$\frac{\mathrm{d}A_2}{\mathrm{dz}} = -j\frac{\beta_2 - \beta_1}{2}A_2 - jK_{21}A_1 \tag{2.37}$$

The coupling matrix can evidently be given as:

$$\boldsymbol{M} = -\begin{bmatrix} \dfrac{\beta_1 - \beta_2}{2} & K_{12} \\ K_{21} & \dfrac{\beta_2 - \beta_1}{2} \end{bmatrix} \tag{2.38}$$

which needs to meet the law of power conservation: $\boldsymbol{PM} = \boldsymbol{M}^{\dagger}\mathbf{P}$.

When $\beta_1 = \beta_2$, namely, phase-matching:

$$\frac{\mathrm{d}A_1}{\mathrm{dz}} = -jK_{12}A_2 = -jKA_2 \tag{2.39}$$

$$\frac{\mathrm{d}A_2}{\mathrm{dz}} = \mp jK^*A_1 \tag{2.40}$$

The corresponding solutions are:

$$A_1 = A_+\exp(-j|K|\mathrm{z}) + A_-\exp\left(j|K|z\right) \tag{2.41}$$

$$A_2 = \frac{|K|}{\mathrm{K}}\{A_+\exp(-j|K|z) - A_-\exp(j|K|z)\} \tag{2.42}$$

for definite $\boldsymbol{P}$. The signs still represent the power flow directions. Obviously, compared with the mode coupling in time, the mode coupling in space is more complicated, and it needs to take into account both the direction of the group velocity and the positive and negative energy.

Take the simplest straight waveguide coupler as an example, the total energy of the system is positive, at the initial position $z = 0$, only mode 1 is being excited, then after propagating $z =$

$\frac{\pi}{2K}$ distance, all the power is transferred to mode 2, and it is transferred back and forth in the later spatial propagation with a period of $\frac{\pi}{2K}$.

2.4.3 Waveguide-microring coupling

Combining the two CMT examples in time and space discussed above, here a waveguide and a resonator are placed close enough to couple each other. In the small coupling area, the ring resonator (waveguide) portion can be approximately treated as a short straight waveguide (Fig. 2.17), which can be solved from the equations of CMT in space. [36]The relationship between the transmitted light and the incident light can be written as:

$$\begin{bmatrix} E_{t1} \\ E_{t2} \end{bmatrix} = \begin{bmatrix} t & \kappa \\ -\kappa^* & t^* \end{bmatrix} \begin{bmatrix} E_{i1} \\ E_{i2} \end{bmatrix} \tag{2.43}$$

where t and κ indicate the transmission and coupling coefficients. One thing to point out is that E_{i2} is the result of phase delay $e^{-j\phi}$ and loss L after E_{t2} travels almost one round in the ring resonator:

$$E_{i2} = E_{t2} e^{-j\phi} \cdot L \tag{2.44}$$

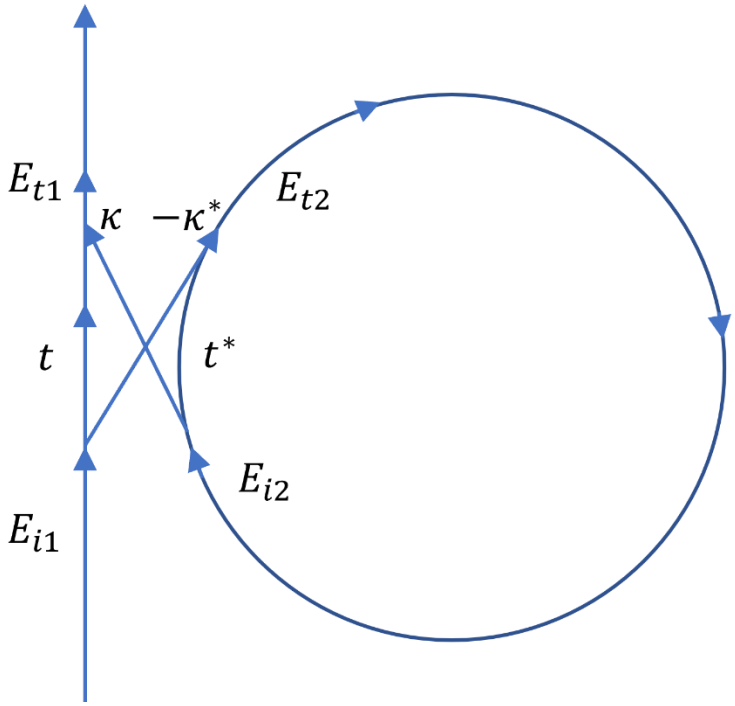

Figure 2.17. Schematic of waveguide-resonator coupling

Assume the coupling system is lossless, the power conservation law requires:

$$|E_{i1}|^2 + |E_{i2}|^2 = |E_{t1}|^2 + |E_{t2}|^2 \tag{2.45}$$

where $|t|^2 + |\kappa|^2 = 1$ needs to be satisfied.

Thus, the relationship between the transmitted light and the incident light of the straight waveguide can be written as:

$$E_{t1} = \frac{t - L\exp(-j\phi)}{1 - tL\exp(-j\phi)} E_{i1} \tag{2.46}$$

when $t = L\exp(-j\phi) = \sqrt{1-\kappa^2}$, the transmitted field $E_{t1} = 0$, which means that all the power is transferred to the ring resonator. This condition is called critical coupling. In the next WGM

sensing application, the energy needs to be coupled into the toroid cavity as much as possible to get a better signal-to-noise ratio in the output spectrum.

A 2D model of the waveguide and ring coupling process is built from the top view in COMSOL and the effect of the spacing of the two structures on the coupling results will be investigated. Since the model size is much larger than the wavelength, the Electromagnetic Waves, Beam Envelopes (ewbe) physical model will be used for the study.

As shown in Fig. 2.18, a waveguide with a width of 0.2 um and a refractive index of 1.45 is built, which is coupled to a ring resonator of the same width and material. The spacing between the two structures is initially set to 20 nm. The system operates around 780 nm, and the radius of the ring is set to 11 integer times 780 nm for satisfying the resonance conditions. The cladding is set to air with a refractive index of 1. And its width is 10 times wider than the core. The size and dimensions of the model are different from those in the actual experiment, mainly to explore a simple case about the coupling of waveguide and resonator, setting the fiber core too small also to avoid the coupling between different modes.

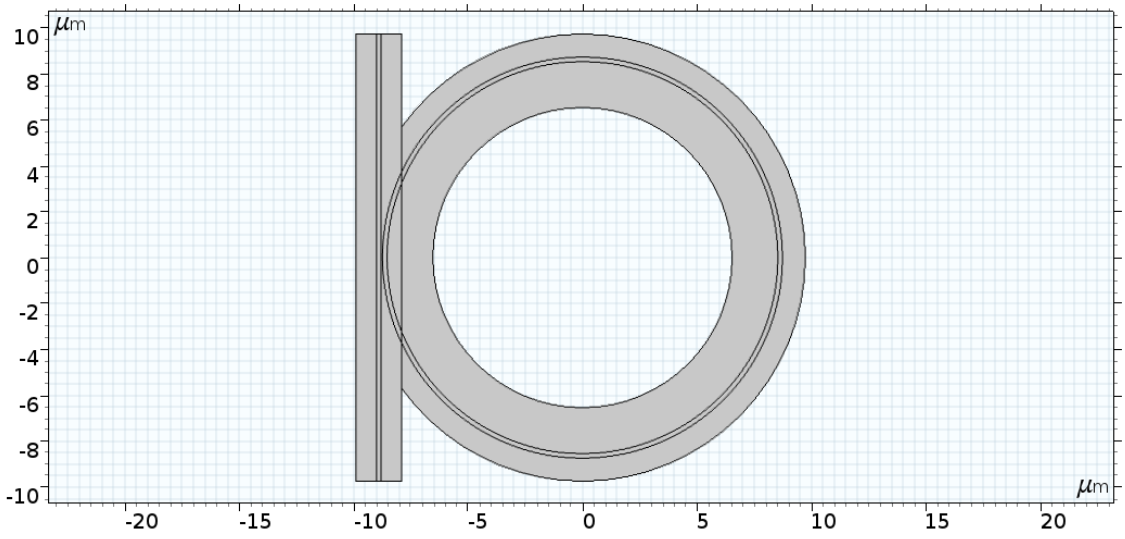

Figure 2.18. The geometry of the waveguide-resonator coupling model

The boundary marked by the blue line in Fig. 2.19 is given as field continuity to ensure that the tangential component of the electromagnetic field remains continuous even under phase jump. The lower and upper ports of the straight waveguide are set as port 1 with incident light and port 2 with transmitted light, respectively. The external boundary conditions are set to SBC to absorb the radiated electric field.

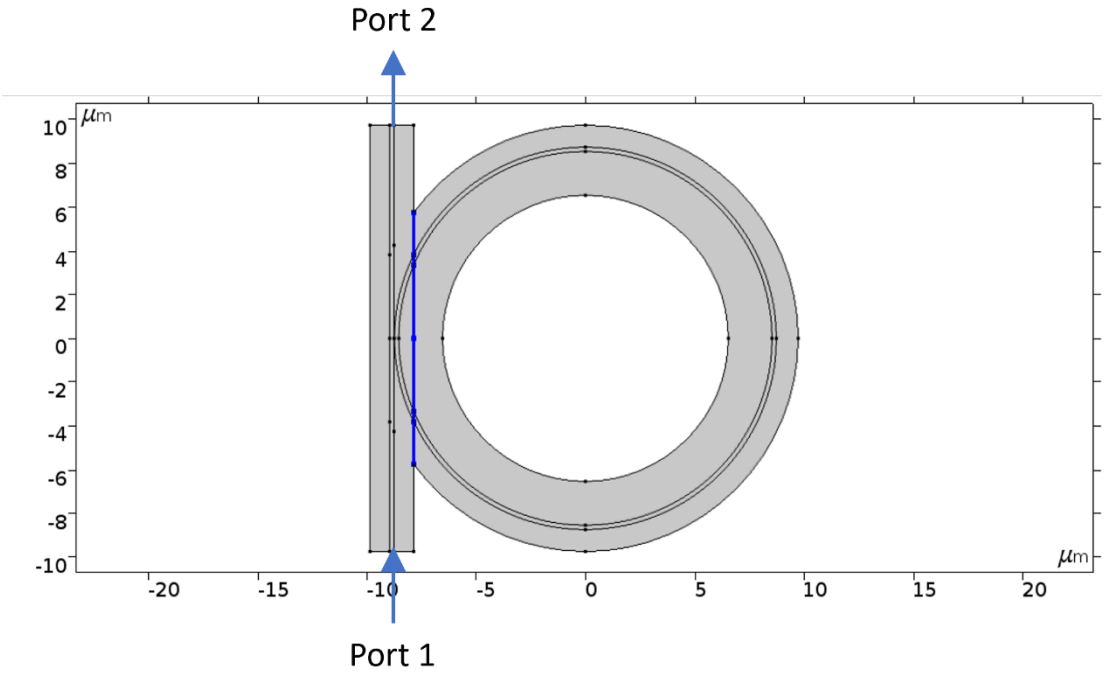

Figure 2.19. Boundary conditions of waveguide-resonator coupling model

Boundary mode analysis is performed initially for ports 1 and 2, respectively, in the study. After that, the frequency domain solver is utilized to investigate how the field propagates from port 1 to port 2. Fig. 2.20 depicts the normalized electric field of port 1. After that, as illustrated in Fig. 2.21, the transmission spectrum vs wavelength can be generated by parametric scanning of

the wavelength. The S-parameter S_{21}, which indicates the voltage transmission coefficient from port 1 to port 2, is being used to determine the transmittance coefficient $|S_{21}|^2$.

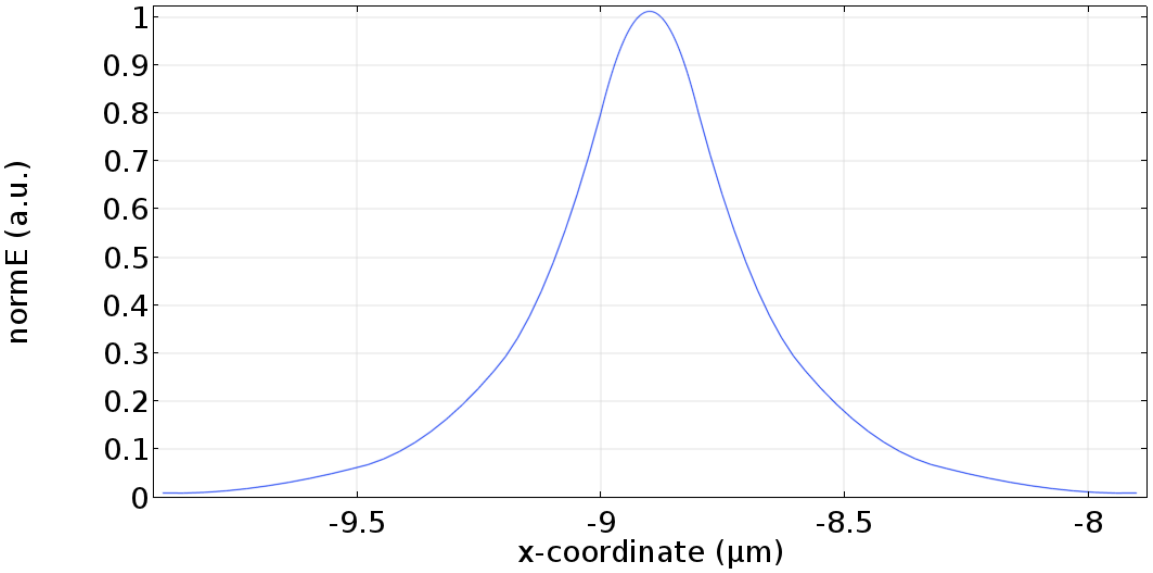

Figure 2.20. Normalized E-field of port 1 using boundary mode analysis

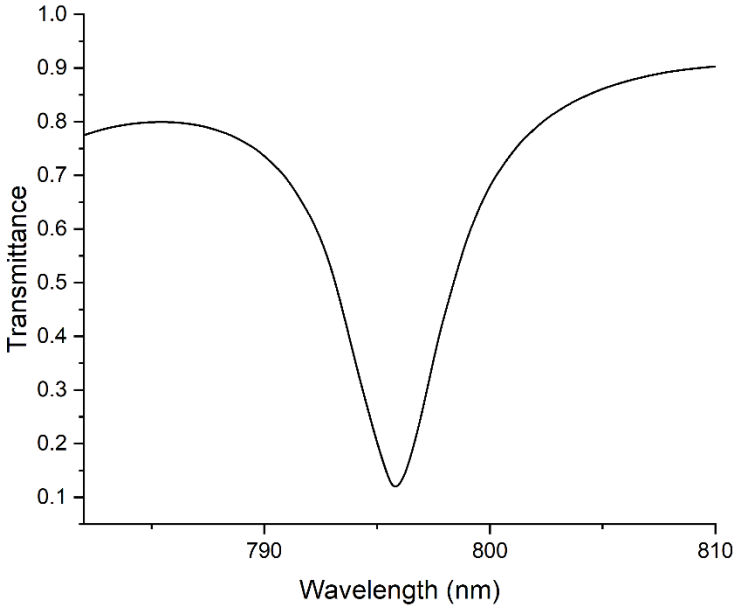

Figure 2.21. Transmittance vs. wavelength

From the figure, it can be seen that the resonant wavelength of the resonator with an integer multiple of 780 nm radius is 795.5 nm. This is because the effective mode index slightly differs from the material refractive index, and the resonant wavelength should be shifted to match the resonance condition. In addition, the minimum transmittance of the two structures with 20 nm spacing is not 0. For the critical coupling condition, a further sweep of the spacing of the structure is performed and the wavelength is set to the resonance of the ring resonator at 795.5 nm. To avoid possible problems with the mesh and boundary conditions in the simulation, the separation cannot be directly set to 0. Therefore, the minimum spacing is set to 0.2 nm, which is almost in contact with each other.

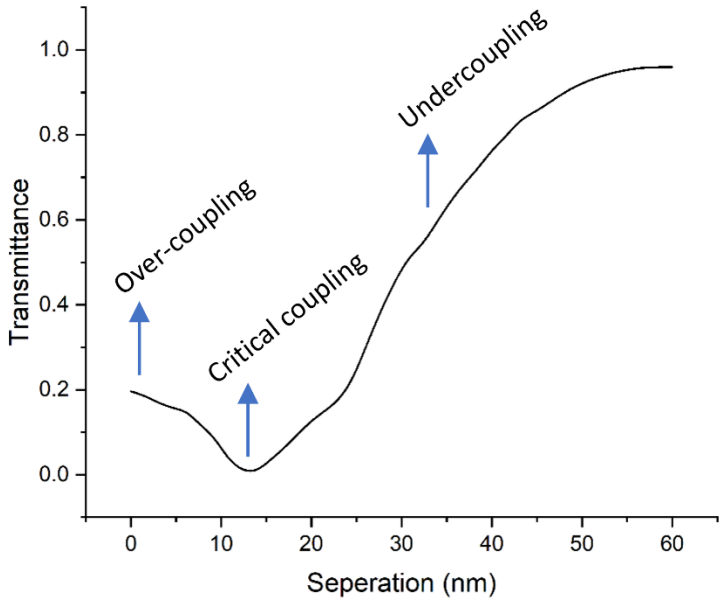

Figure 2.22. Transmittance vs. separation

As shown in Fig. 2.22, when sweeping the spacing between the two structures, it is clear that the transmittance of the straight waveguide port 2 is minimal at the 13 nm gap and is nearly 0. It can be assumed that all the power is coupled into the ring resonator corresponding to the critical coupling (Fig. 2.23(a)). While the transmittance increases at closer distances, which is characterized as over-coupling (Fig. 2.23(b)). After the critical coupling, the transmittance gradually increases with distances, which is referred to as under coupling (Fig. 2.23(c)). Also visually it can be seen that the upper part of the straight waveguide, the transmitted E-field, is varied in different coupling cases. The coupling efficiency is a function of the spacing in this 2D model, and it can be deduced that altering the distance between the taper fiber and the microtoroid is a useful technique to regulate the coupling efficiency in practical experiments.

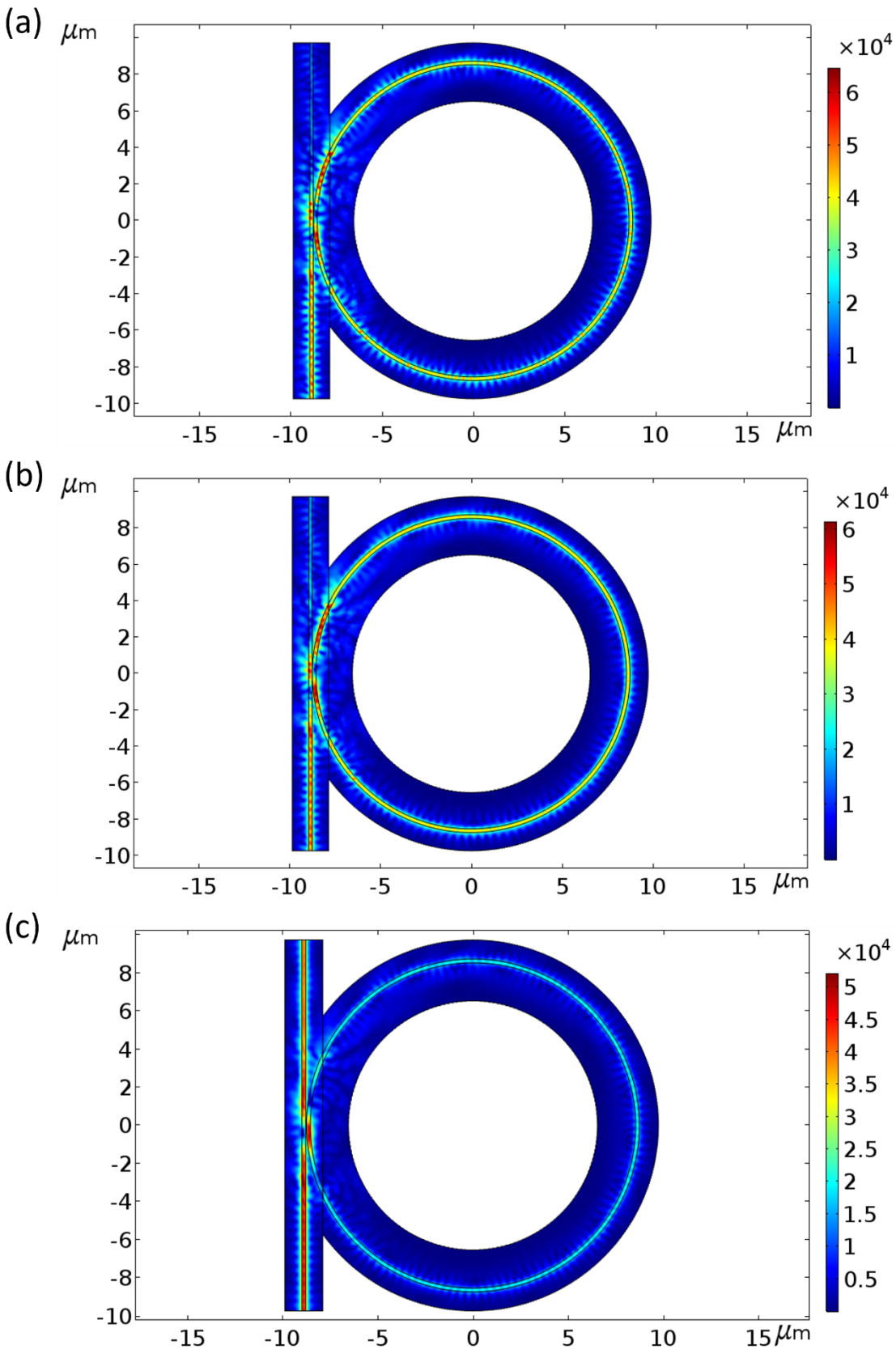
(a)
μm
×10^4
6
5
4
3
2
1
8
6
4
2
0
-2
-4
-6
-8
-10
-15
-10
-5
0
5
10
15
μm
(b)
μm
×10^4
6
5
4
3
2
1
8
6
4
2
0
-2
-4
-6
-8
-10
-15
-10
-5
0
5
10
15
μm
(c)
μm
×10^4
5
4.5
4
3.5
3
2.5
2
1.5
1
0.5
8
6
4
2
0
-2
-4
-6
-8
-10
-15
-10
-5
0
5
10
15
μm

Figure 2.23. Electric field distribution of (a) critical coupling (b) over-coupling (c) undercoupling between waveguide and ring resonator

With the help of CMT and simulation cases of waveguide-resonator coupling, the theory of resonance conditions is more easily linked with the experimental transmission spectrum, which also provides a foundation for the subsequent sensing principles and applications. Other than that, the experimental signal-to-noise ratio can be optimized to a great extent through the adjustment of the coupling conditions. Also, by combining parameters such as coupling efficiency and coupled power, the microresonator can be better designed for other applications, such as nonlinear effects, four-wave mixing, etc.

2.5 WGM fundamental sensing mechanism

In the experiment, the light from the tunable laser is continuously scanned over a range of wavelengths and it will be evanescently coupled into the WGM microcavity through the taper fiber. The light will be trapped and circulating inside the cavity. As a result, a resonance dip is formed in the transmission spectrum (Fig. 2.24). When the microcavity is perturbed in different ways, the transmission spectrum changes accordingly, which can be used for a variety of sensing applications. Three fundamental sensing mechanisms of WGM microcavities will be introduced here.

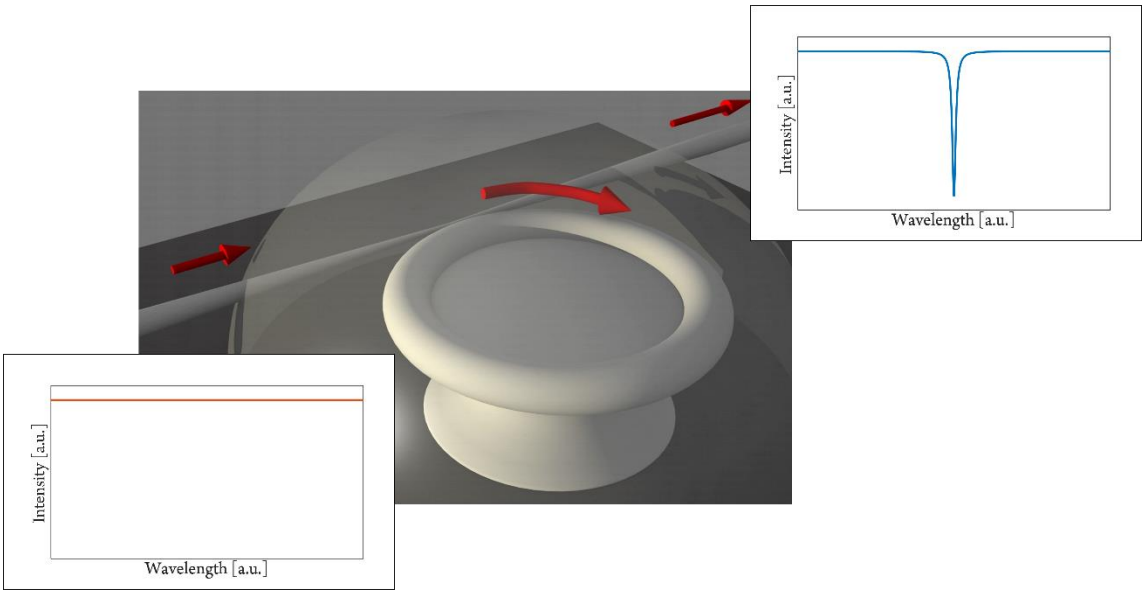

Figure 2.24. Wavelength spectrum before and after the coupling process

2.5.1 Mode shift

Mode shift is the most widespread sensing technique for WGM microresonators. Any particles binding to the surface will be interacting with the evanescent fields of the microtoroids, which acts as a change in the optical path, resulting in the frequency/wavelength shift in the output spectrum. From the point of view of resonance conditions, the adsorption/attachment of particles bring about small changes in the geometric radius of the cavity or the effective mode index, which together cause the resonance shift. This can be defined as:

$$\frac{\Delta\lambda}{\lambda} = \frac{\Delta n}{n} + \frac{\Delta R}{R} \tag{2.47}$$

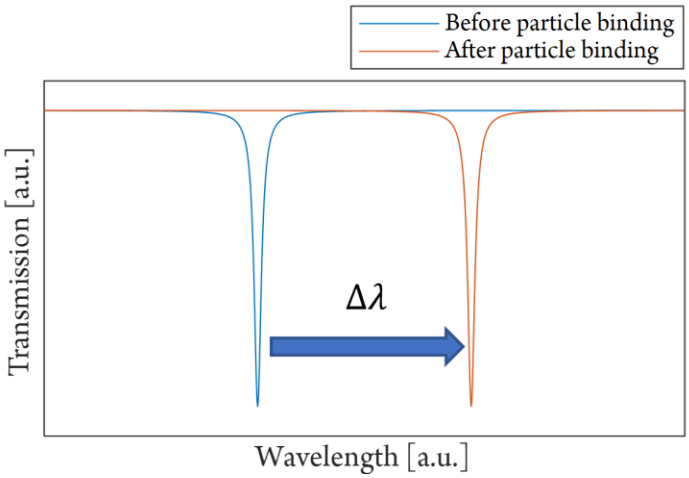

Figure 2.25. Schematic of mode shift

By tracking the resonance shift, the size and amount of detected particles can be approximately figured out from perturbation theory:

$$\frac{\Delta\lambda}{\lambda} = \frac{\alpha_{ex}|\mathbf{E}_0(\mathbf{r}_i)|^2}{2\int \varepsilon_r |\mathbf{E}_0(\mathbf{r})|^2 dV} \tag{2.48}$$

where α_{ex} is the excess polarizability of the induced dipole moment of the particle, $\mathbf{E}_0(\mathbf{r}_i)$ represents the E-field at the position of the particle, ε_r is the permittivity of the medium. This equation will be further extended to a polarizability tensor $\vec{\alpha}(\lambda)$ corresponding to the orientation of the particle and the polarization of the interacting electric field (Chapter 3).

Combined with different functionalized layers, microcavity can be a sensitive and selective biochemical sensor. Furthermore, according to Eq. 2.47, physical variables that may induce refractive index changes or dimensional changes, such as heat, thermal expansion, tension, strain, and so on, can also be measured in addition to particle binding events. Experimentally, the wavelength shift induced by circulating light and surrounding temperature changes together, also

known as the thermal effect, can also be seen as thermal noise for sensing applications. Methods of compensation and cancellation of this noise will be discussed in the subsequent sections.

2.5.2 Mode splitting

Mode-splitting is a sensing technique wherein specific targets are bound to the resonator, breaking the degeneracy between clockwise (CW) and counter-clockwise (CCW) resonant modes. For WGMs in an axisymmetric coordinate system, the CW and CCW modes feature the same resonant frequency and field distribution, but with opposite propagation directions. The scattering generated from a binding particle will induce the coupling of CW and CCW modes to form two standing wave modes (SWMs). Then the particle is able to be detected and sized through the wavelength difference between two SWMs.

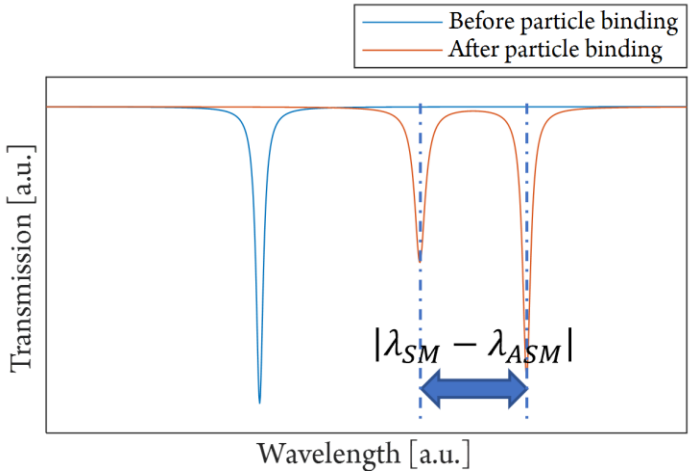

Figure 2.26. Schematic of mode splitting

Experimentally, mode-splitting in microtoroids has been demonstrated for sizing nanoparticles as small as 30 nm in radius [37]. Smaller particles with stronger polarizability material can theoretically be identified.

Mode splitting is appealing compared to other sensing approaches because the sensing signal is conceptually less sensitive to the target binding location. And it is relatively stable to changes in environmental temperature and pressure.

2.5.3 Mode broadening

Mode broadening refers to the change of the mode linewidth in the reflection and transmission spectrum, which probes the particles from the perspective of their loss. Similar to mode splitting, mode broadening is also a detection method that is not responsive to environmental conditions and does not require high Q. In experiments, mode shift and mode broadening can also be employed simultaneously to detect WGM-particles interactions.

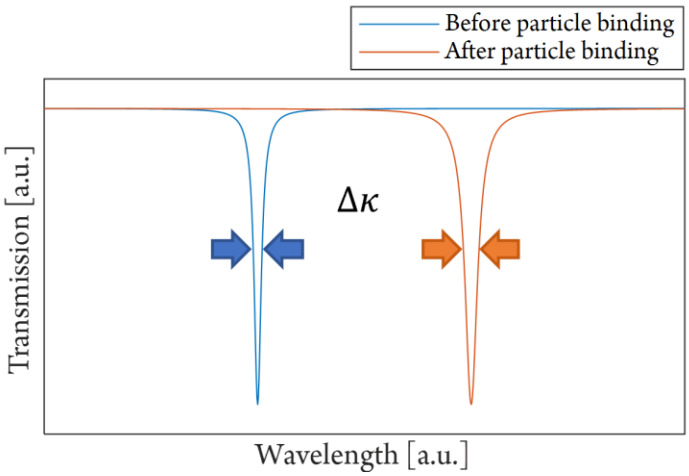

Figure 2.27. Schematic of mode broadening

2.6 Sensitivity enhancement methods

2.6.1 Frequency-locked optical whispering evanescent resonator (FLOWER)

In conventional mode shift sensing implementation, the wavelength of the tunable laser needs to be continuously scanned to obtain the complete transmission spectrum around the resonance of microcavity. A Lorentzian fit to the resonance dip is then performed to locate and track the local minimum, i.e., the position of the resonance. This approach is limited by the properties of the tunable laser and has a slow tuning and acquisition speed. The frequency locking technique is a primary method of improving the temporal resolution. This is basically an electronic feedback closed-loop system to force the wavelength of the tunable laser to align with the resonance of the microresonator. The system we are going to use in the following experimental sections is called the frequency locked optical whispering evanescent resonator (FLOWER) system (Fig. 2.28).

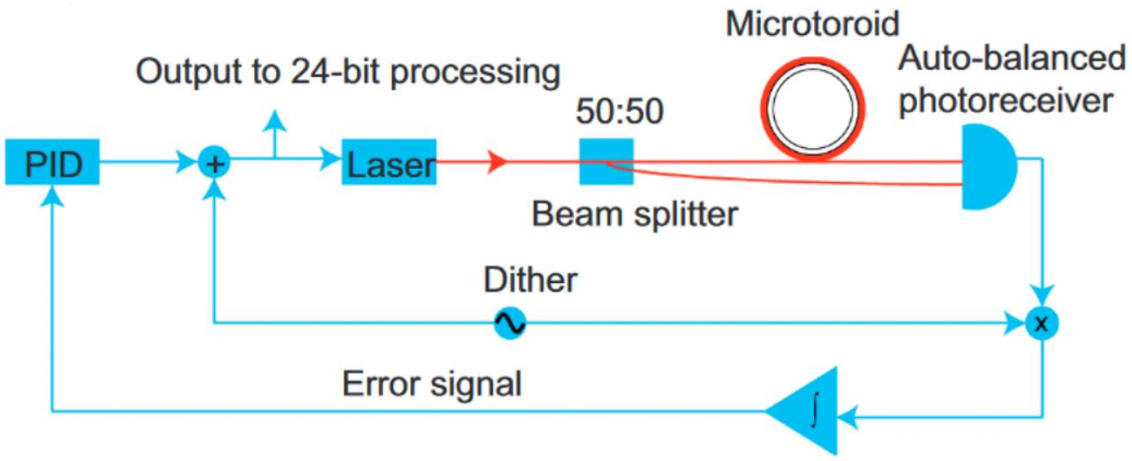

Figure 2.28. Schematic of FLOWER system[38]

In the FLOWER system, a frequency modulation dither signal created from the Digilock is sent to the laser controller. The modulated light from the tunable red laser is coupled to the toroid cavity through a taper fiber. The only light that meets the resonance conditions is confined to the cavity. The transmitted signal is then received by the auto-balanced photodetector and processed by the Digilock. Digilock calculates the time average of the product of the dither signal and the detection signal, known as the error signal, that is, the difference between the laser resonance and the WGM resonance. The error signal is regulated by the proportional–integral–derivative (PID) controller and then fed to the laser controller to align the laser wavelength with the WGM resonance. Such a close loop feedback system can effectively record wavelength shifts of the WGM cavity at femtometer (fm) level or even smaller.

2.6.2 Plasmonic enhancement

As present in Eq. 2.48, the sensing signal (wavelength shift) of a single particle is proportional to its normalized interacting E-field intensity. Normally, the evanescent tail of WGM is restricted by the shape of the microresonator and has the maximum intensity of field only around the equatorial plane. To increase the field intensity, plasmonic structures need to be introduced. The free electrons in the plasmonic particles oscillate with the background electric field, resulting in extremely strong near-field enhancement. The near field area would be available for bioparticle detection to have a larger sensing signal. This hybrid plasmonic-WGM system has been experimentally demonstrated to improve the sensitivity of the microresonator. However, researchers often do not discuss the loss of metals, i.e., the reduction of the system Q. In Chapter 3, we will propose a new trimer structure with lateral dark mode to balance the effect of metallic loss.

3 DARK MODE PLASMONIC OPTICAL MICROCAVITY BIOCHEMICAL SENSOR

Whispering gallery mode (WGM) microtoroid optical resonators have been effectively used to sense low concentrations of biomolecules down to the single molecule limit. Optical WGM biochemical sensors such as the microtoroid operate by tracking changes in resonant frequency as particles enter the evanescent near-field of the resonator. Previously, gold nanoparticles have been coupled to WGM resonators to increase the magnitude of resonance shifts via plasmonic enhancement of the electric field. However, this approach results in increased scattering from the WGM, which degrades its quality factor (Q), making it less sensitive to extremely small frequency shifts caused by small molecules or protein conformational changes. Here we show using simulation that precisely-positioned trimer gold nanostructures generate dark modes that suppress radiation loss and can achieve high ($>10^6$) Q with an electric field intensity enhancement of 4300, which far exceeds that of a single rod (~2500 times). Through an overall evaluation of a combined enhancement factor, which includes the Q factor of the system, the sensitivity of the trimer system was improved 105× versus 84× for a single rod. Further simulations demonstrate that unlike a single rod system, the trimer is robust to orientation changes and has increased capture area. We also conduct stability tests to show that small positioning errors do not greatly impact the result.

3.1 Introduction

Whispering gallery mode (WGM) microtoroids (Fig. 3.1(a)) are excellent sensors due to their ultra-high quality (Q) factors and their ability to be integrated on chip[28]–[30], [39]–[41], [12], [42], [43]. These sensors when combined with frequency-locking, balanced detection, and

data processing techniques are able to detect wavelength shifts (< ~0.005 fm) which correspond to the detection of a biomolecule of radius 2 nm binding to the microtoroid[28], [29], [39]. Coupling plasmonic particles to WGM cavities is one way to improve the sensitivity of the systems[44]. These particles increase the frequency shift upon molecular binding by providing enhanced interaction between the optical field and the analyte due to localized surface plasmon resonance (LSPR)[44], [45]. The scattering and absorption losses of the metal, however, cause degradation of the quality (Q)-factor of the resonance, that is, the broadening of the linewidth. Dark mode plasmonic resonances can help solve this problem[46]–[50], but simulation is necessary to understand the specific impact of a given plasmonic structure on the system.

Currently, due to limitations in computing performance and time consumption, a wedge-shaped model with perfect electric conductor boundary conditions is widely used in plasmonically enhanced WGM toroid simulations[51]. However, such boundary conditions act as mirrors, effectively replicating the plasmonic particle multiple times, which results in an inaccurate calculation of the coupled-system Q-factor for a single particle (see Appendix A for more details).

Here we use a three-dimensional (3D) eigenmode simulation model of a whole microtoroid with a major diameter of 10 μm to explore the interaction of a single cavity with one or several nanostructures. The model is implemented in COMSOL. Due to simulation constraints in both time and memory, we cannot accurately simulate larger whole toroids in 3D. The schematic of our 3D model and the field distribution of the fundamental TE mode is shown in Fig. 3.1(a). The polarization of the TE mode is perpendicular to the equatorial plane of the toroid cavity. Nanorods are placed perpendicular to the equatorial plane for maximum coupling and excitation, and their near field enhancement is shown in Fig. 3.1(c).

We define a figure of merit known as a combined enhancement factor (f_C) to quantify the limit of detection and resolution of our sensing system. With this figure of merit, we can predict that slightly off-resonant coupling between the plasmon and WGM provides better performance than a direct match of the WGM and plasmon resonances. Further, we discuss the improvements that a lateral dark mode supported by a plasmonic trimer structure brings to the system and verify its stability.

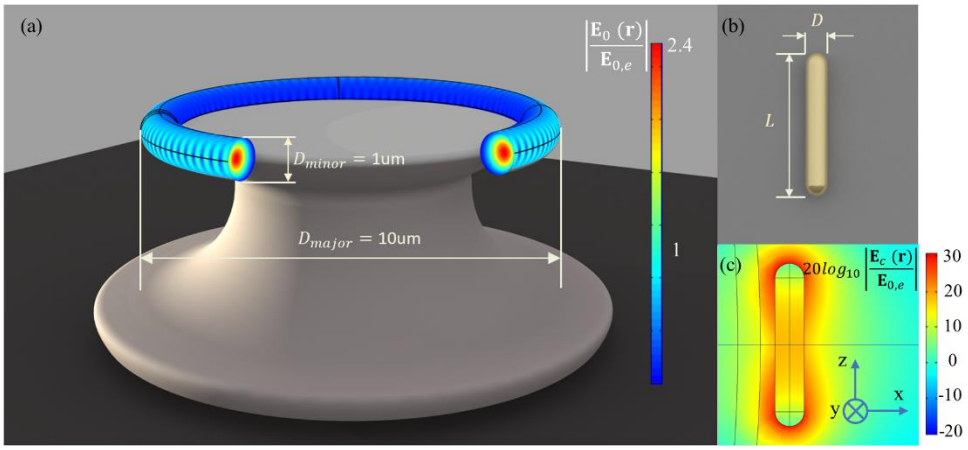

Figure 3.1. Schematic of a microtoroid cavity. (a) The E-field is normalized by the amplitude of the maximum field in the evanescent zone of the bare WGM toroid ($\mathbf{E_o}(\mathbf{r})$). (b) A rendering of a gold nanorod placed parallel to the TE polarization of the WGM cavity mode. The resonance frequency of a single rod is tuned by adjusting its aspect ratio, which is defined as the ratio of the length to the width (diameter) of the rod. (c) Field distribution of the excited dipole mode around a nanorod.

Two critical parameters affect the limit of detection of a WGM sensing system. One is the quality factor mentioned above[27], which determines the linewidth of the resonance peak in the output spectrum. Higher quality factors correspond to narrower resonances, whose central

resonance frequency can be more precisely determined and tracked[17], [28]–[30]. The other parameter is the electric field enhancement factor. The magnitude of the shift in resonance frequency of the WGM upon interaction with an analyte is proportional to this enhancement factor. According to perturbation theory[52], the frequency shift caused by a particle of volume ΔV with (possibly anisotropic) material parameters $\overleftrightarrow{\Delta\varepsilon}$ (r) and $\overleftrightarrow{\Delta\mu}$ (r) relative to the background is given by[20], [52], [53]:

$$\frac{\Delta\omega}{\omega} = -\frac{\int_{\Delta V}\left[\boldsymbol{E}_0^{\dagger}\varepsilon_0\overleftrightarrow{\Delta\varepsilon}(\boldsymbol{r})\boldsymbol{E} + \boldsymbol{H}_0^{\dagger}\mu_0\overleftrightarrow{\Delta\mu}(\boldsymbol{r})\boldsymbol{H}\right]dV}{\int_V\left[\varepsilon_0\varepsilon(\boldsymbol{r})\boldsymbol{E}_0^{\dagger}\cdot\boldsymbol{E} + \mu_0\mu(\boldsymbol{r})\boldsymbol{H}_0^{\dagger}\cdot\boldsymbol{H}\right]dV} \approx -\frac{\varepsilon_b\,\boldsymbol{E}_0^{\dagger}\,\overleftrightarrow{\alpha}(\omega)\,\boldsymbol{E}_0}{2\varepsilon_0\varepsilon_r V_m\,|\boldsymbol{E}_0|^2_{max}}, \tag{3.1}$$

where ε_0 and μ_0 are the permittivity and permeability of free space, ε and μ are relative permittivities and permeabilities, ε_b is the permittivity of the background media (in this case, vacuum), $\mathbf{E}_0$ and $\mathbf{H}_0$ are the electric and magnetic fields for an unperturbed WGM, † represents conjugate-transpose, **E** and **H** are the electric and magnetic fields within the perturbation volume, $|\mathbf{E}_0|^2_{max}$ is the maximum intensity within the unperturbed toroid, $V_m = \int_V \varepsilon_r\,|\mathbf{E}_0|^2 dV/(\varepsilon_r|\mathbf{E}_0|^2_{max})$ is the mode volume of the resonant mode[17], ε_r is the dielectric constant of silica[31], and $\overleftrightarrow{\alpha}(\omega)$ is the polarizability tensor of the particle. In the numerator, we have assumed $\overleftrightarrow{\Delta\mu} = 0$, and in the denominator, we have assumed that the magnetic field contributes an equal amount of energy as the electric field and that the perturbation has a negligible impact on the total energy stored in the cavity. The polarizability tensor for a metallic nanorod can be expressed as[54]–[56]:

$$\overleftrightarrow{\alpha}(\omega) = \begin{pmatrix} \alpha_\perp & 0 & 0 \\ 0 & \alpha_\perp & 0 \\ 0 & 0 & \alpha_\parallel \end{pmatrix}, \tag{3.2}$$

where $\alpha_{\parallel}$ and $\alpha_{\perp}$ correspond to the longitudinal and transverse modes of the nanorod, respectively. The nanorods are small enough that they can be accurately modeled based on the localized surface plasmon resonance of prolate spheroids[55]:

$$\alpha_{\parallel,\perp} = \Delta V \varepsilon_0 \frac{\varepsilon_m - \varepsilon_b}{G_{\parallel,\perp}\varepsilon_m + \left(1 - G_{\parallel,\perp}\right)\varepsilon_b}, \tag{3.3}$$

where $\Delta V = \frac{4}{3}\pi\left(\frac{d}{2}\right)^3 + \pi\left(\frac{d}{2}\right)^2 (L - d)$ is the volume of the cylindrical nanorod, ε_m is the relative permittivity of the metal, ε_b is the dielectric constant of the surrounding environment and the $G_{\parallel,\perp}$ are geometrical factors that can be respectively written as:

$$G_{\parallel} = R_s \frac{1 - e^2}{e^2}\left(-1 + \frac{1}{2e}\ln\left(\frac{1 + e}{1 - e}\right)\right) \tag{3.4}$$

$$G_{\perp} = \frac{1 - G_{\parallel}}{2}, \tag{3.5}$$

where $e = \sqrt{1 - \left(\frac{d}{L}\right)^2}$ is the eccentricity of the prolate spheroid and R_s is a parameter which describes the particle shape. Here we use $R_s = 0.88$ for a spherocylinder[57]. In the simulation, we put the rod parallel to the polarization of the fundamental TE mode and study only the influence of the longitudinal plasmon mode and its corresponding $\alpha_{\parallel}$. It is apparent that $\alpha_{\parallel}$ is greatly influenced by the nanorod aspect ratio. This in turn affects the shift of the unperturbed WGM mode.

3.2 Combined enhancement factor

Fig. 3.2(a) illustrates the frequency shift of the cavity mode around on-resonance ($\lambda \approx 774$ nm) coupling obtained in the simulation, which is consistent with both experimental data and

perturbation theory[58]. The data for the perturbation theory is obtained by numerical calculation of Eqs. (3.1–3.4) where only the longitudinal polarizability $\alpha_{\parallel}$ is necessary, and the unperturbed electric fields and mode volumes are determined from a simulation of the bare cavity. In our calculations for different aspect ratios, the nanorod diameter is held fixed while the length is varied, so at large aspect ratios, the assumption that the nanorod size $\ll \lambda$ starts to fail and the theory deviates from the numerical simulation results[59]. At the same time, the linewidth of the coupled system also varies with the resonance frequency of a single rod as shown in Fig. 3.2(b).

The inset of Fig. 3.2(c) shows how we calculate the intensity enhancement at the particle, which is done by adding a sphere in the near field of the nanorod to represent an analyte molecule. Here we use the volume integration of the electric field intensity over the volume of an analyte particle as the enhancement factor instead of the maximum E-field intensity at the hot spot of the nanoparticle[44], [60]. This is more accurate because the maximum E-field hot spot intensity is sensitive to the mesh of the simulation model and does not take into account the frequency shift caused by the size of the measured particle. The ratio of the integrated field involving a coupled plasmonic particle to that of the evanescent field of the bare toroid can be used to define a field enhancement factor as follows:

$$f_E = \frac{\int_{\Delta V} |\mathbf{E}_c(\mathbf{r})|^2 dV}{\int_{\Delta V} |\mathbf{E}(\mathbf{r})|^2 \, dV}, \tag{3.6}$$

where $|\mathbf{E}_c(\mathbf{r})|$ is the E-field magnitude of the near field of the coupled system. The enhancement factor corresponding to the electric field intensity directly affects the magnitude of the frequency shift when a particle binds to the cavity. This enhancement factor closely follows the same trend as the linewidth broadening caused by the nanorod (Fig. 3.2(b)). It is evident that introducing a

particle with a lossy material such as gold will significantly decrease the Q-factor of the system even with strong local electric field enhancement, so there is a trade-off between Q and intensity enhancement factor as shown in Fig. 3.2(c). At a wavelength of $\lambda \approx 774$ nm, the maximum $2500\times$ intensity enhancement factor is achieved when the rod aspect ratio equals 5.4. In this case, the peak LSPR wavelength coincides with the particular WGM resonance being simulated. The unperturbed, bare toroid exhibits a Q-factor of 7×10^6, which drops to 1.87×10^5 when coupled to the nanorod with an aspect ratio of 5.4.

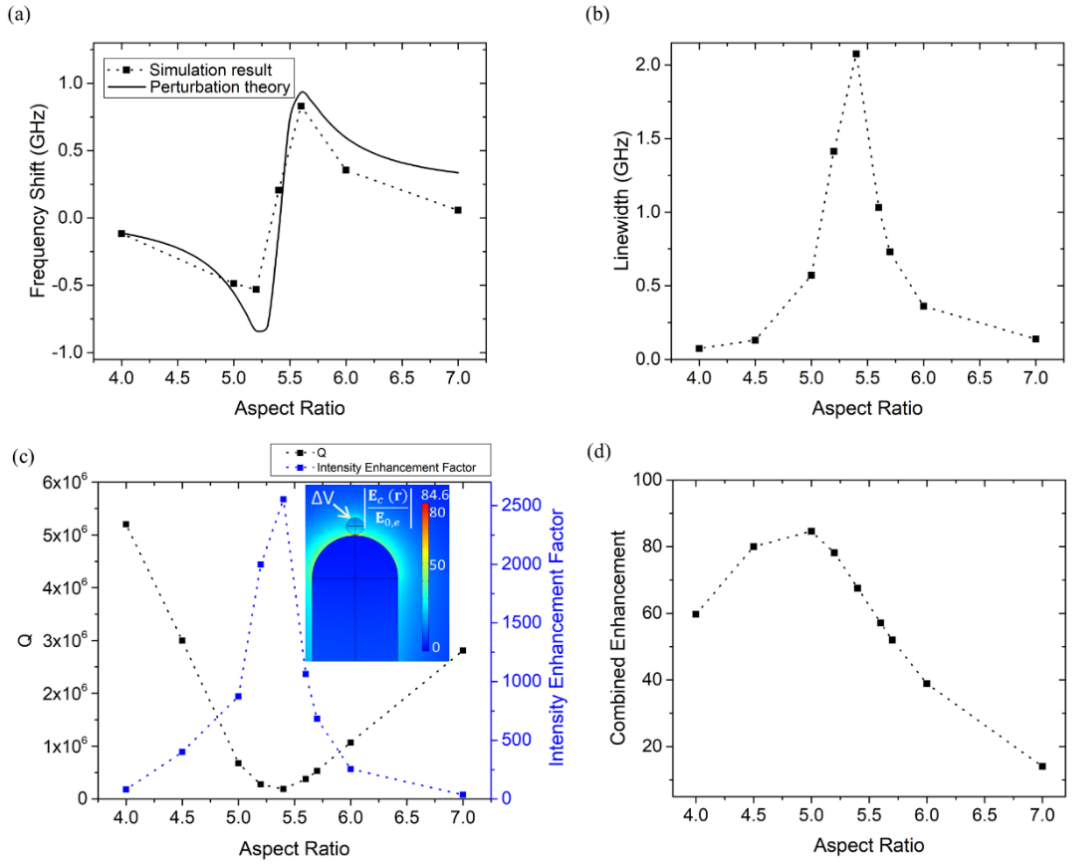

Figure 3.2. (a) The blueshift or redshift of the cavity mode around the on-resonance coupling. (b) The relationship between the linewidth corresponding to system loss and the resonance of a single rod. (c) The relationship between Q-factor and enhancement as a function of the resonance

for a single nanorod. The trend for the enhancement factor is similar to the linewidth change in Fig. 2(b). Extremely strong enhancements are shown for on-resonant coupling. Due to the light-matter interaction, a very strong hot spot is generated between the plasmonic nanorod and the biomolecule. (d) The relationship between the combined enhancement factor (f_C) and the resonance frequency of the rod.

The lower Q of the coupled system involving resonant nanorods may make it difficult to precisely lock to resonance peaks in experiments involving tracking the wavelength shift of the mode. Therefore, a balance is desired between the Q-factor and the intensity enhancement factor.

From Eqs.3.1 and 3.3, it can be shown that frequency shift is directly proportional to the E-field intensity times the volume of the detected particle: $\Delta\omega \propto E^2\,\Delta V$, for scalar α. Then, the volume of the smallest detectible particle follows, $\Delta V_{min} \propto \Delta\omega_{min}/|E|^2 \propto (Q\,|E|^2)^{-1}$, assuming that the smallest experimentally measurable shift, $\Delta\omega_{min}$, is inversely proportional to the Q factor because high-Q resonances correspond to narrow peaks that can be tracked with greater precision than broad resonances. So, the volume of the smallest detectable particle is inversely proportional to a figure of merit that accounts for both the E-field and Q-factor effects, which we call the combined enhancement factor (f_C):

$$f_C = f_Q f_E = \frac{Q_c}{Q_0} f_E, \tag{3.7}$$

where Q_c and Q_0 represent the Q-factors of the coupled and bare toroid cavity, respectively. Higher f_C values correspond to better sensitivity and/or more well-defined resonances. Unlike the peak in f_E, the highest f_C does not occur when the LSPR and WGM resonances coincide. Instead, as shown in Fig. 3.2(d), the position of the peak is shifted significantly to a smaller aspect ratio

than that of resonant coupling. We can state that the improvement to the system from a single rod with an aspect ratio of 5.0 is ideal, which corresponds to an 874× field enhancement factor and a Q-factor of 6.8×10^5. Using f_C as a figure of merit is helpful in selecting the best plasmonic structure for experimental use.

3.3 Individual nanorods coupled system

For multiple gold nanoantennas, we investigate the intrinsic properties of the coupled system. The single gold nanorod can be approximated as a nanocavity. According to coupled mode theory[36], [53], [61], [62], the equations of several coupled modes can be written as:

$$\frac{db_{WGM}}{dt} = (i\Omega_{WGM} - \Gamma_{WGM})b_{WGM} + i\kappa b_1 + i\kappa b_2 + \cdots + i\kappa b_n$$

$$\frac{db_1}{dt} = (i\Omega_1 - \Gamma_1)b_1 + i\kappa b_{\mathrm{WGM}}$$

$$\vdots$$

$$\frac{db_n}{dt} = (i\Omega_n - \Gamma_n)b_n + i\kappa b_{\mathrm{WGM}}, \tag{3.8}$$

where b_{WGM} and b_n represent the mode amplitude of the WGM mode and LSPR mode of the nth nanorod, and Ω_{WGM} and Ω_n correspond to their resonance frequencies and Γ_{WGM} and Γ_n represent their corresponding losses, respectively, which can be calculated from COMSOL using the eigenfrequency solver. The coupling coefficient is defined as a complex number κ which takes into account the frequency shift of the mode and the degradation of the Q. Because the rods in the array are spaced relatively far apart, we only consider the coupling of each LSPR mode with the

cavity and no direct interparticle coupling. Therefore, the above equations for the coupled system can be written as a matrix equation $\dot{\mathrm{M}} = H\mathrm{M}$, where $\mathbf{M} = [b_{WGM}, b_1, \ldots b_n]^T$, and

$$H = \begin{bmatrix} \Omega_{WGM} + i\Gamma_{WGM} & \kappa & \cdots & \kappa \\ \kappa & \Omega_1 + i\Gamma_1 & 0 & 0 \\ \vdots & 0 & \ddots & \vdots \\ \kappa & 0 & \cdots & \Omega_n + i\Gamma_n \end{bmatrix}, \tag{3.9}$$

The intrinsic Q factor of the coupled system can be calculated from the eigenvalues of H, corresponding to the steady-state of the system. Through the simulation data, the coupling coefficient κ (~1.43×10^{11}Hz) can be obtained from a 2×2 matrix generated by a system in which a cavity is coupled to a single rod (see Appendix B). Further, the Q factor of a $(n + 1) \times (n + 1)$ matrix corresponding to a multiple (n) rod coupled system can be calculated numerically. We compare these values with the Q factors obtained from the COMSOL simulation of the multi-rod system (Fig. 3.3(a)). The coupled mode theory can then be used to predict the interaction between the WGM and additional particles without having to run new COMSOL simulations.

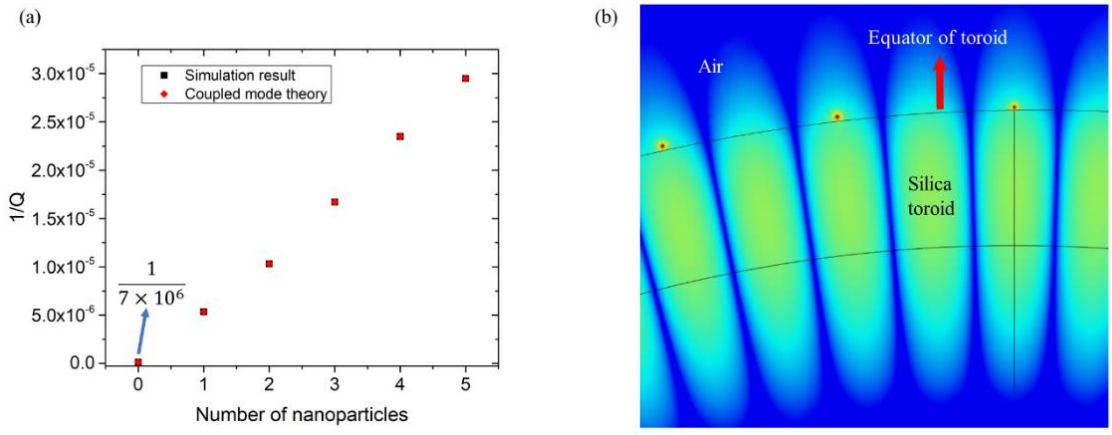

Figure 3.3. (a) The Q-factors obtained through both numerical simulations and coupled mode theory are consistent for the systems involving multiple nanorods and no direct inter-rod

coupling. (b) Top view of multiple rods coupled to the cavity mode. Fig. 3(b) and 2(c) share the same color bar.

Fig. 3.3(a) also shows the full simulation results of coupling several rods to the cavity, where each rod is placed at an antinode of the standing wave WGM (Fig. 3.3(b)). Here, the nanorods are sufficiently far apart such that direct coupling between neighboring nanorods is negligible compared to nanorod-WGM coupling, as verified in Fig. 3.3(a) by the agreement between the numerical simulation results and coupled mode theory (eigenvalues of H, Eq. 3.9).

3.3.1 The details of the full 3D toroid simulation and its comparison with the wedge model

The data and profiles are obtained in COMSOL using finite element analysis. The material of the cavity is silica with a refractive index of $1.45 + 10^{-8}i$ and the background is air[27] with a refractive index of 1. We add the imaginary component of the refractive index of the cavity to lower the Q-factor to a value similar to what we would see in the experiment. The material parameters of gold used here are those given by Johnson and Christy[63]. The diameter of each gold rod is 6 nm. The simulated biomolecule used to calculate the enhancement factor is a sphere with a refractive index of 1.5 and a radius of 1 nm. We constructed the mesh of the cavity by using a uniform sweeping method with a maximum size of one-ninth of a wavelength. The Q-factor and field distribution of the unperturbed cavity surrounded by a perfectly matched layer is consistent with the analytical solution and the two-dimensional axisymmetric model[32], [64]–[66]. The Q is calculated from the real and imaginary parts of the eigenfrequency obtained by COMSOL. In the matrix given in Eq. 3.9, the parameters Ω_{WGM} (3.8724×10^{14} Hz) and Γ_{WGM} (1.03×10^{9} Hz)

are determined from simulations of a bare toroid and the interaction of a single rod with a cavity using the eigenfrequency solver in COMSOL. Ω_n (3.8724×10^{14} Hz) and Γ_n (1.479×10^{12} Hz) are obtained from the spectrum of the nanoparticle in free space, and all rods are identical. The server used for the simulation is configured as a 56-core 2.3 GHz processor and 384 GB memory.

The wedge simulation model is currently widely used in the calculation and prediction of relevant experimental data for microresonators[51]. The model uses perfect electric conductor (PEC) boundary conditions which can be considered as mirrors. Such boundary conditions apply only to bare cavities, but when the cavity is coupled to a nanoparticle (NP) or structure, the PEC boundary conditions replicate the nanoparticles multiple times, such that the interaction between one nanoparticle and the WGM cannot be accurately predicted.

Here we study the effect of the wedge angle on the Q value. The Q value decreases with the increasing number of coupled NPs. To compare the wedge model with a whole 3D model, we construct both models for a toroid with a major radius of 5 microns. Fig. 3.4(a) shows the schematic of the wedge model. The wedge angle θ is inversely proportional to the number of azimuthal modes m, and can be written as:

$$\theta = N\frac{\pi}{m}, \tag{3.10}$$

where N is an integer corresponding to the number of antinodes of the standing wave in Fig. 3.4(b). m satisfies the resonance condition $m\lambda = 2\pi n_{eff}R$, where n_{eff} represents the effective refractive index of the mode. The N in the wedge structure is taken as 1, 3, 5, 7 and compared with the whole toroid model which is used in the main text. The corresponding field distribution for the N = 7 case is shown in Figs. 3.4(b) and (c).

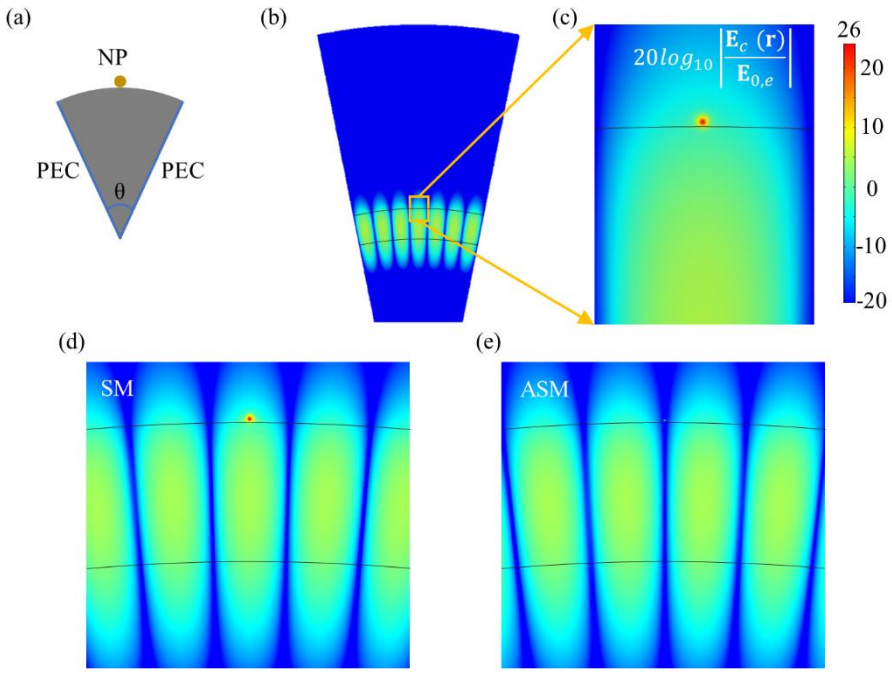

Figure 3.4. (a) Schematic of the wedge model. (b) Electric field distribution of a particle coupled to a toroid cavity (top view). The particle is placed at the antinode. (c) A zoom-in of near field enhancement. (d) and (e) show the symmetric and asymmetric modes of the coupled system obtained by the whole 3D model using an eigenfrequency solver, respectively. The corresponding detuning frequency between the SM and ASM modes is 200 MHz.

The Q of the wedge structure is significantly lower than that of the whole toroid and one particle. This may be because the larger the wedge angle, the lower the number of coupled particles, so the higher the Q. But we don't know the interaction of a single rod and a cavity, nor can we calculate the influence of boundary conditions on the electric field and its influence on the coupled system.

N	1	3	5	7	Whole toroid
Q-factor	8.10×10^3	2.41×10^4	4.04×10^4	5.62×10^4	1.87×10^5

Table 3.1. Q-factor of the coupled system for different wedge angles. The last column is the result of the whole toroid model coupled to a single rod of the same size.

Furthermore, when a nano-scatterer is coupled to the WGM cavity, the coupling of the scattered light to the clockwise mode and counter-clockwise mode of the cavity will generate both a symmetric mode (SM) and an asymmetric (ASM) mode[67]. Symmetric and asymmetric modes correspond to the antinode or node of the standing wave where the particle is located, respectively. Since the PEC boundary condition sets the electric field to zero at the boundary, the position of the WGM standing wave at a specific wavelength is fixed. Accordingly, the introduced nanoparticle does not interact with both the SM and ASM simultaneously. The 3D whole toroid model, however, can generate two modes as shown in Figs. 3.4(d) and (e). This is another advantage of the whole toroid model. Therefore, the whole toroid model is used here rather than the wedge model.

3.3.2 Coupling coefficient calculation

$\Omega_{WGM} + i\Gamma_{WGM}$ and $\Omega_1 + i\Gamma_1$ can be obtained from the eigenfrequency in the bare toroid simulation and the isolated nanorod, respectively. If we assume that the complex eigenfrequency of the coupled system is $\Omega_{coupled} + i\Gamma_{coupled}$ which can be solved from the simulation of the bare toroid coupled to a single nanorod, then from the analytical eigenvalue of the 2×2 matrix, we can calculate κ using:

$$\kappa = \left[\left(\Omega_{WGM} + i\Gamma_{WGM} - \Omega_{coupled} - i\Gamma_{coupled}\right)\left(\Omega_1 + i\Gamma_1 - \Omega_{coupled} - i\Gamma_{coupled}\right)\right]^{\frac{1}{2}} \qquad (3.11)$$

3.4 Trimer-induced lateral dark mode

The dipole modes induced in isolated antennas lead to large energy radiation which adversely limits the Q-factors of the coupled systems. Dark modes, an example of which is the antibonding interaction of dipolar resonances, have a longer lifetime and lower loss compared to bright dipolar modes, but their excitation is not easily feasible from the far-field[46], [47], [50]. Due to the nearly zero net dipole moment of dark plasmons, it is almost impossible for their out-of-phase state to interact with light in free space.

Here we designed a plasmonic trimer consisting of three isolated rods arranged in a symmetric triangle[68], [69] (Fig. 3.5(a)) such that the microtoroid WGM excites one of the nanorods in the trimer, which in turn excites a dark mode resonance (lateral dark mode) of the other two nanorods[46], [49], [70]–[72]. Coupling of the dark mode and WGM standing wave can significantly reduce the degradation of the Q-factor. The superposition of rod near-fields at the center of the trimer can also bring greater intensity enhancement factors. Fig. 3.5(b) shows the spectrum of the lateral dark mode of a trimer and three individual rods in free space. When the ends of three rods exhibit the same charge distribution, we call it a breathing dark mode. Only when two antennas of the trimer generate an antibonding mode (Fig. 3.5(b)) do we refer to this as a lateral dark mode. Although the trimer spectrum exhibits a peak near 800 nm upon far-field or WGM excitation, we still call its mode a lateral dark mode because the laterally-oriented lower two rods of the trimer are excited in an anti-bonding, or dark, mode. The apparent resonance peak in Fig. 3.5(b) is due to the excitation of the vertical rod, which remains bright. Because of this simultaneous combination of bright and dark modes, it is possible to excite a plasmon resonance with minimal scattering and absorption losses. Although the breathing dark mode has much lower loss and its corresponding resonance peak is almost covered by the tail of the lateral dark mode,

its coupling to the WGM is very weak. Therefore, this simulation mainly studies the lateral dark mode instead of the breathing dark mode.

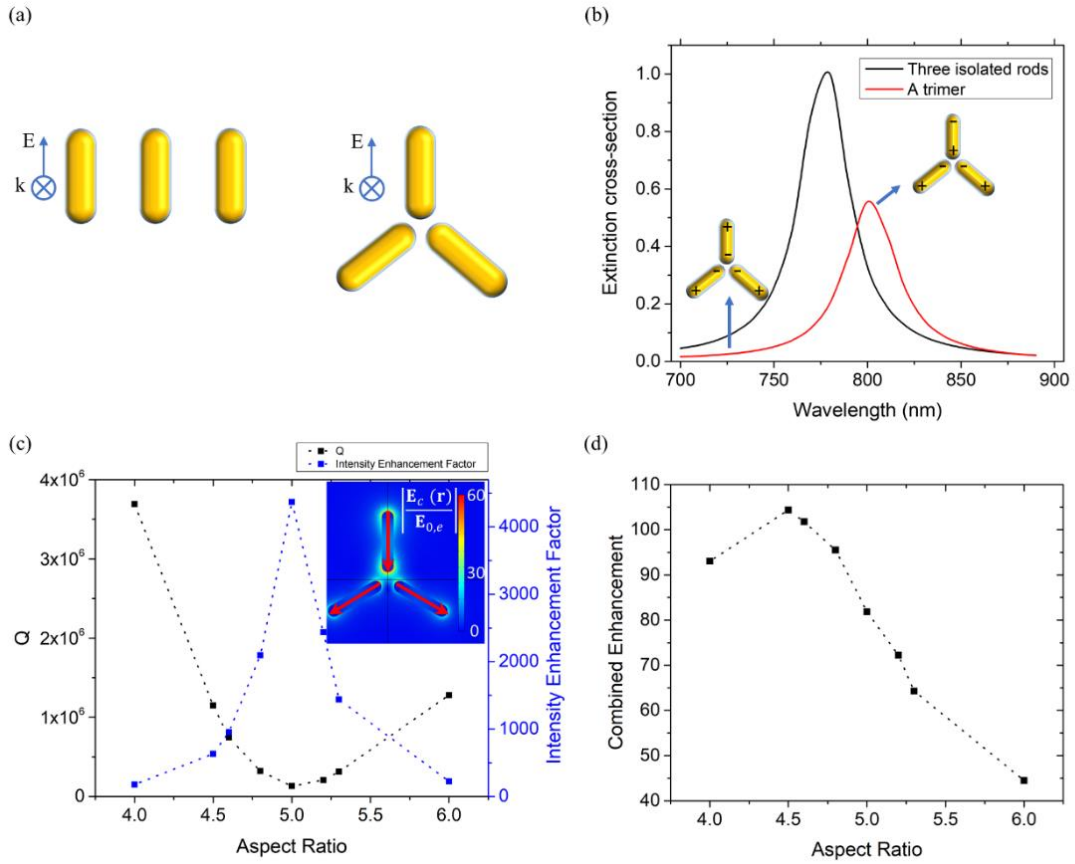

Figure 3.5. (a) Plane wave excitation for three isolated rods and a gold trimer. (b) Spectral comparison of the total extinction cross section of the lateral dark mode versus the three isolated rods from Fig. 4(a). The lateral dark mode is excited at the peak wavelength of the red curve. The illustrations show the charge distribution of the breathing and lateral dark mode at different wavelengths. Because the coupling between the breathing dark mode and free-space radiation is so small, no peak is visible at its resonance around 725 nm. (c) Scan of two parameters of the trimer (lateral dark mode) coupling system by tuning the aspect ratio of the individual rods. The red arrows show the current density direction obtained in COMSOL. The inset shows the field

distribution of excited lateral dark mode. The characteristic dark spot between the ends of the bottom two rods is clearly visible. (d) Plot of the f_C of the trimer. The lateral dark mode exhibits a higher combined enhancement value than that obtained from coupling a single rod to the cavity alone.

Due to the plasmonic coupling between closely-placed nanorods, the resonance position of the lateral dark mode shifts with respect to the spacing and position of the rods. In Fig. 3.5(b), we compare the extinction cross sections when three rods with the same aspect ratio of 5.4 are placed separately or placed as a trimer with an 8 nm central gap. The extinction cross sections are normalized by that of the three isolated rods. The maximum extinction of the trimer is about half of that obtained from three individual rods. At many wavelengths, including 774 nm, corresponding to the WGM resonance, the loss from the trimer is even lower than that of a single rod. Such a low-dissipation mode improves the WGM sensing system.

We also adjust the aspect ratio of the three rods in the trimer to optimize the improvement of the trimer coupling system. Fig. 3.5(c) shows how the Q-factor and intensity enhancement vary with the rod aspect ratio. The biggest intensity enhancement factor here corresponds to the case where the spherical analyte particle is placed in the center of the trimer. At an aspect ratio of 5, the maximum field enhancement factor (~4300×) is much larger than that of a single rod (~2500×), as mentioned above. At the same time, the Q-factor of 1.31×10^5 is similar to that of the single rod case (~1.87×10^5) at on-resonance coupling and is twice as large as the Q for the three rods case (~5.98×10^4) presented in Fig. 3.3(a). Even the relatively dark region just below the center of the trimer in the inset of Fig. 3.5(c) can bring dozens of times of intensity enhancement, which also demonstrates that the trimer structure is beneficial to increasing capture area for biomolecule

detection. The maximum f_C of the system is ~105, which is achieved using the trimer with a rod aspect ratio of 4.5. This f_C is also significantly larger than that of a single rod (~84).

To test the robustness of our system, we studied the effect of tilted angle perturbation, length perturbation, and inter-rod spacing on f_C. Here we chose the trimer with a rod aspect ratio of 4.5 mentioned above as a reference. As shown in the insets in Fig. 3.6, we observe the difference of f_C in the system by introducing different geometric perturbations. Considering the need to bind biomolecules at the center of the trimer in experiments, the spacing between the rods should not be too small. Although different perturbations will impact the Q-factor or enhancement factor of the system, the overall f_C changes little from its initial value 105. The spacing in Fig. 3.6(c) has little effect on the loss caused by the structure, so the corresponding Q value is almost unchanged, and the observed variation is primarily due to E-field enhancement.

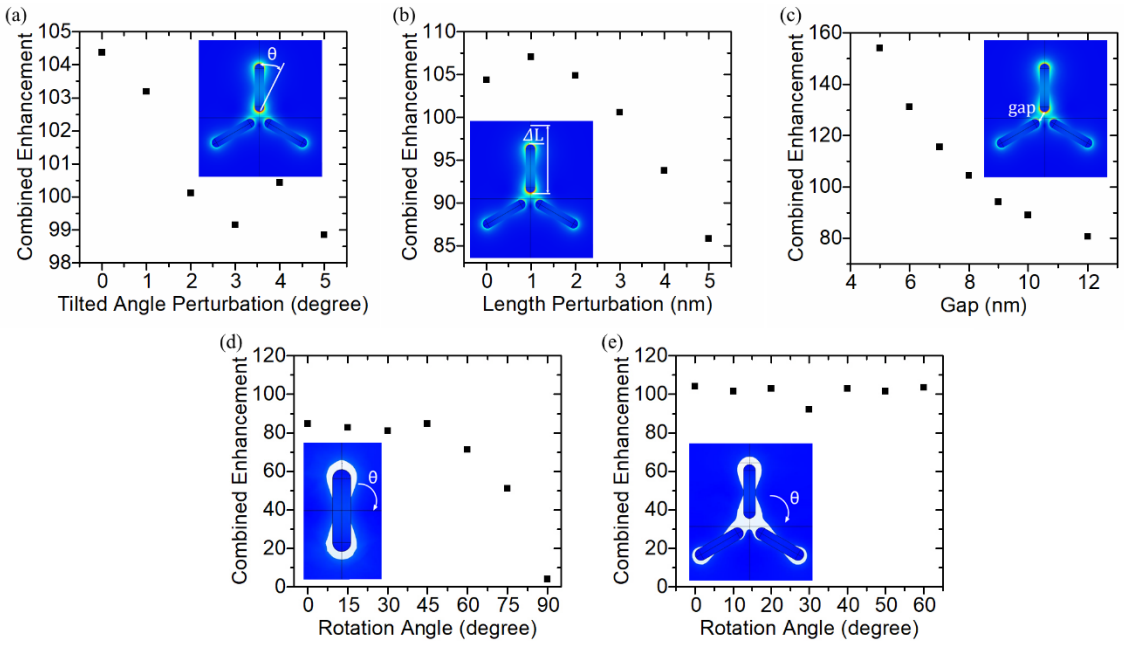

Figure 3.6. Influence of different perturbations on the trimer's combined enhancement factor (a) and (b) Small changes in angle and length can maintain the f_C. (c) To ensure that the gap space is

large enough for particles to bind, we study the effect of the spacing on the system when the spacing is greater than 5 nm. The illustrations for the trimer field distribution use the same color bar as in Fig. 3. (d) The f_c of a single rod system decreases with increasing rotation angle. When the rod is rotated 90 degrees, that is, perpendicular to the polarization of the TE mode, the overall system improvement f_C is only 4×. The white area in the inset shows where the magnitude of the E-field is 10× greater than that of a bare cavity. (e) The rotation of the trimer has little effect on f_c. The white area in the inset shows where the magnitude of the E-field is 10× greater than that of a bare cavity. The enhancement area provided by the trimer (e) is slightly more than twice that of a single rod (d).

Rotations of the entire structure are evaluated for single nanorods and trimer structures in Figs. 3.6(d) and 3.6(e). The gold nanorods in current plasmonic-enhanced WGM systems are randomly attached to the surface of the cavity and their orientation is challenging to control. Here we use a rod with an aspect ratio of 5 (Fig. 3.2) to study the influence of the rotation angle on f_C. When the rotation angle is greater than 45 degrees, the f_C decreases as the rotation angle increases (Fig. 3.6(d)) due to a mismatch with the polarization direction of the WGM. The system has only 4× gain when rotated 90-degrees. In comparison, the trimer is robust to orientation changes. Due to its rotational symmetry, we only rotate the whole trimer from 0 to 60 degrees (Fig. 3.6(e)). The 0-degree point corresponds to the idealized trimer composed of three rods with an aspect ratio of 4.5. The weakest f_C at a 30-degree angle is 92×, which is only 11.5% lower than the maximum enhancement of 104×. The trimer system is much less affected by the rotation angle than the single rod system. The inconsistent signal amplification caused by the rotation of a single rod can add uncertainty to particle detection experiments.

3.5 Conclusions

In this work, we present a lateral dark mode of a symmetric trimer structure generated using whispering gallery mode excitation and define a combined enhancement factor to analyze the improvements it brings to the system. The trimer exhibits a ~105× combined enhancement factor vs 84× for a single rod. We also demonstrate the stability and robustness of the trimer structure. We verify the correctness of our simulation from the frequency shift and linewidth changes caused by detuning and the effect on the Q-factor. Compared to the existing single-rod plasmonic hybrid WGM system, the trimer system exhibits higher enhancement, stability, and greater contact area for particle detection. In future work, we plan to use high-precision optical tweezers[73], [74] to position trimer microresonator systems for biological sensing experiments.

4 PART-PER-TRILLION TRACE SELECTIVE GAS DETECTION USING FREQUENCY LOCKED WHISPERING GALLERY MODE MICROTOROIDS

Rapid detection of toxic and hazardous gases at trace concentrations plays a vital role in industrial, battlefield, and laboratory scenarios. Of interest are both sensitive as well as highly selective sensors. Whispering gallery mode (WGM) microresonator-based biochemical sensors are among the most sensitive sensors in existence due to their long photon confinement times. One main concern with these devices, however, is their selectivity towards specific classes of target analytes. Here, we employ frequency locked whispering gallery mode microtoroid optical resonators covalently modified with various polymer coatings to selectively detect the chemical warfare agent surrogate diisopropyl methylphosphonate (DIMP) as well as the toxic industrial chemicals formaldehyde and ammonia at parts-per-trillion concentrations. This is 1-2 orders of magnitude better than previously reported, depending on the target, except for pristine graphene and pristine carbon nanotube sensors, which demonstrate similar detection levels but in a vacuum and without selectivity. Selective polymer coatings include polyethylene glycol (PEG) for DIMP sensing, accessed by the modification of commercially available materials, and 3-(triethoxysilyl)propyl-terminated polyvinyl acetate (PVAc) for ammonia sensing. Notably, we developed an efficient one-pot procedure to access 3-(triethoxysilyl) propyl-terminated PVAc that utilizes cobalt-mediated living radical polymerization and a nitroxyl polymer-terminating agent. Alkaline hydrolysis of PVAc coatings to form polyvinyl alcohol (PVA) coatings directly bound to the microtoroid proved to be reliable and reproducible, leading to WGM sensors capable of the rapid and selective detection of formaldehyde vapors. The selectivity of these three polymer

coatings as sensing media was predicted, in part, based on their functional group content and known reactivity patterns with the target analytes. Furthermore, we demonstrate that microtoroids coated with a mixture of polymers can serve as an all-in-one sensor that can detect multiple agents. We anticipate that our results will facilitate rapid early detection of chemical agents, as well as their surrogates and precursors.

4.1 Introduction

Toxic and hazardous gases pose a threat to human health in the industry, on the battlefield, and in laboratories. These gases are often colorless and odorless at low, but still harmful, concentrations, making their detection challenging. Accurate and rapid low concentration detection of these agents and their precursors can provide an early warning. Several gas sensing technologies and concepts emerged[75]–[79], all with different advantages and disadvantages in terms of their sensitivity, selectivity, stability, ease of preparation, expense, and portability. In particular, sensors based on pristine graphene and carbon nanotubes have demonstrated ultra-low limits of detection (sub-ppt) in response to nitric oxide, but lack selectivity to other gases and exhibit significant lab-to-lab variations in sensitivity[80], [81]. Whispering gallery mode (WGM) microresonators stand apart from the rest of these biochemical sensors due to their long (on the order of nanoseconds) photon confinement times,[23]–[25], [28], [29], [82], [83] which causes increased interaction of light with matter and enables these devices to be ultra-sensitive sensors.[84], [85] Here, we use a system previously developed in our lab known as FLOWER (frequency locked optical whispering evanescent resonator), which combines WGM technology with noise reduction techniques for sensitive detection of diisopropyl methylphosphonate (DIMP), ammonia (NH_3), and formaldehyde (CH_2O)[28], [29], [82]. We expand the selectivity of this

technique using custom synthesized polymer coatings thus creating both an ultra-sensitive as well as the selective on-chip sensor.

In this work we outline the working principle of FLOWER and then describe the chemical syntheses of siloxy-terminated polymer films and the microtoroid coating method, followed by a detailed account of three different polymer-coated microtoroids containing polyethylene glycol (PEG), polyvinyl acetate (PVAc), and polyvinyl alcohol (PVA), to achieve the selective sensing of DIMP, ammonia, and formaldehyde vapors. Crucially, we find that PEG, PVAc, and PVA coatings each provide high sensitivity and selectivity for only one of the three target analytes. The limits of detection for each of these selective WGM sensors are in the parts per trillion regime. We also evaluate the stability of these polymer-coated toroids as a function of their sensing ability over time (Fig. 4.1). Finally, microcavity resonators coated with a mixture of PEG and PVAc lead to sensitivity and selectivity measurements consistent with those of the separate polymers, demonstrating the detection of multiple target analytes by a single WGM sensor.

4.1.1 FLOWER and gas vapor detection mechanism

In FLOWER, trace signals are detected by locking the frequency of the laser to the resonance frequency of the microresonator cavity (Fig. 4.1 (a)). The resonance condition of the microcavity is given by [20], [23]:

$$m\lambda = n_{eff} \cdot 2\pi R, \tag{4.1}$$

where m is the azimuthal mode number, n_{eff} is the effective refractive index of the WGM, and R is the principal radius of the microcavity. As molecules enter the evanescent field of the resonator, the resonance frequency of the cavity shifts. The laser frequency shifts accordingly and is used to

measure the change in resonance frequency of the cavity. Light is evanescently coupled into the microcavity resonator using a tapered optical fiber and quasi totally internally reflects around the rim. The transmitted signal through the optical fiber is received by an auto-balanced photoreceiver and multiplied by a dither signal to generate an error signal that is the difference between the laser frequency and the microcavity resonance frequency.

For these experiments, we use microtoroid optical resonators due to their high quality (Q) factors and on-chip fabrication. High Q enables precision tracking of the resonance. It is defined as $Q = \frac{\lambda_{Res}}{\lambda_{FWHM}}$, which is the ratio of the resonant wavelength to the linewidth. The Q of the uncoated toroid is typically $10^6 - 10^8$. Chemical coatings can introduce scattering losses and thus lower the Q factor. However, in our study, a uniform thin film polymer coating on the surface of the toroid enables a post-coating $Q > 5 \times 10^5$.

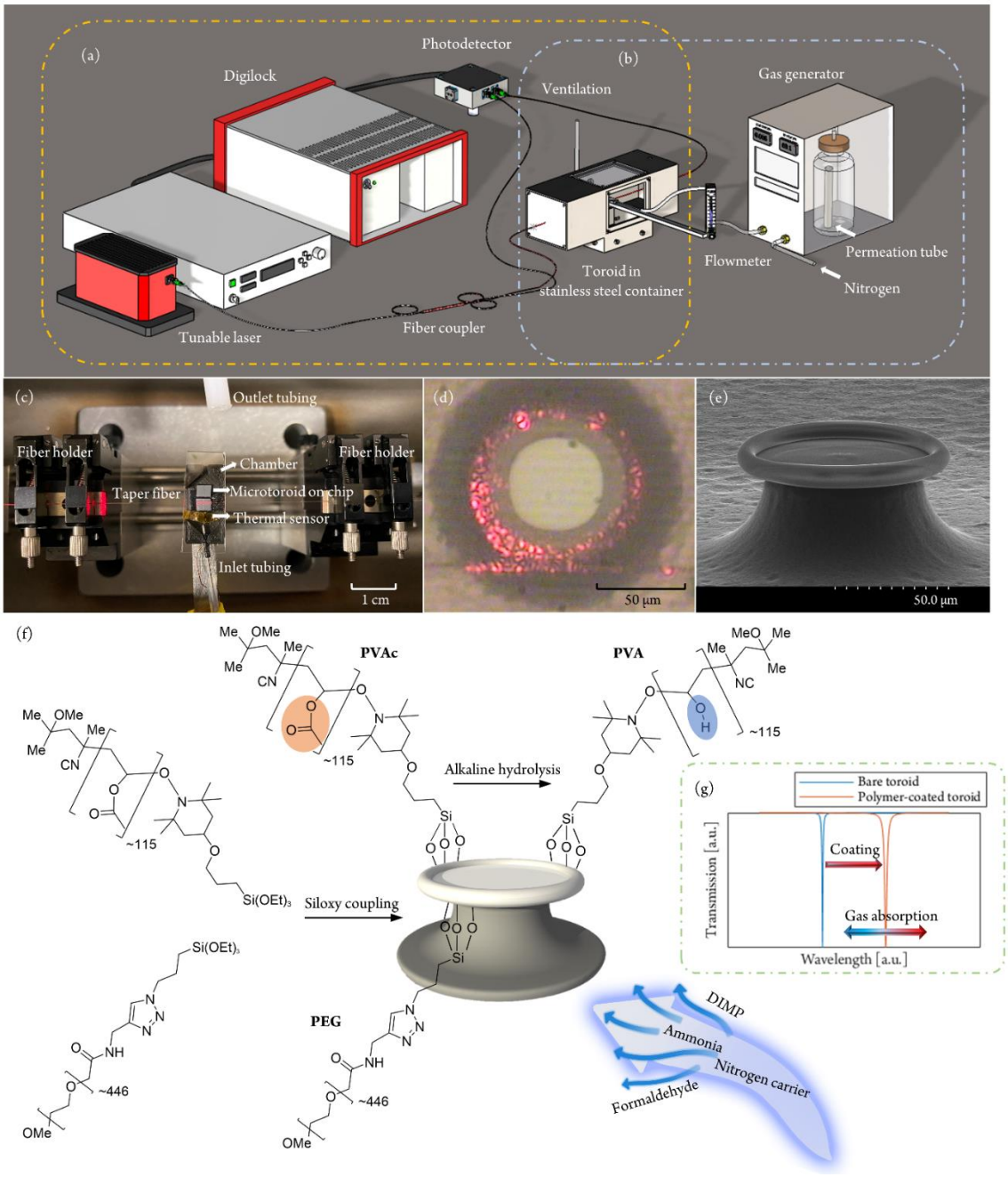

Figure 4.1. FLOWER gas detection system (not to scale). (a) In FLOWER, light from a tunable laser centered at 636 nm is frequency locked to the cavity resonance for high precision tracking of the toroid resonance as molecules enter its evanescent field. (b) For gas sensing purposes, the toroid is enclosed in a vented stainless-steel chamber. Desired chemicals of interest are heated

and directed into the chamber at a known concentration (c) Photograph of toroids mounted on the sample stage. A commercial temperature probe is placed near the inlet tubing to monitor airflow temperature changes. (d) Top view of an optical fiber evanescently coupled to a microtoroid resonator. (e) Scanning electron micrograph of a microtoroid. The toroids used in these experiments are ~ 80 microns in diameter. (f) Schematic diagram of microtoroid gas sensor and gas detection process. The polymer layer is coated on the toroid surface using siloxy coupling chemistry and reacts selectively with the low concentration of target gas carried by the nitrogen. The orange and blue shaded ovals highlight the difference between PVAc and PVA. (g) The sensing mechanism of the wavelength shift induced by the coating and chemical reaction corresponding to the processes shown in (f). Ultra-thin polymer coatings still introduce slight radius changes that cause a shift to longer wavelengths (red shifts), and the associated scattering losses broaden the resonance The signal change due to the absorbed gas is determined by both a change in radius of the microcavity and a change in refractive index.

As the target gas diffuses into the polymer coating, the refractive index change and the polymer swelling contribute to a change in cavity resonance conditions, as shown in Fig. 4.1(g), which can be expressed as[86]–[88]:

$$\frac{\Delta\lambda}{\lambda} = \frac{\Delta n}{n} + \frac{\Delta R}{R}, \qquad (\mathbf{4.2})$$

where R is the major radius of the toroid, n is the refractive index of the polymer-toroid system, and λ is the resonance frequency of the toroid. The interaction of gas vapors with a polymer may lead to sorption, which involves the accumulation of the analyte on or within the polymer coating, or chemical reactions that directly modify the structure of the polymer. These two distinct processes are likely to have varying impacts on the resonance wavelength of the FLOWER gas

sensor by affecting both the effective refractive index and principal radius of the system. In the course of designing a FLOWER gas sensor, we posited that well-known chemical reactions could provide a basis for the selective detection of low concentrations of gas vapors, wherein the functional groups of a polymer coating are chemically modified by the analyte(s) of interest, leading to a distinct change in refractive index.

We identified two distinct, well-established chemical reactions that could potentially allow for the sensitive and selective detection of specific trace gas vapors, namely the irreversible deacetylation of esters by ammonia and the reversible 1,2-addition of alcohols to formaldehyde.[89]–[92] These reactions, as depicted in Figure 4.2, inspired our evaluation of polyvinyl acetate (PVAc) and polyvinyl alcohol (PVA) as coatings in WGM gas sensing devices. Notably, PVAc has previously been employed as a sorbent medium in ammonia gas sensing devices (LOD = 23 ppm),[93] and PVA has been utilized in films for formaldehyde sensing in aqueous solution (LOD = 3.82 ppb).[94] We also wished to compare the relative sensing abilities of these two polymers with that of polyethylene glycol (PEG), a polar, chemically robust polymer that is readily available in a variety of molecular weights. Through the evaluation of these three polymers, we hoped to establish whether these well-defined chemical reactions could provide a basis for detecting gas vapors with a WGM sensor.

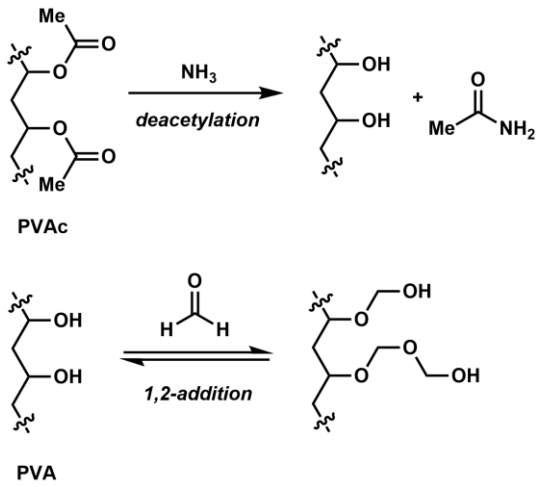

Figure 4.2. Chemical reactions proposed to enable the low concentration detection of gaseous ammonia and formaldehyde with polyvinyl acetate (PVAc) and polyvinyl alcohol (PVA) coatings on WGM gas sensors.

4.2 Materials and Methods

4.2.1 Gas generation

Part-per-trillion gas generation is done via a mass flow generator (Kin-Tek FlexStream with secondary dilution module). The compound to be detected is stored in a permeation tube as a solid or liquid at room temperature. When heated to a particular temperature, it is released at a specific rate that is pre-calibrated by gravimetric determination of weight loss. The released gas is diluted, mixed with nitrogen, and then delivered into a stainless-steel container, eventually reaching the toroid sensor. The sealed stainless-steel container is directly connected to a ventilation system. Temperature changes due to airflow are monitored by a commercial temperature sensor (Amphenol SC30F103A and Thorlabs MTD415LE TEC Driver) at the air inlet.

4.2.2 Preparation of polymer-functionalized microtoroids

A silica microtoroid resonator is fabricated as previously described.[12] Briefly, silicon wafers are purchased with a 2-micron thick layer of silica on top (UniversityWafer, Inc). A combination of photolithography and etching steps is used to create a microdisk structure. Finally, a CO_2 laser (SYNRAD, 48-2KAL) is used to melt the surface of the microdisk to form a smooth toroidal structure.

To covalently bind the polymer coatings, a freshly reflowed silica microtoroid chip was first baked on a hotplate at 60°C-70°C for 5 minutes to remove surface moisture. The chip was plasma-treated for 30 s using a handheld high-frequency generator (ETP, BD-10AS) to clean the surface as well as improve the hydrophilicity. Then the chip was immediately immersed in a 6 mM solution of the desired siloxy-terminated polymer for 2 hours. PEG-20k and PVAc-10.5k used chloroform and 95% Dimethyl sulfoxide (DMSO) as solvents, respectively. After silane deposition, the chip was rinsed with its respective reaction solvent and blown dry with a stream of nitrogen. A PVA coating was accessed from PVAc through a 3 mM 200 μL KOH/MeOH treatment at 45°C for one hour. Finally, the chip was baked at 60°C for 30 min to remove the solvent and kept under a vacuum until needed. For the multilayer coating, a mixture of PEG and PVAc was solubilized with chloroform to form a 3 mM / 3 mM PEG / PVAc solution. The coating procedure then followed the same steps as the PEG-20k coating method.

4.2.3 Polymer Synthesis and Characterization

All reactions were carried out with dry and degassed solvents unless noted otherwise. Vinyl acetate, V-70 (2,2'-Azobis(4-methoxy-2,4-dimethylvaleronitrile), $Co(acac)_2$ [cobalt(II)

acetylacetonate], HOSu (*N*-hydroxysuccinimide), EDC•HCl [*N*-(3-Dimethylaminopropyl)-*N*′-ethylcarbodiimide hydrochloride], (3-aminopropyl)triethoxysilane, and triethylamine were obtained commercially and used without further purification. Nitroxide A (*vide infra*) was synthesized from 4-hydroxy TEMPO (4-Hydroxy-2,2,6,6-tetramethylpiperidine 1-oxyl) according to a reported procedure.[95] (3-azidopropyl)triethoxysilane was synthesized from (3-chloropropyl)triethoxysilane and sodium azide according to a reported procedure.[96] Alkyne-terminated poly(ethylene glycol) (5000 g/mol, catalog number A3177-1/M-ALKYNE-5000) and carboxylic acid-terminated poly(ethylene glycol) (20000 g/mol, catalog number A3089-1 / M-CM-20K) were obtained from JenKem Technology and used as received. ^{1}H NMR spectra were recorded on a Bruker 400 MHz spectrometer and are reported relative to residual $CHCl_3$ (δ 7.26 ppm) or CHD_5 (δ 7.16 ppm). Analytical size exclusion chromatography (SEC) was performed using an Agilent 1260 series pump equipped with two Agilent PLgel MIXED-B columns (7.5 x 300 mm), an Agilent 1200 series diode array detector, a Wyatt 18-angle DAWN HELEOS light scattering detector, and an Optilab rEX differential refractive index detector. The mobile phase was THF at a flow rate of 1 mL/min. Molecular weights and molecular weight distributions were calculated by light scattering using a dn/dc value of 0.0502 mL/g (25 C) for poly(vinyl acetate) in THF.[97]

4.2.4 Polymer stability: fluorescence test

To ensure that PEG is uniformly and efficiently deposited on the microtoroid surface, we performed fluorescence tests using cholera toxin subunit B Alexa Fluor 546 dye (CTB AF546 dye). PEG has commonly been reported to prevent non-specific protein adsorption and reduce bio-fouling[98]–[100]. Three chips were used for this fluorescence test, one bare chip, one freshly

coated chip, and one coated and used for one week. First, all three chips were incubated with 0.05 mg/mL CTB AF546 conjugate for 1 hour and rinsed with Tris-NaCl buffer before fluorescence imaging. The fluorescence test results are shown in Figure 4.3. The bare toroid shows higher fluorescence intensity due to stronger non-specific protein binding. The chip after one week of use shows almost the same fluorescence intensity as the bare chip (Figures 4.3), which means that the PEG coating may have detached or otherwise degraded and can no longer block protein binding. In Figures 4.3(b)(e), fluorescence is barely visible in the freshly prepared chips, confirming that PEG is uniformly bound to the toroid surface. In gas sensing experiments, a nearly identical sensing signal is usually obtained for up to three days following fresh functionalization, after which the signal gradually decreases. The sensing results are consistent with the fluorescence test results. Occasionally, it is possible to obtain chips that maintain their sensitivity for more than a week.

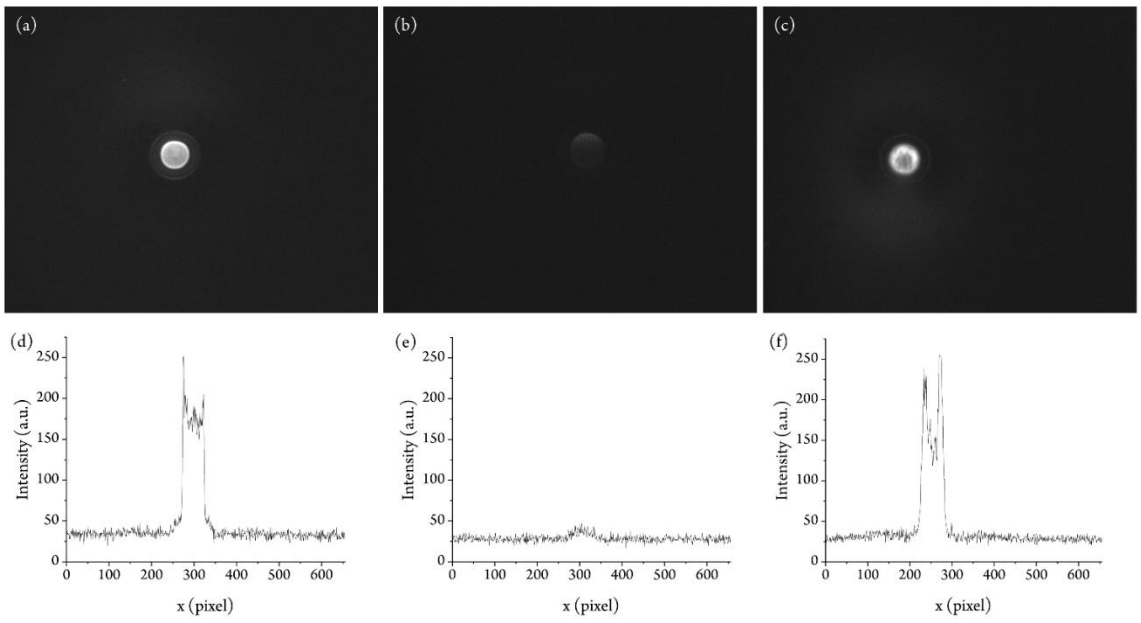

Figure 4.3. PEG coating confirmation via imaging the nonspecific adsorption of a fluorescent protein. Fluorescence images of (a) a bare toroid, (b) a fresh PEG-coated toroid, and (c) a PEG-coated toroid after having been used for one week. (d)(e)(f) are the fluorescence intensities along

the x-axis corresponding to (a)(b)(c), respectively. A low fluorescence intensity indicates the presence of a complete PEG coating that resisted the nonspecific adsorption of the fluorescent dye.

4.2.5 Synthesis and deposition of polymer coatings

With consideration of literature precedent, we synthesized polymers with a (3-triethoxysilyl) propyl group to allow for efficient conjugation of an activated silica surface.[101] Samples of (3-triethoxysilyl) propyl-terminated polyethylene glycol (PEG) of two different molecular weights, 5000 Da and 20000 Da, were accessed by the chemical modification of commercially-available end-functionalized PEGs (Figure 4.4). Specifically, (3-triethoxysilyl) propyl-terminated PEG-5000 (siloxyPEG-5000) was accessed via a copper-catalyzed alkyne-azide cyclization from the corresponding alkyne-terminated PEG and (3-azidopropyl) triethoxysilane. 3-triethoxysilyl propyl-terminated PEG-20000 (siloxyPEG-20000) was synthesized by an amidation reaction between a succinimidyl ester-terminated PEG and (3-aminopropyl) triethoxysilane.

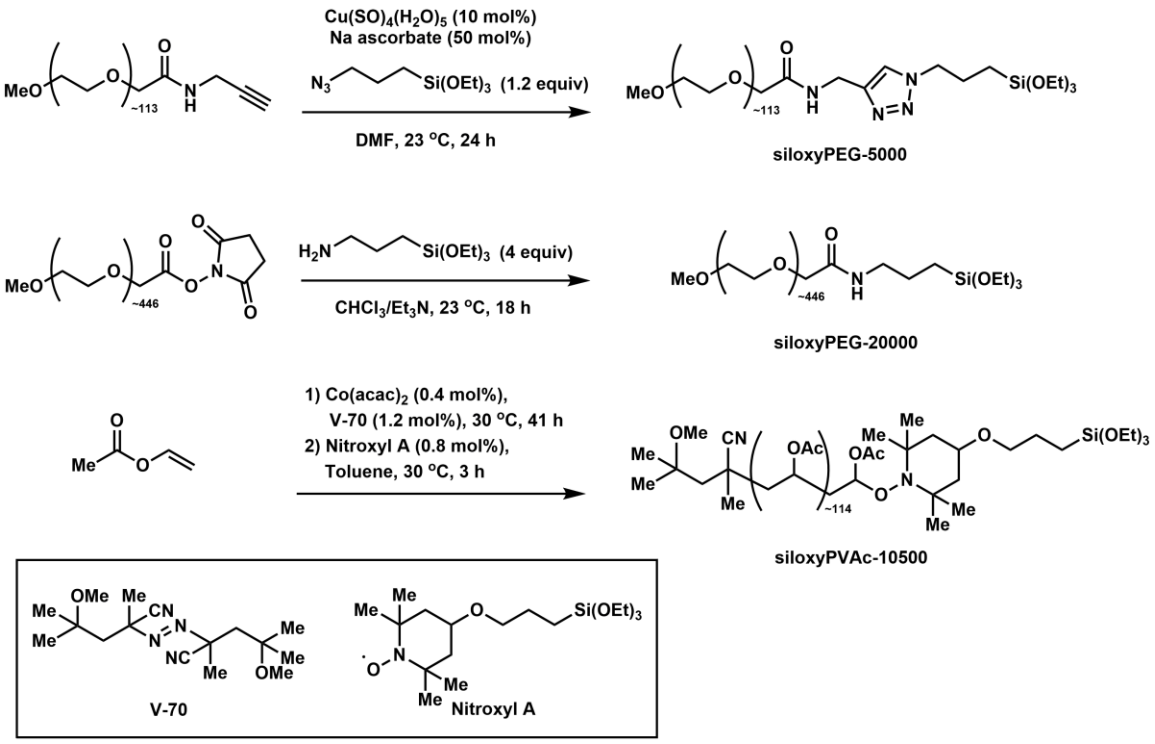

Figure 4.4. Synthetic routes to 3-(triethoxysilyl)propyl-terminated polyethylene glycols and polyvinyl acetate for direct grafting onto glass microtoroids.

In contrast, accessing (3-triethoxysilyl)propyl-terminated polyvinyl acetate (PVAc) required that the polymer be synthesized under living radical conditions, such that the desired end group could be installed in a well-defined manner. Vinyl acetate was successfully polymerized under cobalt-mediated conditions at 30°C using a combination of $Co(acac)_2$ (acac = acetylacetonate) and V-70 (2,2'-azobis(4-methoxy-2,4-dimethylvaleronitrile), a low temperature azo radical initiator). While these living polymerization conditions for vinyl acetate have been widely reported,[102], [103] we implemented a less typical method for installing the desired end group: addition of nitroxyl radical, a TEMPO derivative functionalized with a (3-triethoxysilyl)propyl group, lead to termination of the polymerization and allowed for the desired (3-triethoxysilyl)propyl-terminated PVAc (siloxyPVAc-10500) to be isolated. This nitroxide

termination approach has been previously utilized to yield PVAc macroinitiators for ATRP.[29] Following purification of the polymer, NMR spectroscopy indicated that the desired end group has been installed with high efficiency (>95%). Furthermore, analytical gel permeation chromatography indicated a number average molecular weight (M_n) of approximately 10500 Da with a polydispersity (M_n/M_w) of 1.06. To our knowledge, there are no prior reports of a similar siloxy-terminated PVAc synthetized in a one-pot manner.

Siloxy-terminated polymers were deposited onto freshly prepared silica microtoroids by a solvothermal route. Generally, a 6 mM solution of the selected siloxy-terminated polymer in either chloroform or dimethyl sulfoxide (DMSO) was incubated with the bare microtoroid at room temperature for 2 hours. These conditions consistently yielded polymer-coated toroids with satisfactory optical properties, as characterized by a minimal decrease in quality factor (Q). A PVA-coated microtoroid was made by submerging a PVAc-coated microtoroid in a 3mM 200uL KOH/MeOH solution on a 45˚C hotplate for 1 hour. Following washing and the removal of residual solvent (dry N_2 stream or vacuum oven), the polymer-coated toroids were then evaluated in gas sensing experiments. Further synthesis details as well as nuclear magnetic resonance (NMR) spectra and size exclusion chromatography (SEC) data are provided in the Supplemental Information.

4.2.6 Thermal drift calibration

The refractive index and physical size of the microtoroid are temperature dependent due to thermal expansion. Under laboratory conditions, the wavelength shift can be considered linear with respect to a small range of temperatures and can be expressed as:

$$\Delta\lambda_T = K_T \cdot \Delta T \tag{4.3}$$

Before introducing the test gas, we need to calibrate the subsequent temperature drift by measuring the thermal coefficient, K_T. A thermal sensor (Amphenol SC30F103A) is placed between the chip and gas inlet to monitor the environmental temperature change. However, since it cannot be in contact with the toroid, it only provides an approximate measurement of the actual toroid temperature. For example, it does not capture the initial temperature shift caused by the pump light. The wavelength shift and temperature change with time in the initial stage of the experiment are shown in Figure 4.5, where the relationship is nonlinear.

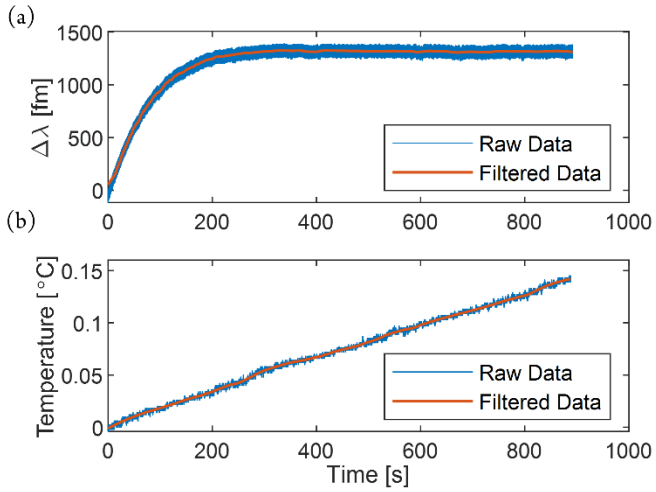

Figure 4.5. Nonlinear thermal drift at the beginning of frequency-locking. (a) Wavelength shift. (b) Temperature change.

After the initial thermal drift reaches a steady state, we then observe a linear relationship between the wavelength shift and the measured temperature change (Figure 4.6). The slope of the fitted line in Figure 4.6 (c) is 3200 pm $°C^{-1}$. The calibrated wavelength shift is flat. At this point, we begin trace gas sensing experiments.

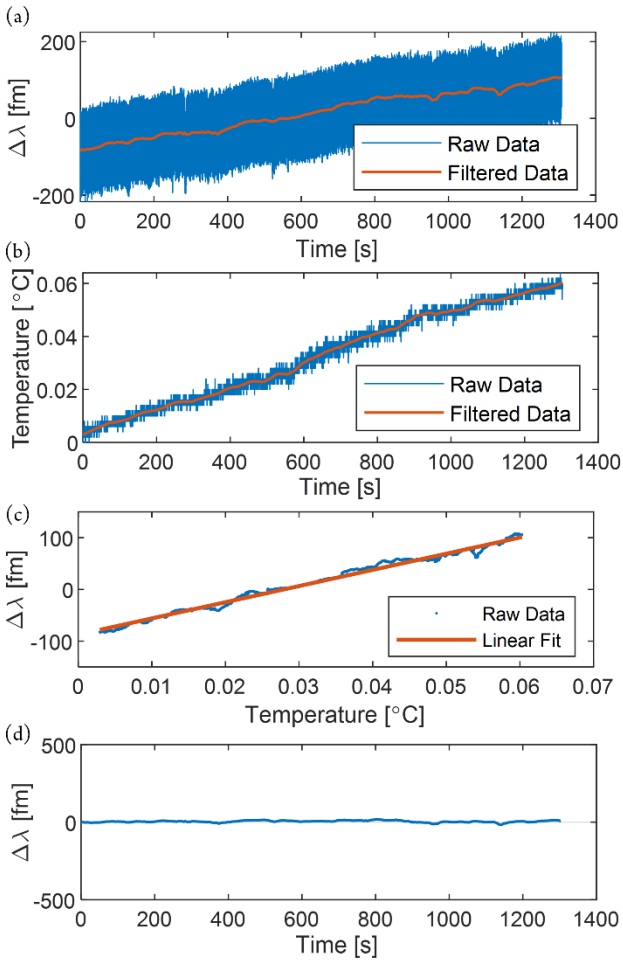

Figure 4.6. Linear thermal drift and sensor stabilization. (a) Wavelength shift after the pump light-induced thermal drift reaches a steady state corresponding to (b) Measured temperature change. (c) Wavelength shift versus temperature change and its linear fit. (d) Calibrated wavelength shift.

4.3 Results and discussion

4.3.1 Sensitivity and selectivity tests of polymer-coated microtoroids

Gas sensing experiments were done in as controlled an environment as possible. The chamber is first initially filled with nitrogen. Air flow into the chamber is controlled by a flowmeter at 50 standard cubic centimeters per minute (sccm). Both wavelength shift and temperature change data are tracked and recorded simultaneously as the chamber fills with nitrogen. The thermal coefficient of the polymer-coated toroid is then determined and was found to be in the range of 2–8 pm/°C.[40], [104] Subsequently, resonance frequency shifts were recorded in response to increases in concentration; all wavelength shift data is calibrated by previously obtained temperature coefficients for each particular microtoroid (see Supplementary Information, Materials & Methods). Switching between the nitrogen carrier and the target gas was performed every ten minutes.

The response of toroids coated with PEG, PVAc, and PVA coatings to DIMP, ammonia, and formaldehyde at different concentrations are shown in Figures 4.7, 4.8, and 4.9 respectively. The gas concentrations range from 0.5 ppb to 4 ppb. PEG-coated toroids show a much stronger reaction to DIMP than ammonia or formaldehyde (Figure 4.7), despite ammonia being readily dissolvable in liquid PEG at sub-atmospheric pressures,[105] and formaldehyde being a significant and persistent impurity in PEG owing to the decomposition of hydroxymethyl end groups in the polymer.[106] In our experiments, we believe the strongly polar phosphorous oxide bond in DIMP is responsible for its strong interactions with PEG as compared to those of ammonia or formaldehyde at the low concentrations employed in our gas sensing experiments. The presence of methoxy end groups, as opposed to hydroxyl end groups, in our PEG coatings suggests that the polymer is not being chemically modified by DIMP during our measurements. Experiments using

a lower molecular weight PEG (5k) resulted in higher limits of detection (Supplementary Information).

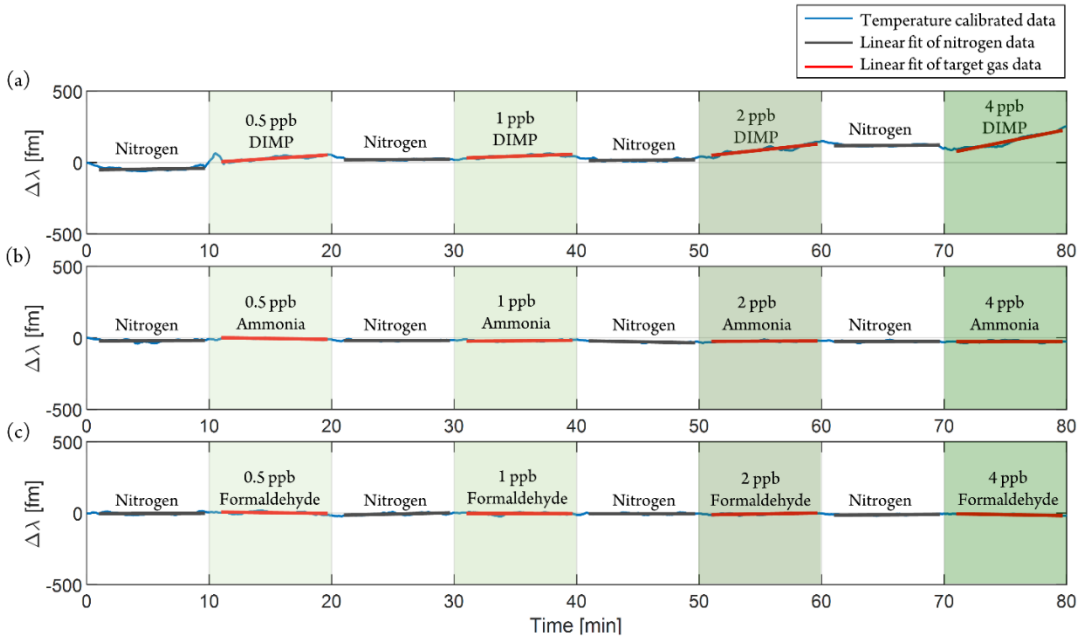

Figure 4.7. Response of a PEG-20k coated microtoroid to (a) DIMP, (b) ammonia, and (c) formaldehyde. PEG-20k-coated toroids show a shift to longer wavelengths in reaction with DIMP, but no discernible reaction to ammonia or formaldehyde.

Figure 4.8 indicates that the PVAc coating, similarly to PEG, has no strong interaction with formaldehyde that can provide a means of gas vapor detection with our WGM sensor. In contrast, PVAc displays strong sensitivity towards ammonia. For DIMP detection, the signal response is difficult to observe at low concentrations and is only apparent as the concentrations gradually increase to 2 ppb and higher, suggesting that the PVAc coating is much less sensitive to DIMP than the PEG coating was. In the detection of DIMP vapors by PVAc, the corresponding effective refractive index slightly decreases, resulting in a blue shift.

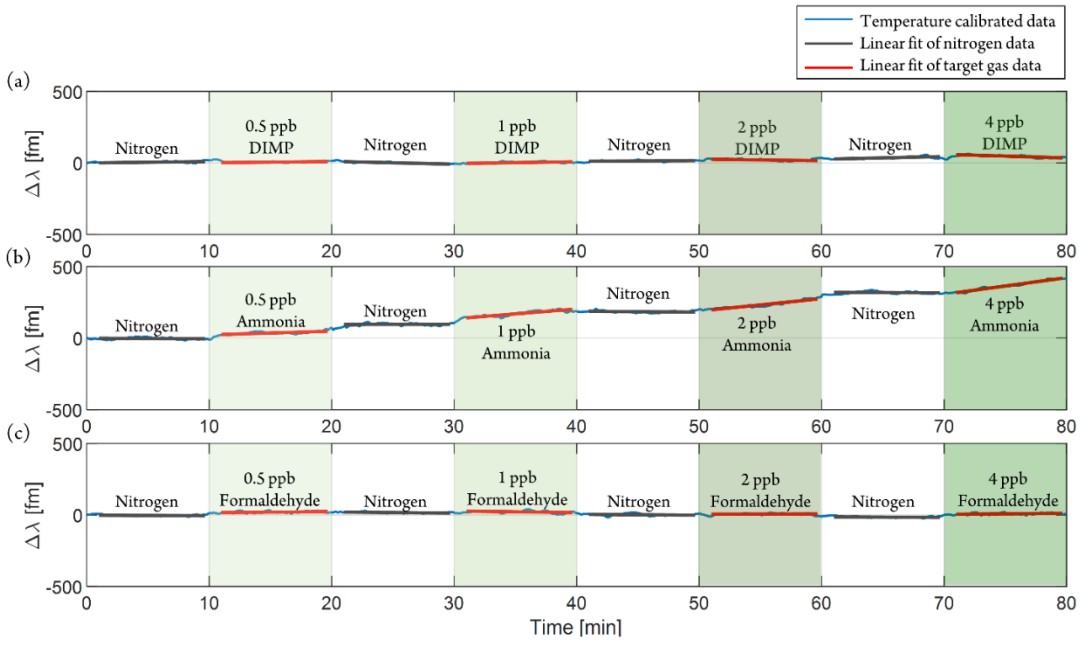

Figure 4.8. Response of a PVAc-10.5k coated microtoroid to (a) DIMP, (b) ammonia, and (c) formaldehyde. The PVAc-10.5k treated toroid shows a weak blue shift (shift to shorter wavelengths) in response to DIMP and a significant red shift in response to ammonia. Similar to PEG, PVAc-10.5k is non-reactive to formaldehyde.

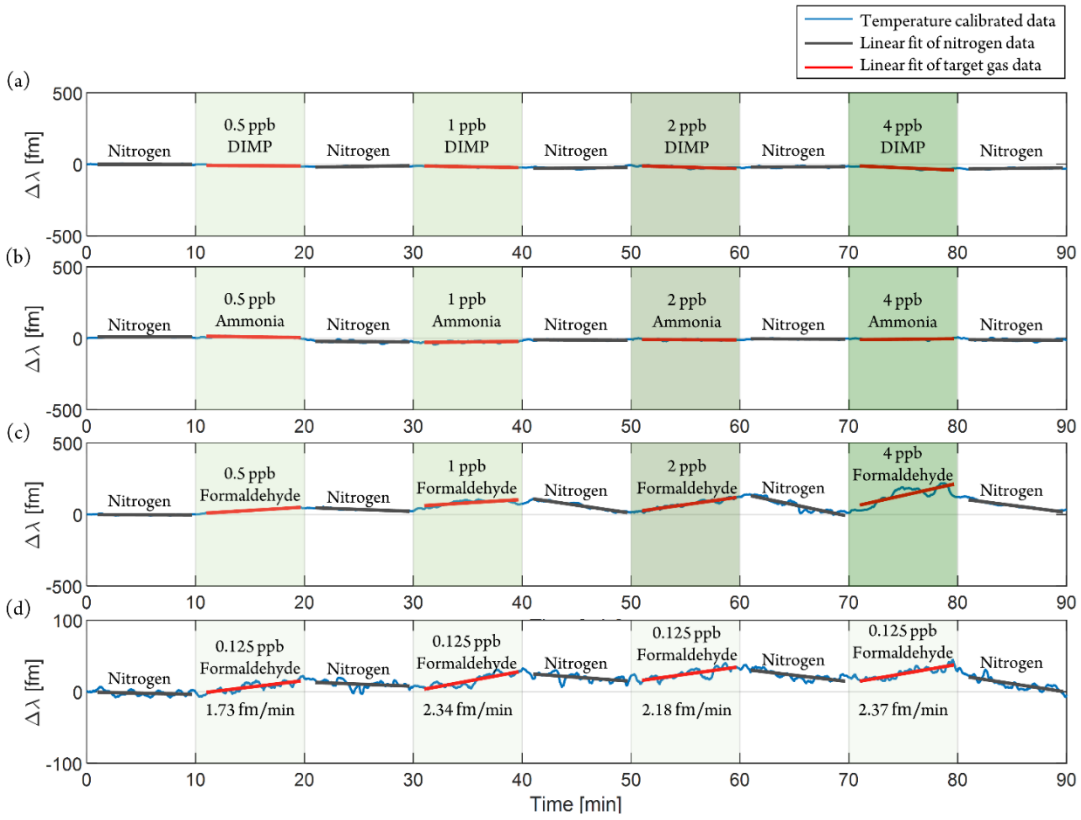

Figure 4.9. Response of a PVA coated microtoroid to (a) DIMP, (b) ammonia, and (c) formaldehyde. The PVA-treated toroid presents a clear red shift (shift to longer wavelengths) in response to low concentrations of formaldehyde and a distinct reversible response after switching back to pure nitrogen. The toroid sensors show a slight blue shift in response to DIMP and no response to ammonia. (d) Reproducibility of the sensor response at 125 ppt of formaldehyde.

The selectivity test of the PVA-treated toroid for the three gases is shown in Figure 4.9. It is apparent that the PVA no longer responds to ammonia after the alkaline hydrolysis of PVAc. PVA also has an extremely weak response to DIMP that results in a small blue shift of the sensor resonance frequency. These results provide some verification that the chemical reaction between ammonia and the acetate ester groups of PVAc underly its high sensitivity and selectivity for this analyte, as the lack of ester groups in PVA is correlated with no response to ammonia by the WGM

sensor. The small response of PVA to DIMP may involve the exchange of isopropoxide bound to phosphorus for a polymer-based alkoxide; however, such alkoxide exchange reactions generally require elevated temperatures or microwave irradiation to proceed rapidly.[107] In contrast, the PVA-coated microtoroid WGM sensor displays extremely high sensitivity towards formaldehyde. After the removal of formaldehyde from the sample chamber, the signal recovered slowly to the initial position. The sensing and recovery experiment at 125 ppt of formaldehyde exposure (Figure 4.9d) shows excellent reversibility and reproducibility. While this analyte concentration is approaching the detection limit of the sensor (117 ppt, see below), it still responds quickly and consistently. These observations align with a reversible chemical process taking place, such as the 1,2-addition of alcohols to formaldehyde.

4.3.2 Figure of merit in FLOWER gas sensing

The sensitivity of the sensor is given in $\mathrm{fm\,min^{-1}\,ppb^{-1}}$. The background noise of the sensor can be calculated from three times the standard deviation (3σ) of the curve in response to nitrogen. The limit of detection (LOD) of FLOWER for different gases can be derived from the ratio of the background noise and sensitivity, written as[36]:

$$\mathrm{LOD\ [ppb]} = \frac{3\sigma_{\mathrm{Noise}}\ [\mathrm{fm \cdot min^{-1}}]}{\mathrm{Sensitivity\ [fm \cdot min^{-1} \cdot ppb^{-1}]}} \qquad (\mathbf{4.4})$$

Figure 4.10(a) illustrates the procedure for calculating the sensitivity, background noise and LOD using the PVA coated toroid as an example. Greater sensitivity means that the absorption of a unit concentration of gas can cause a greater refractive index change or polymer swelling. A sensitivity heatmap of all the polymer-gas interactions tested is shown in Figure 4.10(b). All three

polymer coatings have excellent selectivity. Except for the reversible reaction of PVA with formaldehyde, all the nitrogen response sections are very flat. This enables sub ppb level detection limits (Table 4.1).

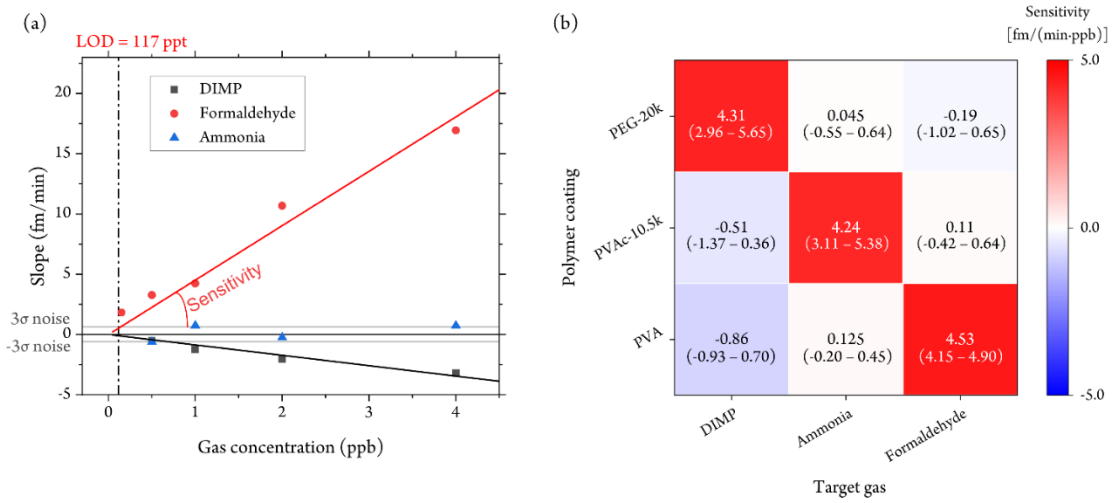

Figure 4.10. Sensitivity, selectivity, and limit of detection. (a) Sensing signal (slope of wavelength shift) of a PVA-coated toroid versus gas concentration. The sensitivity of the PVA-coated toroid to the target gas is obtained by linearly fitting the points in the graph. The interaction of this line with the background noise is the detection limit. The LOD for formaldehyde sensing is 117 ppt. (b) Sensitivity heatmap of different coatings for different gases. The color represents the direction of wavelength shift (red for longer wavelength shifts and blue for shifts to shorter wavelengths). The intensity of the color shade indicates the interaction strength of the two chemicals. The 95% confidence intervals are given in parentheses.

Polymer	Gas	Background noise (3σ) [fm·min^{-1}]	Sensitivity [fm·min^{-1}·ppb^{-1}]	LOD [ppt]
PEG	DIMP	1.308	4.31	304
PVAc	Ammonia	1.842	4.24	434
PVA	Formaldehyde	0.532	4.53	117

Table 4.1. Summary of vapor sensing to DIMP, ammonia, formaldehyde.

4.3.3 Sensitivity/LOD comparison: PEG-5k vs. PEG-20k

PEG-5k and PEG-20k were functionalized on separate toroid surfaces at the same concentration (6 mM) and used for DIMP detection. The 4-fold greater molecular weight makes the Flory radius of PEG-20k about 2.3 times longer than that of PEG-5k [109], which also results in a larger wavelength shift for PEG-20k compared to PEG-5k for the same concentration of DIMP. The slopes of the red and blue fitted lines in Figure 4.11 are 4.31 fm min^{-1} ppb^{-1} and -1.78 fm min^{-1} ppb^{-1}, respectively. The ratio of the two absolute slope values is 2.42, which is very close to the Flory radius ratio of the polymer. The sensitivity of the coating is positively correlated with its thickness. Thicker coatings result in higher sensitivities. We speculate that the blue shift (shift to short wavelengths) in the reaction of PEG-5k with DIMP may be due to the dominant role of the refractive index change compared to polymer layer expansion in the case of ultra-thin polymer layers.

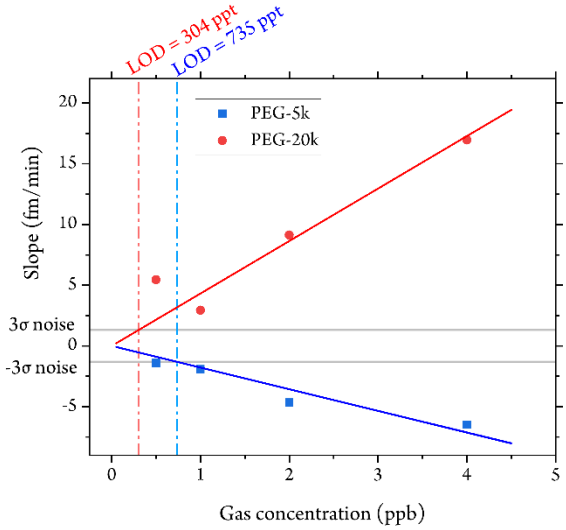

Figure 4.11. Sensing signal (slope of wavelength shift) of a different molecular weight PEG-coated toroids versus DIMP gas concentration.

4.3.4 Irreversible response of PVAc to ammonia

The results in Figure 4.12 (b)(c) show that after the first gas trace test of ammonia from 0.5 ppb to 4 ppb concentrations, the toroid no longer responds to higher concentrations (> 8 ppb), and the response to ammonia after one day is very low. Therefore, we conclude that the detection of ammonia detection via PVAc is irreversible.

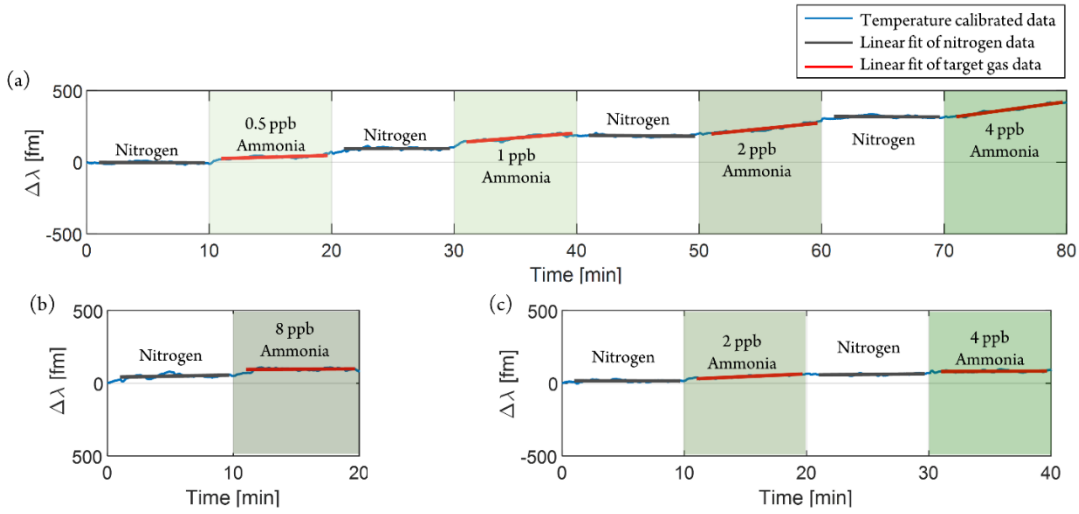

Figure 4.12. Response of a PVAc-10.5k coated microtoroid to ammonia. (b) Test result of ammonia with 8-ppb concentration following the 4-ppb test in (a). Response of the same chip to ammonia after one day of being placed in nitrogen.

4.3.5 Sensitivity and selectivity test of a multilayer coated microtoroid

A mixture of polymers, PEG and PVAc, was used as a single coating on the toroid surface (Figure 4.13). Just as neither PEG nor PVAc was found to facilitate the detection of formaldehyde, the mixed coating of these polymers was also unresponsive to formaldehyde in our gas sensing

tests. The mixed-coating toroid exhibited a noticeable redshift for ammonia, with a sensitivity of 3.83 fm min^{-1} ppb^{-1} that is well within the confidence interval shown in Figure 4.10(b), and also showed a sensitivity of 3.45 fm min^{-1} ppb^{-1} for DIMP, appropriately combining the weak blue-shift effect of DIMP interacting with PVAc with the strong red shift associated with the interaction of DIMP with PEG. Overall, these experimental results are consistent with the sensitivity matrix in Figure 4.10(b). These experiments suggest that FLOWER gas sensors may be modified to impart the sensor with sensitivity for specific analytes in a straightforward, combinatorial manner, overcoming one of the major limitations inherent to many gas sensing technologies.

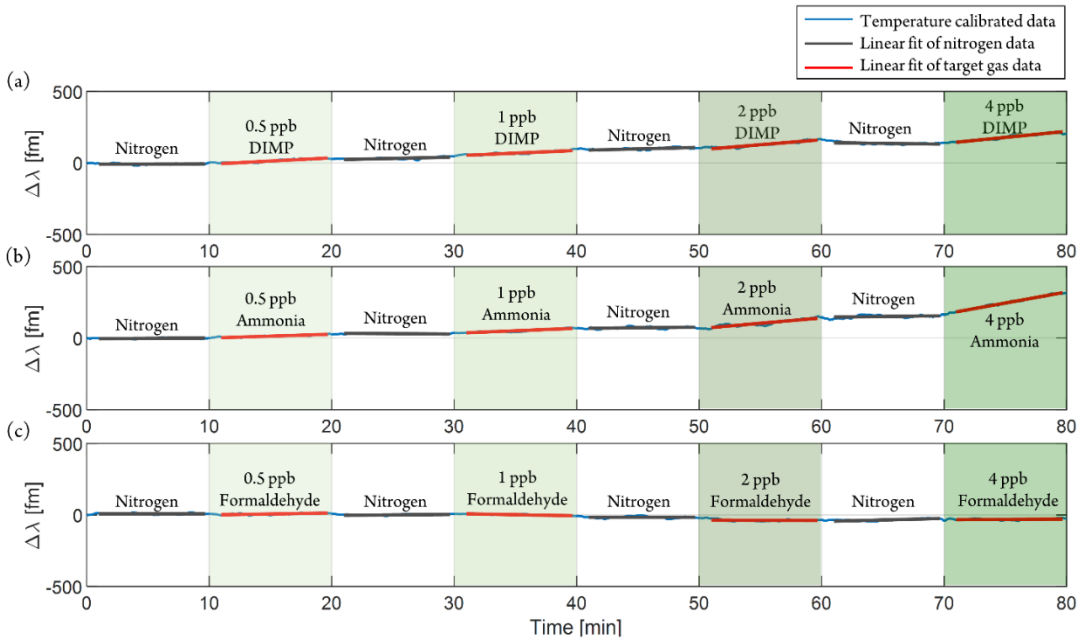

Figure 4.13. PEG and PVAc multilayer coated microtoroid response to (a) DIMP, (b) ammonia, and (c) formaldehyde. This multilayer coated toroid red shifts in response to both DIMP and ammonia but does not significantly respond to formaldehyde. The multilayer toroid's sensitivity to DIMP is slightly lower than to ammonia, which is influenced by the blueshift in response to PVAc and DIMP.

Gas	Sensing technique	LOD	Demonstrated	Reference
DIMP	Present work	304 ppt	500 ppt	
	Paper spray mass spectrometry	A few	A few ppb	[110]
	Organic polymer	6.6 ppb		[111]
Ammonia	Present work	434 ppt	500 ppt	
	Pristine graphene	33.2 ppt	200 ppt	[112]
	Pristine carbon nanotubes (CNTs)	27.8 ppt	200 ppt	[112]
	Silica gel coated microsphere	160 ppt	2.5 ppb	[113]
	SPR with metal oxide	154 ppb	10 ppm	[114]
	Graphene-enhanced Brillouin optomechanical	1 ppb	1 ppm	[115]
Formaldehyde	Present work	117 ppt	125 ppt	
	Carbon nanotubes	20 ppb	20 ppb	[116]
	SnO2-nanowires	2 ppm	2 ppm	[117]

Table 4.2. Comparison with other gas sensing technologies.

Table 4.2 provides a comparison of the WGM gas sensor in this work with other gas sensing technologies for the detection of DIMP, ammonia, and formaldehyde. Using WGM gas sensors, we demonstrate lower detection limits than most gas sensing technologies and selective detection when combined with polymer layers. Graphene and CNTs have lower limits of detection based on extrapolation of sensitivity and noise levels, but similar minimum measured concentrations. Furthermore, these experiments using nanoscale carbon are performed in a vacuum and lack selectivity.

4.4 Conclusion

We combine FLOWER with polymer coatings to create a highly selective as well as sensitive, small molecule gas sensor. We select three harmful gases as the targets for detection, namely DIMP, ammonia, and formaldehyde. By using three different polymer coatings, namely PEG, PVAc, and PVA, we demonstrate sub-ppb detection limits. The selectivity of the three individual coatings has also been verified to correspond to only one of the three analytes. With the

reversible reaction of PVA with formaldehyde, the stability and reproducibility of the sensor at very low concentrations (125 ppt) have also been demonstrated. Furthermore, we realized selective and sensitive sensing by a mixed PEG/PVAc coating that performed in a combinatorial manner in comparison to the individual polymer coatings. This final set of experiments demonstrates the applicability of these devices toward the selective detection of small molecule gas mixtures.

5 TEMPERATURE CALIBRATION OF WHISPERING GALLERY MODE BIOCHEMICAL SENSOR USING OFDR

Whispering gallery mode (WGM) microcavities, such as microspheres, microrings, and microtoroid cavities, have expanded biochemical sensing applications in the last few decades. Analyte particles interacting with the evanescent field of the cavity cause shifts in the WGM resonance. However, light coupled to the cavity through the fiber leads to heating and interferes with the generation of analyte binding curves due to temperature shifts that are difficult to separate from binding generated shifts. Here, we use a high spatial resolution optical frequency-domain reflectometry (OFDR) scheme near 780 nm to calibrate the thermal drift within a microtoroid cavity. Rayleigh backscattering signal enables measurement of temperature with 30 mK resolution. This method will improve detection accuracy as it characterizes the contribution of thermal effects to the measured shift.

5.1 Introduction

Optical whispering gallery mode (WGM) microresonators possess the ability to confine photons for extended durations, thus dramatically enhancing light-matter interactions and enabling different sensing applications.[23]–[25], [29], [118] Mode shift is considered the most widespread sensing technique for WGM. The interaction between the evanescent field and the analyte perturbs the resonance conditions creating a shift in the WGM resonance. By accurately tracking the wavelength shift, the analyte size, concentration, and other characteristics can be analyzed and measured. However, the mode shift sensing mechanism is highly sensitive to environmental conditions. For sensing applications, the wavelength shift induced by circulating light and

surrounding temperature changes, typically known as the thermal effect, can be recognized as thermal noise.[26] Although thermal drift occurs slowly and does not corrupt the detection of single-particle binding events, it can corrupt the measurement of long-term binding profiles. In the experiments, the researchers usually acquire temperature at a few millimeters (mm) from the microresonator and control the temperature of the entire chip. This non-contact temperature acquisition still does not accurately calibrate the temperature variations inside the cavity, such as the heat induced by confined photons, which can be challenging for ultra-low concentration sample detection.

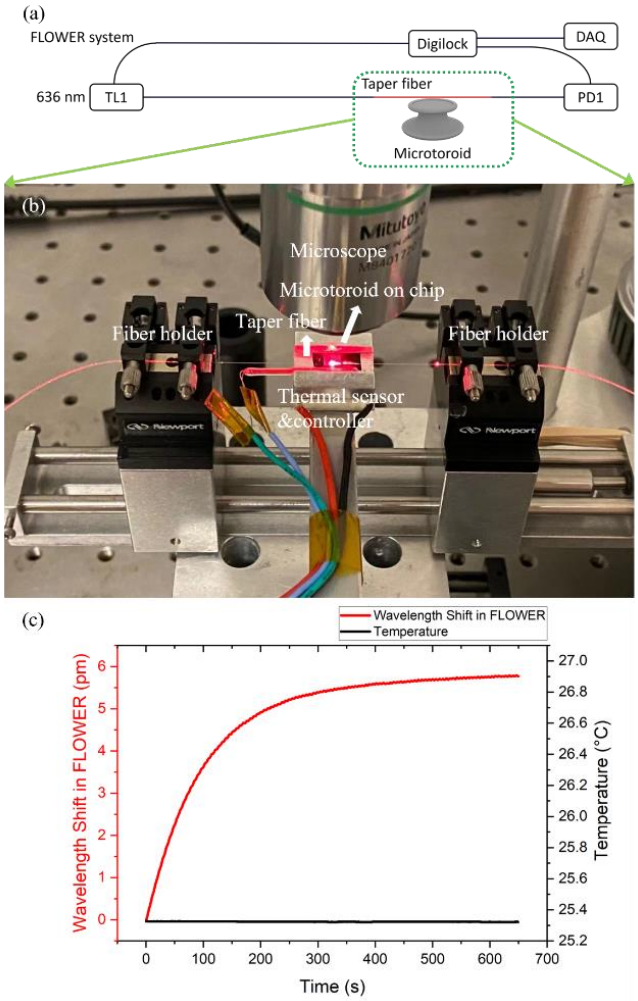

Figure 5.1. (a) Diagram of fiber-based FLOWER system. TL: Tunable laser; PD: Photodetector; DAQ: Data acquisition card. (b) Experimental setup for taper fiber and microtoroid coupling. The microtoroid chip is placed on a stainless steel chamber connected to a high accuracy temperature sensor and controller. (c) The wavelength shift signal and the temperature signal collected by the commercial temperature probe during the initial ten minutes of FLOWER system operation.

The frequency locking technique is an effective method to precisely track the resonance shift of the microresonator.[83] The Digilock device functions as the operator of the electronic feedback system and deliver the high-frequency dither signal that modulates the laser wavelength to the laser controller. The modulated light is coupled to the 100 μm diameter microtoroid on the chip through the evanescent field of the taper fiber. Only the light satisfying the resonance conditions $m\lambda = 2\pi R n_{eff}$ will be confined to the resonator. Digilock then processes the signal received by the photoreceiver to derive the error signal, which is the difference between the wavelength of the tunable laser and the resonance of the microtoroid. A proportional–integral–derivative (PID) controller built in the Digilock regulates the error signal and retransmits it to the laser controller to form the frequency locking. The entire closed-loop electronic control feedback scheme is termed a frequency locked optical whispering evanescent resonator (FLOWER) system (Fig. 5.1(a)), which will enable rapid and high precision tracking of cavity resonance. Q factor (Q), an intrinsic characteristic of the microcavity, serves an essential role in WGM sensing and is defined as $Q = \omega\tau$, where ω and τ are the angular frequency and photon lifetime of the corresponding resonance mode, respectively. Typically, the Q of bare microtoroid is in the range of $10^6 - 10^8$ representing extremely long photon confinement periods. In the early stages of frequency locking, the circulating light continuously heats the microtoroid and leads to refractive

index changes, eventually yielding a wavelength shift of several picometres (pm). As shown in Fig. 5.1(c), the sensing signal for the first ten minutes is approximately equivalent to a temperature change of 1.5 ℃. Such a large temperature change cannot be captured by a temperature sensor placed a few millimeters away. The detected temperature variation does not even exceed 0.1 ℃. Optical fiber, the only optical component in direct contact with the microtoroid in the experiment, would be used as a temperature sensor to monitor and collect the temperature changes inside the toroid.

In this work, we propose a temperature calibration method that exploits the OFDR technique near 780 nm to analyze Rayleigh backscattering signals (RBS) in fibers to calibrate the thermal drift inside the microtoroid. Due to the wide-range sweep of optical frequencies (8 THz) corresponding to the wavelength range (765 – 781 nm), this method can achieve ultra-high spatial resolution at the micrometer (μm) level. In addition, the reflected signal generated by each cycle of the confined light in the resonator is distributed consecutively in the spatial domain overlapping with the single-mode fiber region, which greatly expands the effective sensing area and thus improves the sensitivity of temperature sensing.

5.2 OFDR temperature sensing principle

The basic configuration of the OFDR distributed optical sensing system is mainly a Mach-Zehnder interferometer (MZI).[119] When the light passes through the test fiber, its Rayleigh backscattering return to the circulator coupler and interference with the reference signal to generate beat signals as shown in the blue frame in Fig. 5.2(a) [120]–[122]. By converting the beat

frequency signal in the frequency and time domains, physical information about the scattering point at a specific location can be accessed as shown in Fig. 5.2(b) [123]–[125].

When the single-mode fiber is disturbed by the environment, the wave equation for steady-state propagation can be described as [125]:

$$\frac{\partial^2 E}{\partial z^2} + \beta^2 \left[1 + \frac{\Delta\varepsilon(z)}{\varepsilon}\right] E = 0 \tag{5.1}$$

where β is the wavenumber in the fiber, $\Delta\varepsilon(z)$ is the variation of the permittivity of the fiber core along the propagation direction. The function of $\Delta\bar{\varepsilon}(z)$ in a measured region is given by:

$$\begin{aligned}\Delta\bar{\varepsilon}(z) &= \frac{2}{\pi}\int_{\beta_0-\Delta\beta}^{\beta_0+\Delta\beta} \Delta\tilde{\varepsilon}(\beta)\exp(-i2\beta z)\mathrm{d}\beta \\ &= \frac{2}{\pi}\int_{\beta_0-\Delta\beta}^{\beta_0+\Delta\beta}\int_{-\infty}^{\infty} \Delta\varepsilon(z)\exp(-i2\beta z)\mathrm{d}z \cdot \exp\{i2\beta(z-z_0)\}\mathrm{d}\beta \end{aligned} \tag{5.2}$$

The integral transformation of $\Delta\tilde{\varepsilon}(\omega) = \int_{-\infty}^{\infty} \Delta\varepsilon(z)\exp(-i2\beta z)\mathrm{d}z$ divides the permittivity into separate spatial frequency components. and the integration of $\int_{\beta_0-\Delta\beta}^{\beta_0+\Delta\beta} \Delta\tilde{\varepsilon}(\omega)\exp\{i2\beta(z-z_0)\}\mathrm{d}\beta$ creates a new permittivity function composed of the original permittivity function in the measurement range.

The electric field in a fiber can be written as a sum of two waves propagating forward and backward $E = E_0\exp(j\beta z) + E_r(z,\beta)\exp(-j\beta z)$, where E_0 is the constant amplitude of the forward propagating wave and $E_r(z,\beta)$ is the amplitude of the spatially varying backward propagating wave. Assume the wave varies slowly ($\mathrm{d}^2E_r(z,\beta)/\mathrm{d}z^2 \cong 0$) and the scattered light is weak ($|E_r(z,\beta)| \ll E_0$), $E_r(z,\beta)$ can be solved as follows:

$$E_r(-\infty,\beta) = \frac{E_0\beta}{2i}\int_{-\infty}^{\infty}\frac{\Delta\varepsilon(z)}{\varepsilon}\exp(i2\beta z)dz \tag{5.3}$$

After introducing a reference reflection into the fiber at the location $z = z_0$, we then have a detected E-field:

$$E_d(\beta) = E_0\frac{\beta}{2i}\int_{-\infty}^{\infty}\frac{\Delta\varepsilon(z)}{\varepsilon}\exp(i2\beta z)\mathrm{d}z + rE_0\exp(i2\beta z_0) \tag{5.4}$$

where r is the scatterer reflectivity. Then the signal intensity at the detector is $I_d = \sqrt{\frac{\varepsilon}{\mu}}E_d(\beta)E_d^*(\beta)$. After derivation, the measured intensity in the range of $2\Delta\beta$ centered at β_0 due to laser scanning can be expressed as [125]:

$$\int_{\beta_0-\Delta\beta}^{\beta_0+\Delta\beta} I_d(\beta)\exp\{-i2\beta(z-z_0)\}\mathrm{d}\beta = {E_0}^2 r\frac{c\pi\beta_0}{ni}\Delta\bar{\varepsilon}(z) \tag{5.5}$$

The permittivity variation is thus obtained as [126]:

$$\Delta\bar{\varepsilon}(z) = i\frac{n}{{E_0}^2 rc\beta_0\pi}\int_{\beta_0-\Delta\beta}^{\beta_0+\Delta\beta} I_d(\beta)\exp\{-i2\beta(z-z_0)\}\,d\beta \tag{5.6}$$

That is, the permittivity variation can be solved by integrating the intensity of the reference reflection at different wavenumbers. In other words, we need to Fourier transform the beating signal scanned over a certain wavelength range and then process it at a specific location (using a rect function filtering).

The signal processing of temperature variations is described in Fig. 5.2(c). The temperature-induced relative variations in refractive index (or permittivity variations) require two sets of reflected beat frequency signals. Both the reference and measurement signals are initially recorded in the time domain and, due to laser scanning, can also be treated as a "periodic" optical

frequency domain ($I(\nu)$ or $I(\lambda)$).[125]–[127] The signal is Fourier transformed ($I(\tau) = \mathcal{F}\{I(\nu)\}$ or $\mathcal{F}\{I(\lambda)\}$) and then multiplied by $\frac{c}{2n}$ coefficient to transfer to the spatial domain $I(z)$ with $z = \frac{c}{2n}\tau$. Here $\frac{c}{n}$ is the speed of light in the fiber (n is the refractive index of the fiber). In practice, the signals are collected and processed with discrete sampling. The detected signal intensity as a function of position (discrete Fourier transform of the intensity) can be rewritten as:

$$\tilde{I}(z) = \frac{1}{N}\sum_{k=0}^{N-1} I_k e^{-ikm\frac{2\pi}{N}} \tag{5.7}$$

where *N* is the total number of points in the measurement and I_k is the spectral intensity at different locations. The step size corresponding to the spatial resolution is $L_{RES} = \frac{\pi}{nk_{range}} \approx \frac{\lambda^2}{2n\lambda_{range}} \approx 12.25\mu m$, where $\lambda_{range} = 16\ nm$ is the total wavelength tuning range from 765 nm to 781 nm.

Then the spectra of any segment of the test fiber are converted by selecting the corresponding spatial domain signals and transforming them back to the optical frequency domain, namely the reference/measurement Rayleigh backscattering signal. A sliding window with certain width $\Delta z = N' L_{RES}$ is taken to filter the sensing data in the spatial domain. Zero-padding, an effective interpolation method, is used to improve the distributed temperature measurement accuracy before inverse Fourier Transform (IFT). [128] Finally, the temperature variations are measured by the spectral shifts in the reference RBS from zero-mean normalized cross-correlation (ZNCC) [126]:

$$I_k^{(ref)} \otimes I_{N'-k}^{(test)*} = \frac{1}{2\pi N}\sum_{m=m_1}^{m_2} \tilde{I}_m^{(ref)} \tilde{I}_m^{(test)*} e^{ijm\frac{2\pi}{N'}} \tag{5.8}$$

where N' represents the number of points in the measurement range Δz ($N' = m_2 - m_1 + 1$). When there is no change in temperature, a peak is expected at zero frequency. When a temperature change is applied to the measurement range, this peak is shifted proportionally.

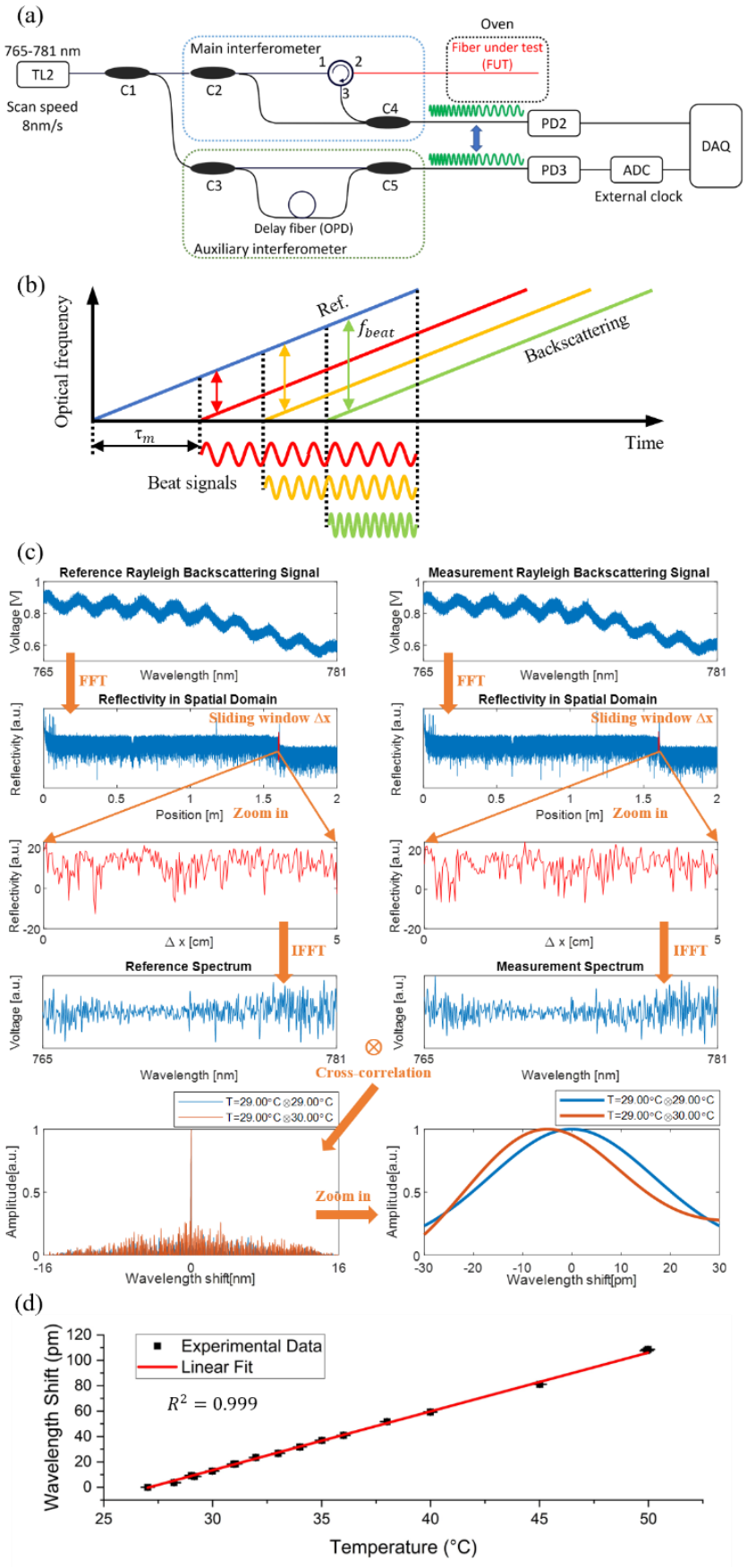
(a)
765-781 nm
TL2
Scan speed
8nm/s
C1
Main interferometer
C2
1
2
3
C4
Oven
Fiber under test
(FUT)
PD2
PD3
ADC
DAQ
External clock
C3
C5
Delay fiber (OPD)
Auxiliary interferometer
(b)
Optical frequency
Ref.
f_{beat}
Backscattering
τ_m
Time
Beat signals
(c)
Reference Rayleigh Backscattering Signal
Measurement Rayleigh Backscattering Signal
Voltage [V]
Wavelength [nm]
FFT
Reflectivity in Spatial Domain
Sliding window Δx
Reflectivity [a.u.]
Position [m]
Zoom in
Δ x [cm]
IFFT
Reference Spectrum
Measurement Spectrum
Voltage [a.u.]
Cross-correlation
T=29.00°C⊗29.00°C
T=29.00°C⊗30.00°C
Amplitude[a.u.]
Zoom in
Wavelength shift[nm]
Wavelength shift[pm]
(d)
Wavelength Shift (pm)
Experimental Data
Linear Fit
$R^2 = 0.999$
Temperature (°C)

Figure 5.2. (a) Schematic of OFDR temperature sensing system of SM600 fiber near 780nm. C: fiber coupler; ADC: analog-to-digital converter circuit. (b) Beating signals generated from the reference light and backscattering light. (c) Signal processing procedure for distributed OFDR-based temperature sensing system. The specific steps are illustrated by the orange arrows and text

The wavelength shift, $\Delta\lambda$, or frequency shift, $\Delta\nu$, of the backscatter pattern due to a temperature change within a small range, ΔT, is identical to the response of a fiber Bragg grating [129]:

$$\frac{\Delta\lambda}{\lambda} = -\frac{\Delta\nu}{\nu} = k_T \Delta T \tag{5.9}$$

where k_T is the thermo-optical coefficient. Similarly, the wavelength shift in the FLOWER system is linear concerning temperature, but with different coefficients.

5.3 Results and discussion

5.3.1 Temperature calibration of bare single-mode fiber

Before applying the OFDR system to the FLOWER system for microtoroid temperature correction, the temperature of the bare single-mode fiber (Thorlabs SM600) is first measured and calibrated. A 20 cm length of optical fiber without a jacket is placed in a sealed high-precision oven. The laser continuously scans between 765 nm and 781 nm at 8nm/s scan speed. Modulation voltage is a triangular wave ranging within 0-10V from DAQ output. Because the laser in practice cannot do a perfect linear scan, an auxiliary interferometer is built to compensate for the nonlinear phase noise of the laser. It has the same configuration as the main interferometer, with a 14 meters delay fiber to generate beat frequency. The output interference signal is converted by an ADC to

trigger the DAQ's external clock. This nonlinear phase compensation process is referred to as the frequency sampling method.[130], [131] In data analysis, a 5 cm window ($\Delta z = N' L_{RES} = 5\ cm$) is set to crop the sensing area corresponding to $N' = 4081$ within the measurement. As the oven temperature is gradually adjusted from 27 ℃ to 50 ℃, the OFDR wavelength shift data presents a perfectly linear response (Fig. 5.2(d)). The slope representing the thermo-optical coefficient is 4.63 $pm/℃$. At each temperature, 10 sets of data are recorded and analyzed with a standard deviation of less than 0.142 pm, which corresponds to an uncertainty of only 0.03 ℃.

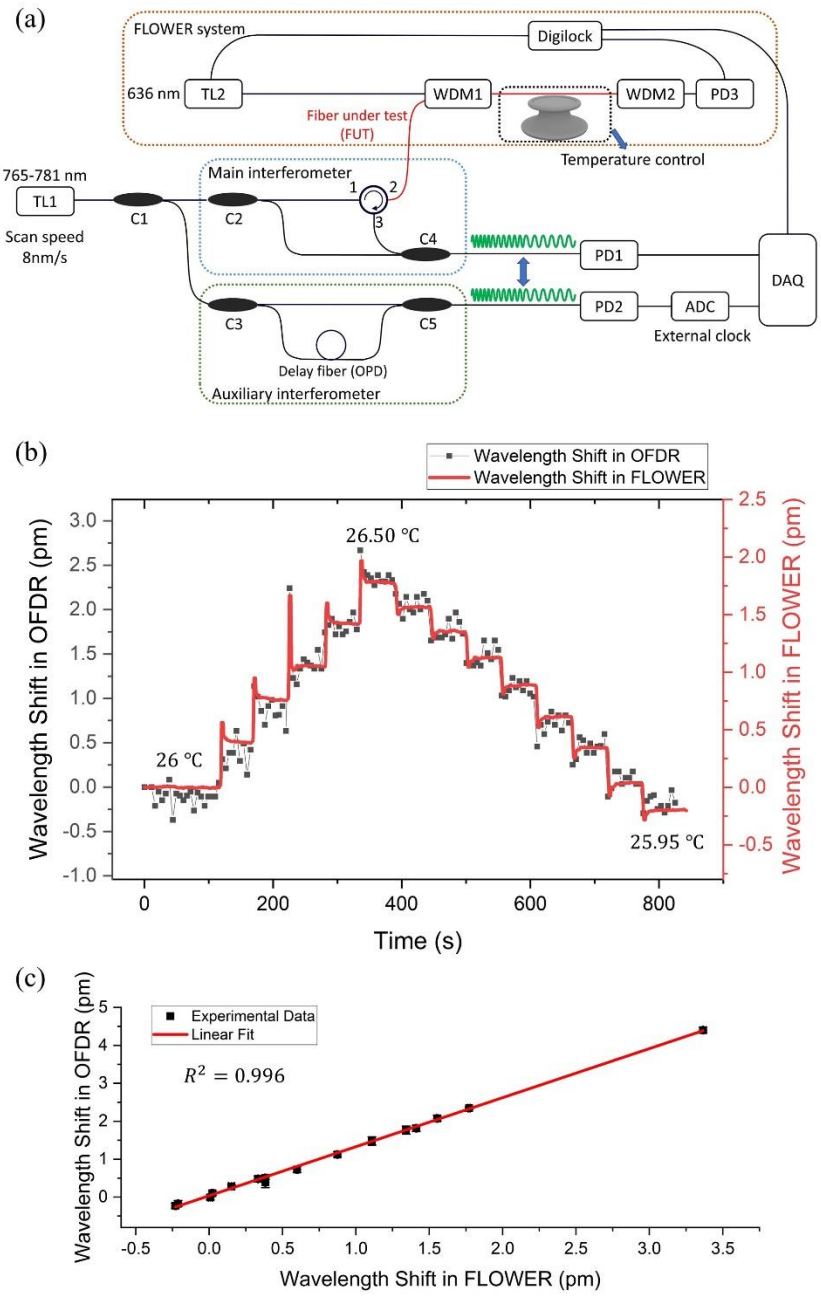

Figure 5.3. (a) Combination of FLOWER system with OFDR. (b) Wavelength shift as a function of time for OFDR and FLOWER systems under external temperature modulation. (c) Wavelength shift in OFDR versus wavelength shift in FLOWER.

5.3.2 Temperature calibration of thermal drift in FLOWER

Afterward, the OFDR is combined with the FLOWER system. The light from port 2 of the circulator is passed through the wavelength-division multiplexing (WDM) and then coupled to the toroid. FLOWER system is operating at 636nm. Two systems do not affect each other. The fiber used for backscattering acquisition is highlighted in red in Fig. 5.3(a). The stainless steel chamber under the toroid is wired to a precision temperature controller (Vescent Photonics SLICE-QTC) with sub-millikelvin stability to mimic environmental temperature changes. OFDR and FLOWER systems are able to track temperature changes simultaneously (Fig. 5.3(b)). Spikes in signal variations are due to proportional–integral–derivative (PID) tuning of the temperature device. After temperature stabilization, the wavelength shifts of the two systems have a good linear relationship with $R^2 = 0.996$ as indicated in Fig. 5.3(c). The slope of linear fit indicates the wavelength shift of the two systems in the ratio $\frac{\Delta\lambda_{OFDR}}{\Delta\lambda_{FLOWER}} = 1.2925$, corresponding to a thermal coefficient k_{T_WGM} of 3.58 $pm/℃$ within theoretical expectations for the WGM mode.

After the dual systems temperature-wavelength calibration, the temperature controller is turned off and the toroid is completely cooled down. The OFDR is still aligned with the FLOWER system. The double y-axis coordinates in Fig. 5.4(a) and (c) are adjusted by the scale factor of the wavelength shift of the two systems. As seen in Fig. 5.4(a), there is a 5.5-second interval between every two OFDR temperature acquisition points, which includes 4 seconds for the tunable laser to complete a full scan (765 – 781 – 765 nm) and 1.5 seconds for the laser re-setting and initialization time. The exponential fit of OFDR sensing data almost overlaps with the wavelength shift of the FLOWER system. The FLOWER wavelength shift corrected by OFDR achieves a very stable condition in only 100 seconds (Fig. 5.4(b)).

Referring back to the thermal drift noise at the beginning of the FLOWER operation, the commercial temperature probe cannot monitor the temperature change inside the toroid. OFDR, however, can have a trend closely following that of the FLOWER system. Its fitted curve nearly coincides with the wavelength shift of FLOWER (Fig. 5.4(c)). After 300 seconds, the corrected wavelength shifts considerably smooth, with a relative temperature change of less than 0.1 ℃ accordingly. Previously, researchers had to wait half an hour or more for thermal equilibrium to begin the sensing experiments. Instead, they can now start in less than 10 minutes, or even 5 minutes.

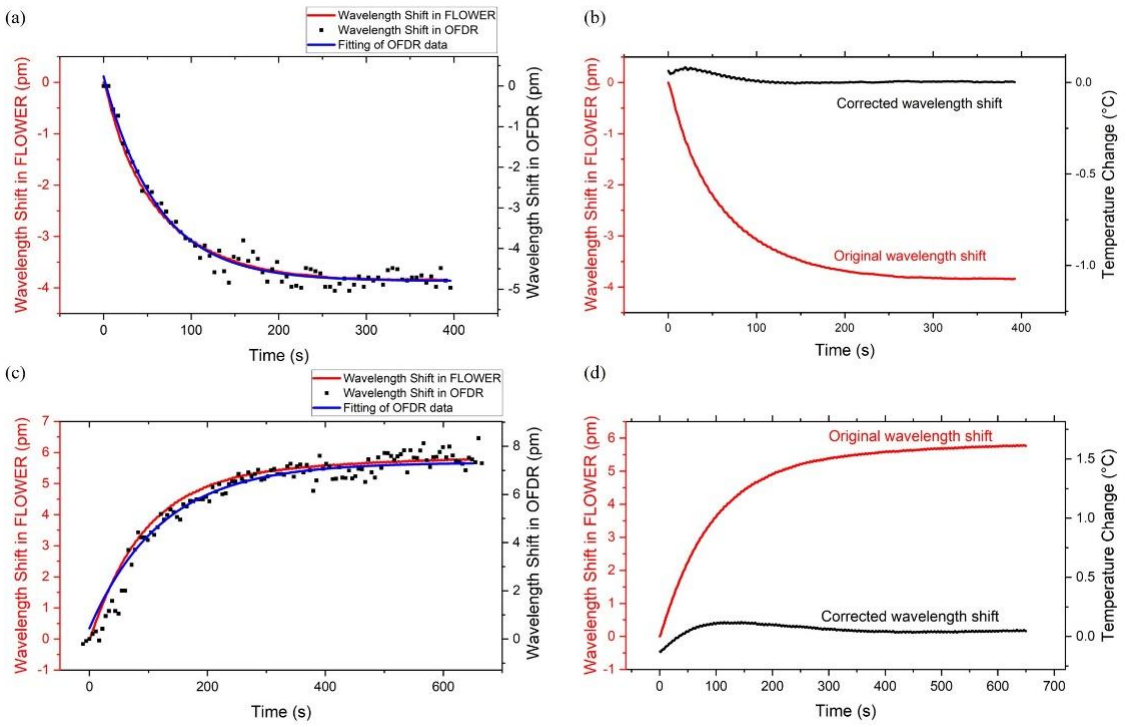

Figure 5.4. Wavelength shifts of the two systems during cooling (a) and heating (c) of the toroid cavity itself. (b) (d) Wavelength shift in FLOWER before and after OFDR calibration.

5.4 Conclusion

In summary, in this work, a high spatial resolution OFDR scheme at 780 nm to calibrate the thermal drift within a microtoroid cavity has been designed and demonstrated. With the help of MZI and hardware frequency sampling method, high spatial resolution signal acquisition in SM600 fiber is realized. By the analysis approaches of zero-padding and ZNCC, the Rayleigh backscattering signal enables the measurement of temperature with 30 mK resolution. Both the thermal drift of the FLOWER system caused by circulating light and ambient temperature changes can be accurately calibrated with OFDR, which greatly minimizes the thermal drift during biochemical sensing experiments. With the development of fabrication technology, smaller size and higher accuracy OFDR systems will be applicable to the measurement and calibration of physical quantities in more photonics integrated devices.

6 PARTICLE SHAPE ANALYSIS USING WHISPERING GALLERY MODE POLARIZATION SENSING

Whispering-gallery mode (WGM) microresonators such as microspheres, microrings, microbubbles, and microtoroids have been used for highly sensitive biological and chemical sensing. Microtoroids due to their extremely high-quality factors can easily sense particles that enter their evanescent field. With the help of auto-balanced detection and data processing techniques, the frequency-locked optical whispering evanescent resonator (FLOWER) approach has successfully reduced external noise and achieved macromolecular detection. FLOWER, however, can only detect and quantify the size of particles. It would be advantageous to also measure the orientation of elongated particles. We can achieve this by tracking how the WGM resonances for different polarizations shift upon interaction with gold nanorods. Using perturbation theory and three-dimensional finite element simulations of nanorods of aspect ratio 2.7 interacting with a microtoroid with resonance, we found significant differences between the frequency shifts of the two polarizations depending on nanorod orientation. A vertical nanorod produces a wavelength shift of -40 fm in the TE mode at 780 nm and -3 fm in the TM mode at 633 nm. In contrast, a spherical particle produces TE and TM shifts of -179 fm at 633 nm and -230 fm at 780 nm, respectively. We further built an experimental dual-FLOWER system to verify our simulation data. Our approach helps to determine the shape and orientation of bound objects thus allowing us to examine, for example, the conformational changes of proteins.

6.1 Introduction

In most previous experiments, researchers have approximated the detected biological particles as spheres for calculation and analysis. However, in real biological cases, many samples cannot be approximated in this way, such as rod-shaped bacterial molecules and Y-shaped antibodies or more complex protein folding structures. Here we want to measure and analyze the shape of the non-spherical particles by using the FLOWER system to resolve the different axial polarizability of the particles.

From the detailed explanation of perturbation theory in Chapter 3, we know that the frequency shift induced by single particle binding can be written as:

$$\frac{\Delta\omega}{\omega} \approx -\frac{\varepsilon_b \boldsymbol{E}_0^{\dagger} \overleftrightarrow{\alpha}(\omega)\, \boldsymbol{E}_0}{2\varepsilon_0 \varepsilon_r V_m \left|\boldsymbol{E}_0\right|^2_{max}} \propto \overleftrightarrow{\alpha}(\omega) = \begin{pmatrix} \alpha_x & 0 & 0 \\ 0 & \alpha_y & 0 \\ 0 & 0 & \alpha_z \end{pmatrix} \tag{6.1}$$

and

$$\alpha_{x,y,z} = \Delta V \varepsilon_0 \frac{\varepsilon_m - \varepsilon_b}{G_{x,y,z}\varepsilon_m + \left(1 - G_{x,y,z}\right)\varepsilon_b}, \tag{6.2}$$

The shift is only proportional to the polarizability of the particle for the induced dipole moment. The polarizabilities are varied on different axes. That is, the wavelength shifts caused by the interaction of electrons in different axes with the WGM evanescent field are different.

In Fig. 6.1, we take the metallic rod as an example, when its long axis is oriented parallel to the TE mode polarization, the free electrons in it are oscillating along with the TE mode, which is well known as the longitudinal mode. Accordingly, the transverse mode is formed in the TM mode polarization direction. Definitely, the longitudinal mode and the transverse mode will cause

the different wavelength shifts of the system, so the size and the shape of this rod could be obtained and measured on a nano-scale.

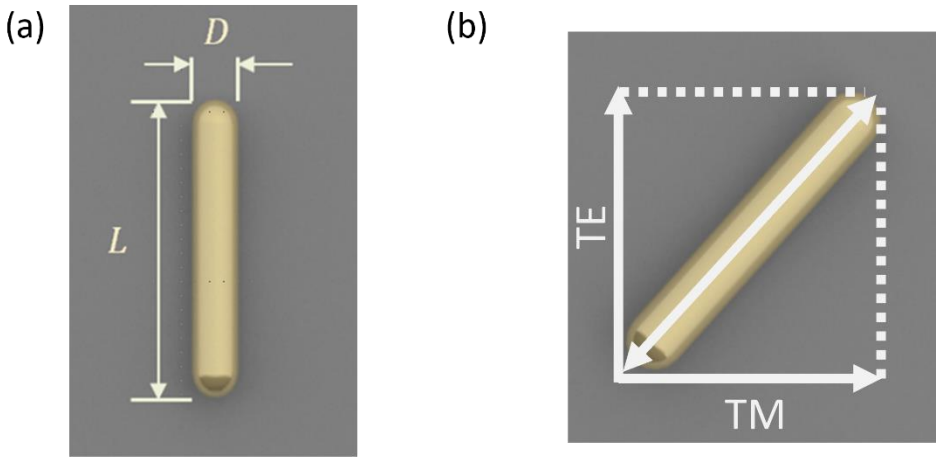

Figure 6.1. (a) A rendering of the gold nanorod. (b) Interaction of a tilted nanorod with fundamental TE and TM modes.

When the particle is rotated at a certain angle attached to the microresonator surface, the projection of its polarizability in different axes can be resolved by the TE and TM mode shifts. Thus, the tilted angle will also be derived. In general, we are developing a 1-D sizing system into a 2-D coordinate sizing system.

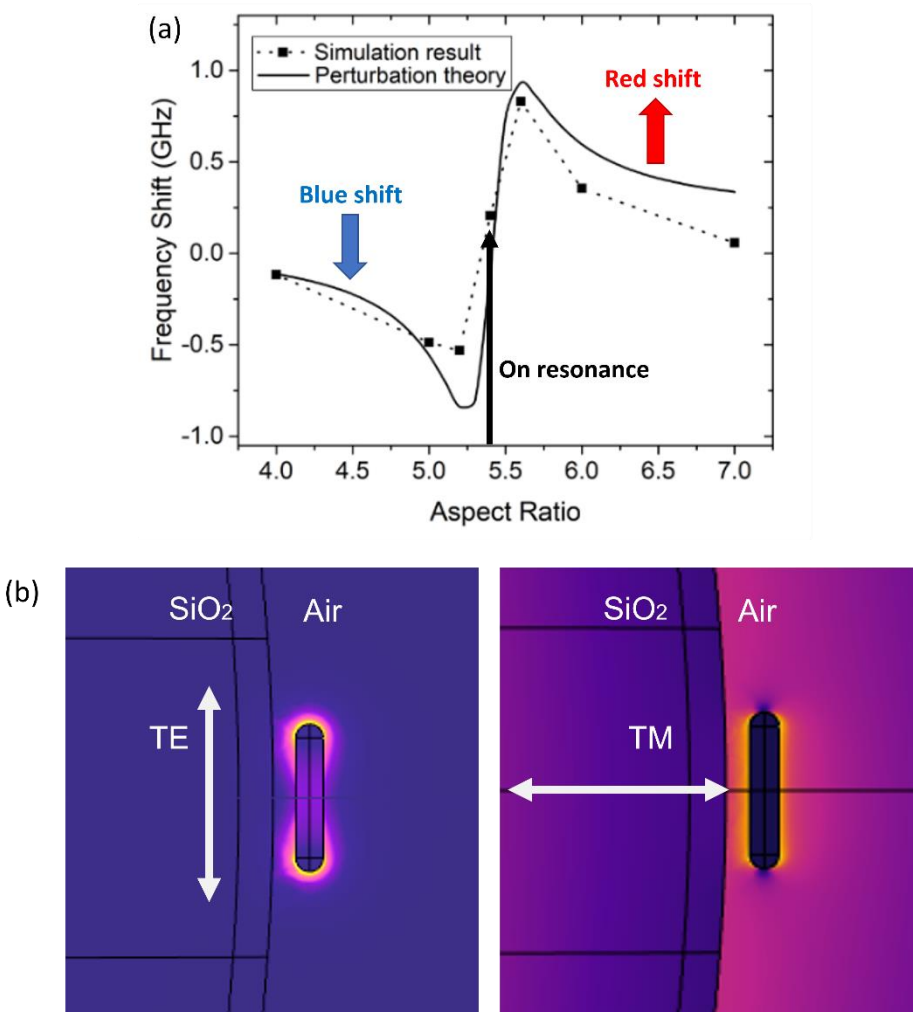

Figure 6.2. (a) Frequency shift induced by a gold nanorod coupling as a function of its aspect ratio. (b) Longitudinal and transverse modes of the gold nanorod interacting with the TE and TM modes.

Due to the material properties of the plasmonic structure, very different responses occur when it has on resonance or off resonance coupling with WGM. If the resonance of the nanorod is to the left of the resonance of the toroid, it will cause the blue shift while it is binding to the surface (Fig. 6.2). Otherwise, it will result in a redshift. This can be a good indicator of particle adsorption or dissociation.

6.2 Experimental setup

Since the frequency-locked technique requires a separate set of signal modulation systems to control the laser, two FLOWER systems are required when tracking two modes with different polarizations simultaneously, namely a dual-FLOWER system as shown in Fig. 6.3. Meanwhile, to avoid crosstalk between the signals, the two FLOWER systems will operate at different wavelengths, one at 780 nm and the other at 636 nm. Both wavelengths can be propagated in Thorlabs SM600 fiber.[132] Two light beams of different wavelengths are combined into a fiber via WDM and coupled to a toroid and then split by WDM to be received by two separate detectors. It is important to note that both ends of the taper fiber need to be fused to the WDM to achieve optimal coupling efficiency and to further avoid signal crosstalk.

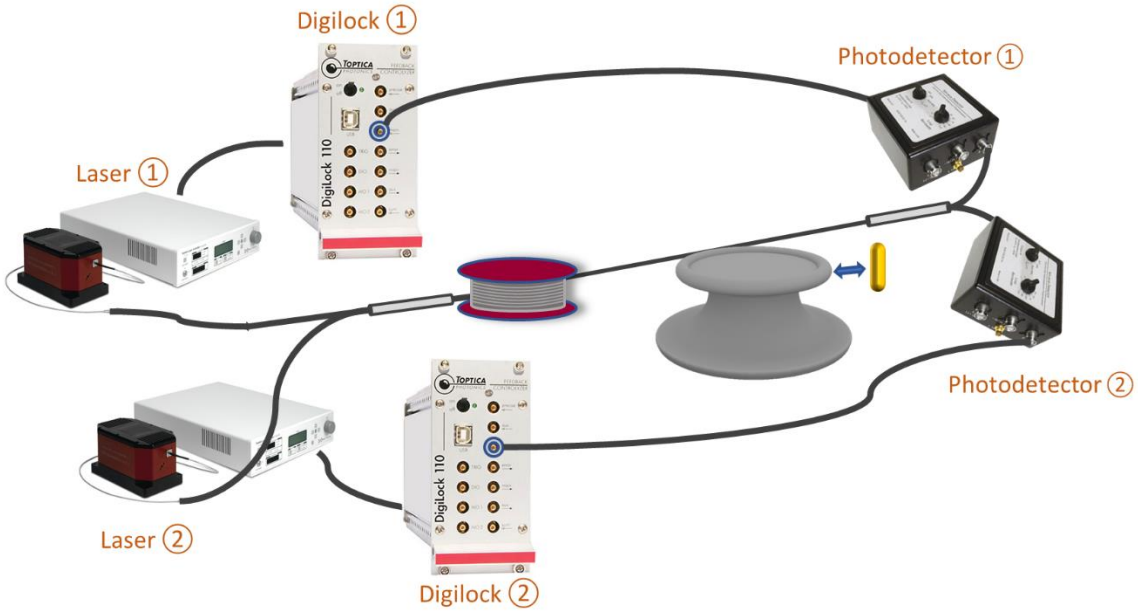

Figure 6.3. Schematic of dual-FLOWER system. Two light from different tunable lasers combined by the wavelength division multiplexer (WDM) are evanescently coupled into the microcavity through the taper fiber and then split into two detectors. After receiving the optical

signal, the two digilock devices modulate the laser outputs to implement frequency locking for both fundamental TE and TM mode, which causes the wavelength of laser output to track the resonance of the microcavity. The wavelength shift caused by the interactions of the attached nanoparticles and different modes can be obtained simultaneously. Accordingly, the size of the corresponding particle along the mode polarization direction can also be calculated by post-processing the feedback signal.

6.3 Results and discussion

FLOWER system output spectrum and its corresponding modes are present in Fig. 6.4. Usually, the sharpest resonance obtained under critical coupling is the fundamental TE mode, and the second sharpest adjacent dip corresponds to TM mode. The spacing between the two modes is about tens of picometers depending on the toroid size. From the simulation E-profile of the cross-section of the toroid, we can see they all have the same pattern. And their mode volume and evanescent amplitude will be taken into account for wavelength shift calculation.

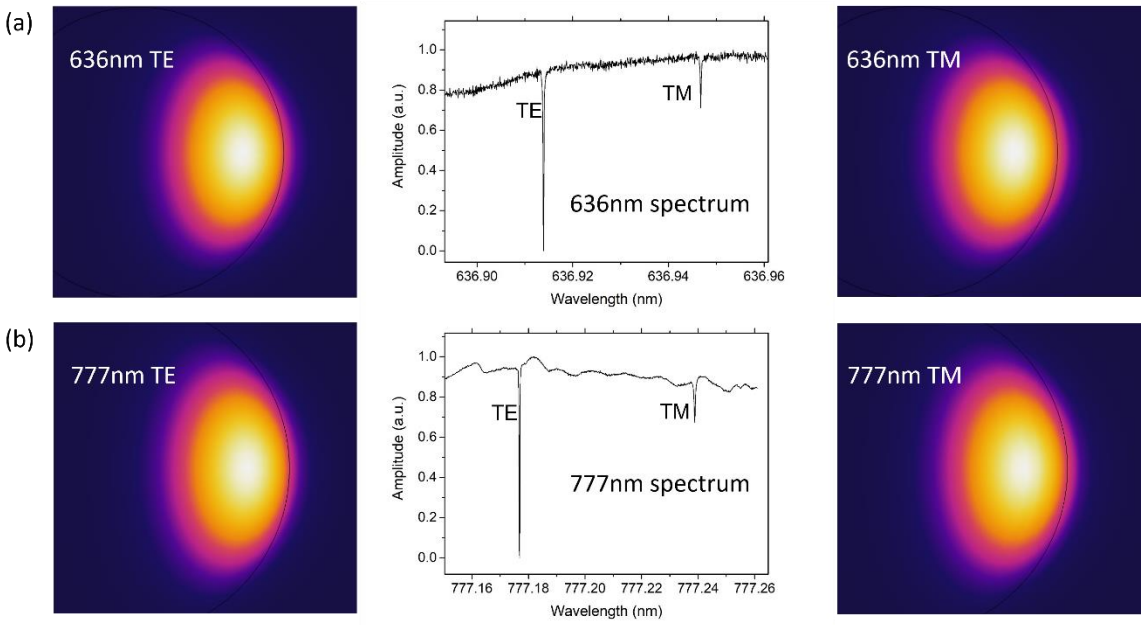

Figure 6.4. FLOWER system output spectrum at (a) 636 nm and (b) 777nm. The corresponding mode distribution is shown on the left and right sides respectively

The shape of two types of particles, gold spheres and gold nanorods (nanoComposix Inc), were measured. In this case, the diameter of the gold sphere measured by transmission electron microscopy (TEM) is $100 \pm 5nm$. Size distribution (CV) is less than 15%, where CV represents the coefficient of variation, also known as relative standard deviation (RSD). The peak resonance of the nanosphere is at 560 nm, which will cause a blue shift for both 636 and 780nm laser, but in different steps. Since the mode pattern of TE and TM are almost the same, their evanescent field intensity is also essentially the same. Theoretically, the wavelength shifts induced by a single gold nanosphere at 636 nm and 777 nm are -179 fm and -230 fm, respectively.

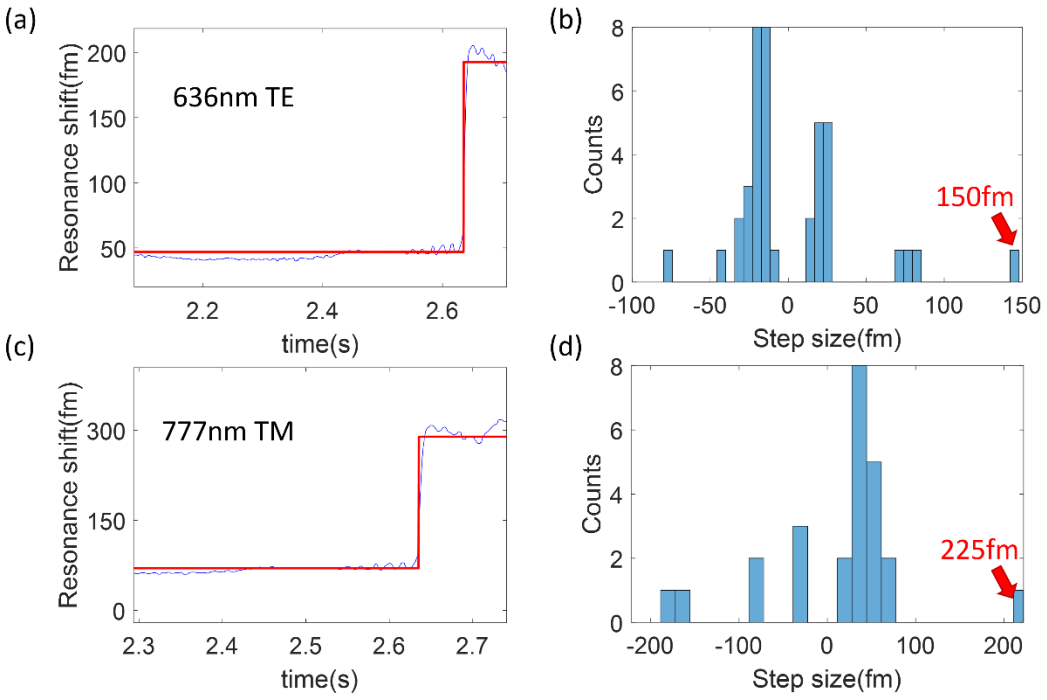

Figure 6.5. Wavelength shift as a function of time for gold nanospheres binding events in (a) TE mode at 636 nm and (c) TM mode at 777 nm. (b) and (d) are the histograms of the steps corresponding to (a) and (c)

As shown in Fig. 6.5, at 2.63s, the signal goes up corresponding to the redshift means the particle is binding off the toroid. From the histogram of the steps, the biggest steps are 150fm for 633nm and 225fm for 780nm. In turn, the dimensions for different axis are calculated as 95nm by 99nm, which is within the size distribution. Thus, the measurements of the binding event at 2.63s are consistent with the nanorod shape. The remaining wavelength shifts in the histogram refer to particles interacting with the toroid's different latitudinal evanescent tails.

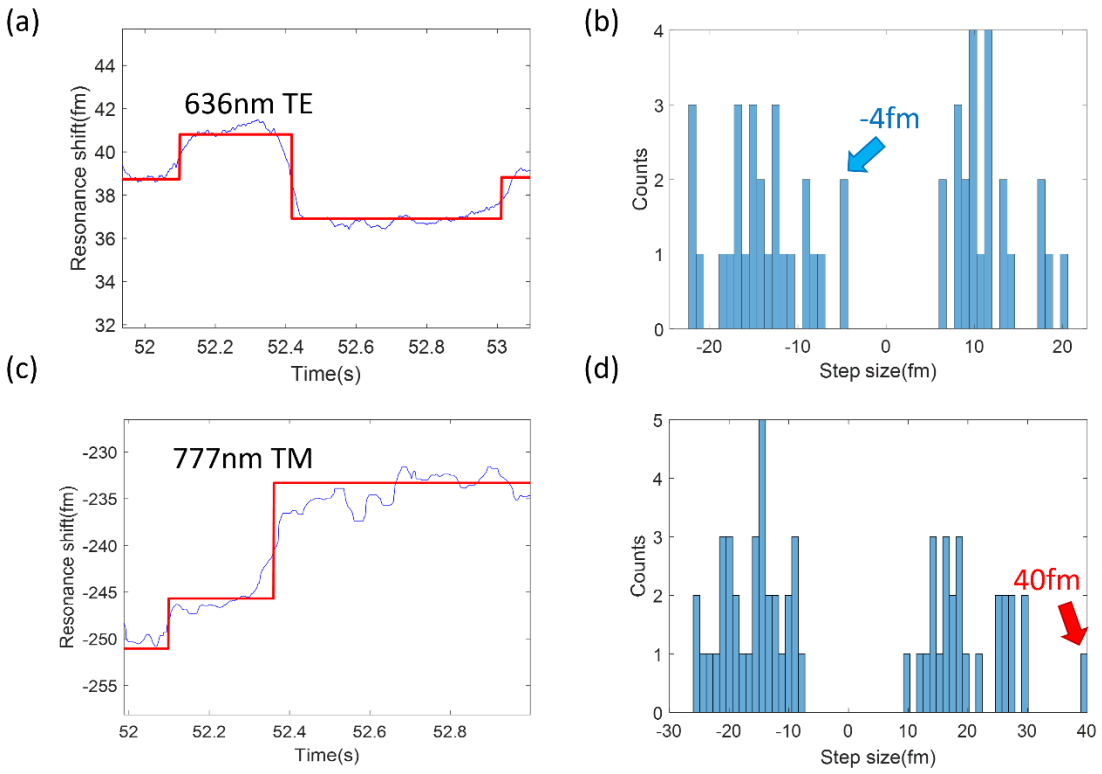

Figure 6.6. Wavelength shift as a function of time for AuNRs binding events in (a) TE mode at 636 nm and (c) TM mode at 777 nm. (b) and (d) are the histograms of the steps corresponding to (a) and (c)

The analysis of gold nanorods is more complex. The average length and width measured by TEM are $50.7 \pm 5.3nm$ and $18.9 \pm 1.2nm$ with a size distribution of 10.4% and 6.4%. Thus, the aspect ratio of about 2.7 and a longitudinal resonance at 673 nm which is between 636 and 777 nm would cause a 28 ± 10 fm redshift of 636 nm WGM and a -40 ± 15 fm blueshift of 777 nm WGM. And the transverse mode is around 550 nm, which will cause a -4 fm blue shift for both longer wavelengths. From the wavelength shift profile in Fig. 6.6, the signal is rising at 636 nm, but falling at 777 nm, as we expected. Then from the histogram for more binding events, the

biggest steps match with the numerical prediction. The shape of the corresponding AuNR is configured as 50nm by 19nm.

The dual-FLOWER system has been shown to effectively reconfigure the shape of rod-shaped plasmonic particles and can be further applied to the detection of irregular biomolecular samples. It should be noted that due to the material properties of biomolecules, their polarizability will be much smaller than that of plasmonic particles of the same size, and consequently, the wavelength shift caused will be small. Therefore, it is necessary for the FLOWER system to have a high enough sensitivity while ensuring that both systems run at the same clock to align the particle binding events.

6.4 Conclusion

We built a dual-FLOWER (frequency locked optical whispering evanescent resonator) system to achieve shape measurements and analysis of gold nanoparticles. The system simultaneously tracks two whispering gallery modes with different polarizations to derive the dimension for the corresponding axis. We will further demonstrate this method on a bioparticle on the nano-scale.

7 SUMMARY AND PROSPECT

After introducing the principles related to the WGM microresonator, this dissertation encompasses two applications (highly sensitive and selective gas sensing and particle shape measurement) and two approaches to improve the sensing performance. Two improvements include a simulation project based on the FEM method and an experimental project based on the fiber optic metrology technique. Both improve the signal-to-noise ratio (SNR) of the WGM gas sensor by enhancing the sensing signal and reducing the noise level, respectively. The gas sensing experiment and the simulation of plasmonic near-field enhancement are both sourced from different subtasks of the same project. The idea of particle shape measurement came from the theoretical derivation of the simulation project.

From the perspective of practicality, the author believes that the sensing performance of current WGM sensors has reached a comparatively high level, and accordingly problems of integration and stability should be addressed. For example, how to efficiently and stably couple light in and out of the WGM cavities, nowadays researchers mainly use taper fibers and prisms as couplers, while waveguides and gratings will certainly take their places as more stable optical components, accordingly, the production and fabrication of these components around the WGM cavities is a big problem. Also from a standpoint of fabrication, what would be a better way to detect a gas mixture, a toroid with a multilayer coating, a toroid sensing array of different specific polymer materials, or both? After solving the problem of optical coupling using a waveguide, the next big problem is the integration of the sensing system, that is, the laser, waveguide, coupler, detector, circuit feedback control system, etc., are all miniaturized or even integrated into the same chip. Only in this way will WGM sensors have the potential for commercialization and portable applications.

The fiber metrology technology called OFDR, mentioned in Chapter 5, has recently been used in automated driving technology, where it is known as FMCW Lidar (frequency-modulated continuous wave) in free space, mainly for measuring the distance and relative speed of people or vehicles in the driving path of a car. Its practical use is primarily due to the solution of manufacturing problems. The OFDR technology mentioned in Chapter 5 can further measure other physical parameters such as temperature while obtaining high precision position information, and the next improvement should also come from the perspective of miniaturization and instrumentalization.

The author firmly believes that when there is a breakthrough in fabrication technology, WGM resonators will become one of the most important components of next-generation photonic integrated devices and are not limited to sensing applications.

REFERENCES

[1] "St Paul's Cathedral," *Wikipedia*. Apr. 02, 2022. Accessed: Apr. 07, 2022. [Online]. Available: https://en.wikipedia.org/w/index.php?title=St_Paul%27s_Cathedral&oldid=1080617231

[2] "Whispering gallery," *Wikipedia*. Dec. 13, 2021. Accessed: Apr. 07, 2022. [Online]. Available: https://en.wikipedia.org/w/index.php?title=Whispering_gallery&oldid=1060059954

[3] Lord Rayleigh, "CXII. *The problem of the whispering gallery*," *The London, Edinburgh, and Dublin Philosophical Magazine and Journal of Science*, vol. 20, no. 120, pp. 1001–1004, Dec. 1910, doi: 10.1080/14786441008636993.

[4] A. Ashkin and J. M. Dziedzic, "Observation of Resonances in the Radiation Pressure on Dielectric Spheres," *Phys. Rev. Lett.*, vol. 38, no. 23, pp. 1351–1354, Jun. 1977, doi: 10.1103/PhysRevLett.38.1351.

[5] R. E. Benner, P. W. Barber, J. F. Owen, and R. K. Chang, "Observation of Structure Resonances in the Fluorescence Spectra from Microspheres," *Phys. Rev. Lett.*, vol. 44, no. 7, pp. 475–478, Feb. 1980, doi: 10.1103/PhysRevLett.44.475.

[6] V. B. Braginsky, M. L. Gorodetsky, and V. S. Ilchenko, "Quality-factor and nonlinear properties of optical whispering-gallery modes," *Physics Letters A*, vol. 137, no. 7, pp. 393–397, May 1989, doi: 10.1016/0375-9601(89)90912-2.

[7] S. L. McCall, A. F. J. Levi, R. E. Slusher, S. J. Pearton, and R. A. Logan, "Whispering-gallery mode microdisk lasers," *Appl. Phys. Lett.*, vol. 60, no. 3, pp. 289–291, Jan. 1992, doi: 10.1063/1.106688.

[8] R. W. Boyd, *Nonlinear Optics*. Academic Press, 2020.

[9] S. M. Spillane, T. J. Kippenberg, and K. J. Vahala, "Ultralow-threshold Raman laser using a spherical dielectric microcavity," *Nature*, vol. 415, no. 6872, Art. no. 6872, Feb. 2002, doi: 10.1038/415621a.

[10] T. J. Kippenberg, S. M. Spillane, D. K. Armani, and K. J. Vahala, "Ultralow-threshold microcavity Raman laser on a microelectronic chip," *Opt. Lett., OL*, vol. 29, no. 11, pp. 1224–1226, Jun. 2004, doi: 10.1364/OL.29.001224.

[11] A. M. Armani, R. P. Kulkarni, S. E. Fraser, R. C. Flagan, and K. J. Vahala, "Label-Free, Single-Molecule Detection with Optical Microcavities," *Science*, vol. 317, no. 5839, pp. 783–787, Aug. 2007, doi: 10.1126/science.1145002.

[12] D. K. Armani, T. J. Kippenberg, S. M. Spillane, and K. J. Vahala, "Ultra-high-Q toroid microcavity on a chip," *Nature*, vol. 421, no. 6926, pp. 925–928, Feb. 2003, doi: 10.1038/nature01371.

[13] K. J. Vahala, "Optical microcavities," *Nature*, vol. 424, pp. 839–846, Aug. 2003, doi: 10.1038/nature01939.

[14] H. Tazawa and W. H. Steier, "Bandwidth of linearized ring resonator assisted Mach-Zehnder modulator," *IEEE Photonics Technology Letters*, vol. 17, no. 9, pp. 1851–1853, Sep. 2005, doi: 10.1109/LPT.2005.853522.

[15] X. Xiao *et al.*, "25 Gbit/s silicon microring modulator based on misalignment-tolerant interleaved PN junctions," *Opt. Express, OE*, vol. 20, no. 3, pp. 2507–2515, Jan. 2012, doi: 10.1364/OE.20.002507.

[16] B. E. Little, S. T. Chu, W. Pan, and Y. Kokubun, "Microring resonator arrays for VLSI photonics," *IEEE Photonics Technology Letters*, vol. 12, no. 3, pp. 323–325, Mar. 2000, doi: 10.1109/68.826928.

[17] T. J. A. Kippenberg, "Nonlinear Optics in Ultra-high Q Whispering-Gallery Optical Microcavities," phd, California Institute of Technology, 2004. Accessed: Jun. 10, 2019. [Online]. Available: http://resolver.caltech.edu/CaltechETD:etd-06072004-085555

[18] H. Rokhsari and K. J. Vahala, “Ultralow Loss, High Q, Four Port Resonant Couplers for Quantum Optics and Photonics,” *Phys. Rev. Lett.*, vol. 92, no. 25, p. 253905, Jun. 2004, doi: 10.1103/PhysRevLett.92.253905.
[19] F. Vollmer, D. Braun, A. Libchaber, M. Khoshsima, I. Teraoka, and S. Arnold, “Protein detection by optical shift of a resonant microcavity,” *Appl. Phys. Lett.*, vol. 80, no. 21, pp. 4057–4059, May 2002, doi: 10.1063/1.1482797.
[20] S. Arnold, M. Khoshsima, I. Teraoka, S. Holler, and F. Vollmer, “Shift of whispering-gallery modes in microspheres by protein adsorption,” *Optics Letters*, vol. 28, no. 4, p. 272, Feb. 2003, doi: 10.1364/OL.28.000272.
[21] T. Lu *et al.*, “High sensitivity nanoparticle detection using optical microcavities,” *Proceedings of the National Academy of Sciences*, vol. 108, no. 15, pp. 5976–5979, Apr. 2011, doi: 10.1073/pnas.1017962108.
[22] J. Su, “Label-Free Detection of Single Biological Molecules Using Microtoroid Optical Resonators,” Ph.D., California Institute of Technology, United States -- California. Accessed: Apr. 10, 2022. [Online]. Available: https://www.proquest.com/docview/1695273069/abstract/811990309FFB439EPQ/1
[23] C. Li, L. Chen, E. McLeod, and J. Su, “Dark mode plasmonic optical microcavity biochemical sensor,” *Photon. Res.*, vol. 7, no. 8, p. 939, Aug. 2019, doi: 10.1364/PRJ.7.000939.
[24] L. Chen, C. Li, Y.-M. Liu, J. Su, and E. McLeod, “Simulating robust far-field coupling to traveling waves in large three-dimensional nanostructured high-Q microresonators,” *Photon. Res.*, vol. 7, no. 9, p. 967, Sep. 2019, doi: 10.1364/PRJ.7.000967.
[25] L. Chen, C. Li, Y. Liu, J. Su, and E. McLeod, “Three-Dimensional Simulation of Particle-Induced Mode Splitting in Large Toroidal Microresonators,” *Sensors*, vol. 20, no. 18, Art. no. 18, Jan. 2020, doi: 10.3390/s20185420.
[26] C. Li *et al.*, “Part-per-trillion trace selective gas detection using frequency locked whispering gallery mode microtoroids,” Mar. 2022, doi: 10.26434/chemrxiv-2022-606xv.
[27] M. L. Gorodetsky, A. A. Savchenkov, and V. S. Ilchenko, “Ultimate Q of optical microsphere resonators,” *Opt. Lett., OL*, vol. 21, no. 7, pp. 453–455, Apr. 1996, doi: 10.1364/OL.21.000453.
[28] J. Su, “Label-Free Single Exosome Detection Using Frequency-Locked Microtoroid Optical Resonators,” *ACS Photonics*, vol. 2, no. 9, pp. 1241–1245, Sep. 2015, doi: 10.1021/acsphotonics.5b00142.
[29] J. Su, “Label-Free Biological and Chemical Sensing Using Whispering Gallery Mode Optical Resonators: Past, Present, and Future,” *Sensors*, vol. 17, no. 3, p. 540, Mar. 2017, doi: 10.3390/s17030540.
[30] J. Su, A. F. Goldberg, and B. M. Stoltz, “Label-free detection of single nanoparticles and biological molecules using microtoroid optical resonators,” *Light: Science & Applications*, vol. 5, no. 1, p. e16001, Jan. 2016, doi: 10.1038/lsa.2016.1.
[31] L. Novotny and B. Hecht, *Principles of Nano-Optics*. Cambridge University Press, 2012.
[32] B. Min, L. Yang, and K. Vahala, “Perturbative analytic theory of an ultrahigh- Q toroidal microcavity,” *Physical Review A*, vol. 76, no. 1, p. 013823, Jul. 2007, doi: 10.1103/PhysRevA.76.013823.
[33] B. Lamouroux, B. Prade, and J. Y. Vinet, “Field Deformation on a Bent Step Index Fibre,” *Journal of Modern Optics*, vol. 38, no. 4, pp. 761–775, Apr. 1991, doi: 10.1080/09500349114550751.
[34] S. J. Garth, “Modes on a bent optical waveguide,” *IEE Proceedings J (Optoelectronics)*, vol. 134, no. 4, pp. 221–229, Aug. 1987, doi: 10.1049/ip-j.1987.0039.
[35] “Using Perfectly Matched Layers and Scattering Boundary Conditions for Wave Electromagnetics Problems,” *COMSOL*. https://www.comsol.com/blogs/using-perfectly-matched-layers-and-scattering-boundary-conditions-for-wave-electromagnetics-problems/?setlang=1 (accessed Mar. 04, 2022).

[36] B. E. Little, S. T. Chu, H. A. Haus, J. Foresi, and J.- Laine, “Microring resonator channel dropping filters,” *Journal of Lightwave Technology*, vol. 15, no. 6, pp. 998–1005, Jun. 1997, doi: 10.1109/50.588673.
[37] J. Zhu *et al.*, “On-chip single nanoparticle detection and sizing by mode splitting in an ultrahigh-Q microresonator,” *Nature photonics*, vol. 4, no. 1, p. 46, 2010.
[38] J. Su, A. F. Goldberg, and B. M. Stoltz, “Label-free detection of single nanoparticles and biological molecules using microtoroid optical resonators,” *Light: Science & Applications*, vol. 5, no. 1, p. e16001, Jan. 2016, doi: 10.1038/lsa.2016.1.
[39] J. D. Swaim, J. Knittel, and W. P. Bowen, “Detection limits in whispering gallery biosensors with plasmonic enhancement,” *Appl. Phys. Lett.*, vol. 99, no. 24, p. 243109, Dec. 2011, doi: 10.1063/1.3669398.
[40] F. Vollmer and L. Yang, “Review Label-free detection with high-Q microcavities: a review of biosensing mechanisms for integrated devices,” *Nanophotonics*, vol. 1, no. 3–4, pp. 267–291, 2012, doi: 10.1515/nanoph-2012-0021.
[41] Y. Zhi, X.-C. Yu, Q. Gong, L. Yang, and Y.-F. Xiao, “Single Nanoparticle Detection Using Optical Microcavities,” *Advanced Materials*, vol. 29, no. 12, p. 1604920, 2017, doi: 10.1002/adma.201604920.
[42] M. R. Foreman, J. D. Swaim, and F. Vollmer, “Whispering gallery mode sensors,” *Advances in Optics and Photonics*, vol. 7, no. 2, p. 168, Jun. 2015, doi: 10.1364/AOP.7.000168.
[43] F. Vollmer, S. Arnold, D. Braun, I. Teraoka, and A. Libchaber, “Multiplexed DNA Quantification by Spectroscopic Shift of Two Microsphere Cavities,” *Biophys J*, vol. 85, no. 3, pp. 1974–1979, Sep. 2003.
[44] M. D. Baaske, M. R. Foreman, and F. Vollmer, “Single-molecule nucleic acid interactions monitored on a label-free microcavity biosensor platform,” *Nature Nanotechnology*, vol. 9, no. 11, pp. 933–939, Nov. 2014, doi: 10.1038/nnano.2014.180.
[45] S. I. Shopova, R. Rajmangal, S. Holler, and S. Arnold, “Plasmonic enhancement of a whispering-gallery-mode biosensor for single nanoparticle detection,” *Appl. Phys. Lett.*, vol. 98, no. 24, p. 243104, Jun. 2011, doi: 10.1063/1.3599584.
[46] Y. Gao, N. Zhou, Z. Shi, X. Guo, and L. Tong, “Dark dimer mode excitation and strong coupling with a nanorod dipole,” *Photon. Res., PRJ*, vol. 6, no. 9, pp. 887–892, Sep. 2018, doi: 10.1364/PRJ.6.000887.
[47] T.-S. Deng, J. Parker, Y. Yifat, N. Shepherd, and N. F. Scherer, “Dark Plasmon Modes in Symmetric Gold Nanoparticle Dimers Illuminated by Focused Cylindrical Vector Beams,” *J. Phys. Chem. C*, vol. 122, no. 48, pp. 27662–27672, Dec. 2018, doi: 10.1021/acs.jpcc.8b10415.
[48] D. E. Gómez, Z. Q. Teo, M. Altissimo, T. J. Davis, S. Earl, and A. Roberts, “The Dark Side of Plasmonics,” *Nano Letters*, vol. 13, no. 8, pp. 3722–3728, Aug. 2013, doi: 10.1021/nl401656e.
[49] D. E. Gómez, K. C. Vernon, and T. J. Davis, “Symmetry effects on the optical coupling between plasmonic nanoparticles with applications to hierarchical structures,” *Physical Review B*, vol. 81, no. 7, Feb. 2010, doi: 10.1103/PhysRevB.81.075414.
[50] J.-S. Huang *et al.*, “Mode Imaging and Selection in Strongly Coupled Nanoantennas,” *Nano Letters*, vol. 10, no. 6, pp. 2105–2110, Jun. 2010, doi: 10.1021/nl100614p.
[51] A. Kaplan *et al.*, “Finite element simulation of a perturbed axial-symmetric whispering-gallery mode and its use for intensity enhancement with a nanoparticle coupled to a microtoroid,” *Opt. Express, OE*, vol. 21, no. 12, pp. 14169–14180, Jun. 2013, doi: 10.1364/OE.21.014169.
[52] R. A. Waldron, “Perturbation theory of resonant cavities,” *Proceedings of the IEE - Part C: Monographs*, vol. 107, no. 12, pp. 272–274, Sep. 1960, doi: 10.1049/pi-c.1960.0041.
[53] H. A. Haus, *Waves and fields in optoelectronics*. Prentice-Hall , 1984. Accessed: Feb. 13, 2019. [Online]. Available: http://dl.merc.ac.ir/handle/Hannan/4099
[54] H. Chen, L. Shao, Q. Li, and J. Wang, “Gold nanorods and their plasmonic properties,” *Chemical Society Reviews*, vol. 42, no. 7, pp. 2679–2724, 2013, doi: 10.1039/C2CS35367A.

[55] D. P. Sprünken *et al.*, “Influence of the Local Environment on Determining Aspect-Ratio Distributions of Gold Nanorods in Solution Using Gans Theory,” *The Journal of Physical Chemistry C*, vol. 111, no. 39, pp. 14299–14306, Oct. 2007, doi: 10.1021/jp074500r.
[56] C. F. Bohren and D. R. Huffman, *Absorption and Scattering of Light by Small Particles*. John Wiley & Sons, 2008.
[57] S. W. Prescott and P. Mulvaney, “Gold nanorod extinction spectra,” *Journal of Applied Physics*, vol. 99, no. 12, p. 123504, Jun. 2006, doi: 10.1063/1.2203212.
[58] F. Ruesink, H. M. Doeleman, E. Verhagen, and A. F. Koenderink, “Controlling nanoantenna polarizability through backaction via a single cavity mode,” *Physical Review Letters*, vol. 120, no. 20, May 2018, doi: 10.1103/PhysRevLett.120.206101.
[59] L. Novotny, “Effective Wavelength Scaling for Optical Antennas,” *Physical Review Letters*, vol. 98, no. 26, Jun. 2007, doi: 10.1103/PhysRevLett.98.266802.
[60] V. R. Dantham, S. Holler, C. Barbre, D. Keng, V. Kolchenko, and S. Arnold, “Label-Free Detection of Single Protein Using a Nanoplasmonic-Photonic Hybrid Microcavity,” *Nano Letters*, vol. 13, no. 7, pp. 3347–3351, Jul. 2013, doi: 10.1021/nl401633y.
[61] Wonjoo Suh, Zheng Wang, and Shanhui Fan, “Temporal coupled-mode theory and the presence of non-orthogonal modes in lossless multimode cavities,” *IEEE Journal of Quantum Electronics*, vol. 40, no. 10, pp. 1511–1518, Oct. 2004, doi: 10.1109/JQE.2004.834773.
[62] A. Yariv, “Universal relations for coupling of optical power between microresonators and dielectric waveguides,” *Electronics Letters*, vol. 36, no. 4, p. 321, 2000, doi: 10.1049/el:20000340.
[63] P. B. Johnson and R. W. Christy, “Optical Constants of the Noble Metals,” *Phys. Rev. B*, vol. 6, no. 12, pp. 4370–4379, Dec. 1972, doi: 10.1103/PhysRevB.6.4370.
[64] M. Oxborrow, “Traceable 2-D Finite-Element Simulation of the Whispering-Gallery Modes of Axisymmetric Electromagnetic Resonators,” *IEEE Transactions on Microwave Theory and Techniques*, vol. 55, no. 6, pp. 1209–1218, Jun. 2007, doi: 10.1109/TMTT.2007.897850.
[65] J.-P. Berenger, “A perfectly matched layer for the absorption of electromagnetic waves,” *Journal of Computational Physics*, vol. 114, no. 2, pp. 185–200, Oct. 1994, doi: 10.1006/jcph.1994.1159.
[66] M. Oxborrow, “Configuration of COMSOL Multiphysics for simulating axisymmetric dielectric resonators: explicit weak-form expressions axisymmetric electromagnetic resonators.” http://resource.npl.co.uk/docs/science_technology/time_frequency/mwave_standards/axisymmetric/comsol_config.pdf
[67] J. Zhu *et al.*, “On-chip single nanoparticle detection and sizing by mode splitting in an ultrahigh-*Q* microresonator,” *Nature Photonics*, vol. 4, no. 1, pp. 46–49, Jan. 2010, doi: 10.1038/nphoton.2009.237.
[68] J. Alegret, T. Rindzevicius, T. Pakizeh, Y. Alaverdyan, L. Gunnarsson, and M. Käll, “Plasmonic Properties of Silver Trimers with Trigonal Symmetry Fabricated by Electron-Beam Lithography,” *J. Phys. Chem. C*, vol. 112, no. 37, pp. 14313–14317, Sep. 2008, doi: 10.1021/jp804505k.
[69] S. L. Teo *et al.*, “Gold nanoring trimers: a versatile structure for infrared sensing,” *Optics Express*, vol. 18, no. 21, p. 22271, Oct. 2010, doi: 10.1364/OE.18.022271.
[70] T. J. Davis, D. E. Gómez, and K. C. Vernon, “Simple Model for the Hybridization of Surface Plasmon Resonances in Metallic Nanoparticles,” *Nano Lett.*, vol. 10, no. 7, pp. 2618–2625, Jul. 2010, doi: 10.1021/nl101335z.
[71] Funston Alison M., Davis Timothy J., Novo Carolina, and Mulvaney Paul, “Coupling modes of gold trimer superstructures,” *Philosophical Transactions of the Royal Society A: Mathematical, Physical and Engineering Sciences*, vol. 369, no. 1950, pp. 3472–3482, Sep. 2011, doi: 10.1098/rsta.2011.0012.
[72] T. J. Davis, K. C. Vernon, and D. E. Gómez, “Designing plasmonic systems using optical coupling between nanoparticles,” *Physical Review B*, vol. 79, no. 15, Apr. 2009, doi: 10.1103/PhysRevB.79.155423.

[73] A. Ashkin, J. M. Dziedzic, J. E. Bjorkholm, and S. Chu, “Observation of a single-beam gradient force optical trap for dielectric particles,” *Opt. Lett., OL*, vol. 11, no. 5, pp. 288–290, May 1986, doi: 10.1364/OL.11.000288.
[74] J. E. Melzer and E. McLeod, “Fundamental Limits of Optical Tweezer Nanoparticle Manipulation Speeds,” *ACS Nano*, vol. 12, no. 3, pp. 2440–2447, Mar. 2018, doi: 10.1021/acsnano.7b07914.
[75] X. Liu, S. Cheng, H. Liu, S. Hu, D. Zhang, and H. Ning, “A Survey on Gas Sensing Technology,” *Sensors*, vol. 12, no. 7, Art. no. 7, Jul. 2012, doi: 10.3390/s120709635.
[76] H. Nazemi, A. Joseph, J. Park, and A. Emadi, “Advanced Micro- and Nano-Gas Sensor Technology: A Review,” *Sensors*, vol. 19, no. 6, Art. no. 6, Jan. 2019, doi: 10.3390/s19061285.
[77] D. Kwak, Y. Lei, and R. Maric, “Ammonia gas sensors: A comprehensive review,” *Talanta*, vol. 204, pp. 713–730, Nov. 2019, doi: 10.1016/j.talanta.2019.06.034.
[78] Z. Yuan, R. Li, F. Meng, J. Zhang, K. Zuo, and E. Han, “Approaches to Enhancing Gas Sensing Properties: A Review,” *Sensors*, vol. 19, no. 7, Art. no. 7, Jan. 2019, doi: 10.3390/s19071495.
[79] T. Han, A. Nag, S. Chandra Mukhopadhyay, and Y. Xu, “Carbon nanotubes and its gas-sensing applications: A review,” *Sensors and Actuators A: Physical*, vol. 291, pp. 107–143, Jun. 2019, doi: 10.1016/j.sna.2019.03.053.
[80] G. Chen, T. M. Paronyan, E. M. Pigos, and A. R. Harutyunyan, “Enhanced gas sensing in pristine carbon nanotubes under continuous ultraviolet light illumination,” *Sci Rep*, vol. 2, no. 1, p. 343, Dec. 2012, doi: 10.1038/srep00343.
[81] D. J. Buckley, N. C. G. Black, E. G. Castanon, C. Melios, M. Hardman, and O. Kazakova, “Frontiers of graphene and 2D material-based gas sensors for environmental monitoring,” *2D Mater.*, vol. 7, no. 3, p. 032002, Jul. 2020, doi: 10.1088/2053-1583/ab7bc5.
[82] J. Su, A. F. Goldberg, and B. M. Stoltz, “Label-free detection of single nanoparticles and biological molecules using microtoroid optical resonators,” *Light: Science & Applications*, vol. 5, no. 1, p. e16001, Jan. 2016, doi: 10.1038/lsa.2016.1.
[83] X. Jiang, A. J. Qavi, S. H. Huang, and L. Yang, “Whispering gallery microsensors: a review,” *Matter*, vol. 3, no. 2, pp. 371–392, Aug. 2020, doi: 10.1016/j.matt.2020.07.008.
[84] Y. Sun and X. Fan, “Analysis of ring resonators for chemical vapor sensor development,” *Opt. Express*, vol. 16, no. 14, p. 10254, Jul. 2008, doi: 10.1364/OE.16.010254.
[85] M. S. Luchansky and R. C. Bailey, “High- *Q* Optical Sensors for Chemical and Biological Analysis,” *Anal. Chem.*, vol. 84, no. 2, pp. 793–821, Jan. 2012, doi: 10.1021/ac2029024.
[86] V. M. N. Passaro, F. Dell’Olio, and F. De Leonardis, “Ammonia Optical Sensing by Microring Resonators,” *Sensors*, vol. 7, no. 11, pp. 2741–2749, Nov. 2007, doi: 10.3390/s7112741.
[87] G. C. Righini *et al.*, “Advanced Sensing by WGM Microresonators,” in *Advanced Photonics 2017 (IPR, NOMA, Sensors, Networks, SPPCom, PS)*, New Orleans, Louisiana, 2017, p. SeM2E.5. doi: 10.1364/SENSORS.2017.SeM2E.5.
[88] C. Lemieux-Leduc, R. Guertin, M.-A. Bianki, and Y.-A. Peter, “All-polymer whispering gallery mode resonators for gas sensing,” *Opt. Express*, vol. 29, no. 6, p. 8685, Mar. 2021, doi: 10.1364/OE.417703.
[89] J. Fiandor, M. T. García-López, F. G. D. L. Heras, and P. P. Méndez-Castrillón, “A Facile Regioselective 1-O-Deacylation of Peracylated Glycopyranoses,” *Synthesis*, vol. 1985, no. 12, pp. 1121–1123, 1985, doi: 10.1055/s-1985-31446.
[90] H. Wang *et al.*, “Selective and facile deacetylation of pentacyclic triterpenoid under methanolic ammonia condition and unambiguous NMR analysis,” *Chinese Chemical Letters*, vol. 31, no. 2, pp. 333–336, Feb. 2020, doi: 10.1016/j.cclet.2019.06.007.
[91] K. Z. Gaca, J. A. Parkinson, L. Lue, and J. Sefcik, “Equilibrium Speciation in Moderately Concentrated Formaldehyde–Methanol–Water Solutions Investigated Using ^{13}C and ^{1}H Nuclear Magnetic Resonance Spectroscopy,” *Ind. Eng. Chem. Res.*, vol. 53, no. 22, pp. 9262–9271, Jun. 2014, doi: 10.1021/ie403252x.
[92] K. K. Barakoti, P. Subedi, F. Chalyavi, S. Gutierrez-Portocarrero, M. J. Tucker, and M. A. Alpuche-Aviles, “Formaldehyde Analysis in Non-Aqueous Methanol Solutions by Infrared

Spectroscopy and Electrospray Ionization," *Frontiers in Chemistry*, vol. 9, 2021, Accessed: Mar. 15, 2022. [Online]. Available: https://www.frontiersin.org/article/10.3389/fchem.2021.678112
[93] R. Roto, A. Rianjanu, I. A. Fatyadi, A. Kusumaatmaja, and K. Triyana, "Enhanced sensitivity and selectivity of ammonia sensing by QCM modified with boric acid-doped PVAc nanofiber," *Sensors and Actuators A: Physical*, vol. 304, p. 111902, Apr. 2020, doi: 10.1016/j.sna.2020.111902.
[94] L. Aksornneam, P. Kanatharana, P. Thavarungkul, and C. Thammakhet, "5-Aminofluorescein doped polyvinyl alcohol film for the detection of formaldehyde in vegetables and seafood," *Anal. Methods*, vol. 8, no. 6, pp. 1249–1256, Feb. 2016, doi: 10.1039/C5AY02719E.
[95] F. Behrends, H. Wagner, A. Studer, O. Niehaus, R. Pöttgen, and H. Eckert, "Polynitroxides from Alkoxyamine Monomers: Structural and Kinetic Investigations by Solid State NMR," *Macromolecules*, vol. 46, no. 7, pp. 2553–2561, Apr. 2013, doi: 10.1021/ma400351q.
[96] J. C. Grim *et al.*, "A Reversible and Repeatable Thiol–Ene Bioconjugation for Dynamic Patterning of Signaling Proteins in Hydrogels," *ACS Cent. Sci.*, vol. 4, no. 7, pp. 909–916, Jul. 2018, doi: 10.1021/acscentsci.8b00325.
[97] "The dn/dc value for poly(vinyl acetate) in THF at 25 oC was obtained from American Polymer Standards Corporation." http://www.ampolymer.com/dn-dc.html (accessed Mar. 14, 2022).
[98] P. T. Charles, V. R. Stubbs, C. M. Soto, B. D. Martin, B. J. White, and C. R. Taitt, "Reduction of Non-Specific Protein Adsorption Using Poly(ethylene) Glycol (PEG) Modified Polyacrylate Hydrogels In Immunoassays for Staphylococcal Enterotoxin B Detection," *Sensors (Basel)*, vol. 9, no. 1, pp. 645–655, Jan. 2009, doi: 10.3390/s90100645.
[99] N. Wisniewski and M. Reichert, "Methods for reducing biosensor membrane biofouling," *Colloids and Surfaces B: Biointerfaces*, vol. 18, no. 3, pp. 197–219, Oct. 2000, doi: 10.1016/S0927-7765(99)00148-4.
[100] F. J. Xu *et al.*, "Spatially well-defined binary brushes of poly(ethylene glycol)s for micropatterning of active proteins on anti-fouling surfaces," *Biosensors and Bioelectronics*, vol. 24, no. 4, pp. 773–780, Dec. 2008, doi: 10.1016/j.bios.2008.06.055.
[101] K. Glosz, A. Stolarczyk, and T. Jarosz, "Siloxanes—Versatile Materials for Surface Functionalisation and Graft Copolymers," *International Journal of Molecular Sciences*, vol. 21, no. 17, Art. no. 17, Jan. 2020, doi: 10.3390/ijms21176387.
[102] A. Debuigne, J.-R. Caille, C. Detrembleur, and R. Jérôme, "Effective Cobalt Mediation of the Radical Polymerization of Vinyl Acetate in Suspension," *Angewandte Chemie International Edition*, vol. 44, no. 22, pp. 3439–3442, 2005, doi: 10.1002/anie.200500112.
[103] A. Debuigne, J.-R. Caille, N. Willet, and R. Jérôme, "Synthesis of Poly(vinyl acetate) and Poly(vinyl alcohol) Containing Block Copolymers by Combination of Cobalt-Mediated Radical Polymerization and ATRP," *Macromolecules*, vol. 38, no. 23, pp. 9488–9496, Nov. 2005, doi: 10.1021/ma051246x.
[104] E. Ozgur *et al.*, "Ultrasensitive Detection of Human Chorionic Gonadotropin Using Frequency Locked Microtoroid Optical Resonators," *Anal. Chem.*, vol. 91, no. 18, pp. 11872–11878, Sep. 2019, doi: 10.1021/acs.analchem.9b02630.
[105] J.-B. Zhang and K. Huang, "Solubilities of Ammonia in Polyethylene Glycols at 298.2–353.2 K and 0–200 kPa," *J. Chem. Eng. Data*, vol. 65, no. 1, pp. 97–105, Jan. 2020, doi: 10.1021/acs.jced.9b00779.
[106] C. Hildebrandt, L. Joos, R. Saedler, and G. Winter, "The 'New Polyethylene Glycol Dilemma': Polyethylene Glycol Impurities and Their Paradox Role in mAb Crystallization," *Journal of Pharmaceutical Sciences*, vol. 104, no. 6, pp. 1938–1945, Jun. 2015, doi: 10.1002/jps.24424.
[107] E. Bálint, Á. Tajti, N. Tóth, and G. Keglevich, "Continuous Flow Alcoholysis of Dialkyl H-Phosphonates with Aliphatic Alcohols," *Molecules*, vol. 23, no. 7, Art. no. 7, Jul. 2018, doi: 10.3390/molecules23071618.

[108] Daniel. MacDougall, W. B. Crummett, and . et al., “Guidelines for data acquisition and data quality evaluation in environmental chemistry,” *Anal. Chem.*, vol. 52, no. 14, pp. 2242–2249, Dec. 1980, doi: 10.1021/ac50064a004.
[109] Z. Ma *et al.*, “TCR Triggering by pMHC Ligands Tethered on Surfaces via Poly(Ethylene Glycol) Depends on Polymer Length,” *PLoS ONE*, vol. 9, no. 11, p. e112292, Nov. 2014, doi: 10.1371/journal.pone.0112292.
[110] J. McKenna *et al.*, “Detection of chemical warfare agent simulants and hydrolysis products in biological samples by paper spray mass spectrometry,” *Analyst*, vol. 142, no. 9, pp. 1442–1451, 2017, doi: 10.1039/C7AN00144D.
[111] A. R. Hopkins and N. S. Lewis, “Detection and Classification Characteristics of Arrays of Carbon Black/Organic Polymer Composite Chemiresistive Vapor Detectors for the Nerve Agent Simulants Dimethylmethylphosphonate and Diisopropylmethylphosponate,” *Anal. Chem.*, vol. 73, no. 5, pp. 884–892, Mar. 2001, doi: 10.1021/ac0008439.
[112] G. Chen, T. M. Paronyan, and A. R. Harutyunyan, “Sub-ppt gas detection with pristine graphene,” *Appl. Phys. Lett.*, vol. 101, no. 5, p. 053119, Jul. 2012, doi: 10.1063/1.4742327.
[113] A. K. Mallik, G. Farrell, D. Liu, V. Kavungal, Q. Wu, and Y. Semenova, “Silica Gel Coated Spherical Micro resonator for Ultra-High Sensitivity Detection of Ammonia Gas Concentration in Air,” *Sci Rep*, vol. 8, no. 1, p. 1620, Jan. 2018, doi: 10.1038/s41598-018-20025-9.
[114] A. Pathak, S. K. Mishra, and B. D. Gupta, “Fiber-optic ammonia sensor using Ag/SnO_2 thin films: optimization of thickness of SnO_2 film using electric field distribution and reaction factor,” *Appl. Opt., AO*, vol. 54, no. 29, pp. 8712–8721, Oct. 2015, doi: 10.1364/AO.54.008712.
[115] B. Yao *et al.*, “Graphene-Enhanced Brillouin Optomechanical Microresonator for Ultrasensitive Gas Detection,” *Nano Lett.*, vol. 17, no. 8, pp. 4996–5002, Aug. 2017, doi: 10.1021/acs.nanolett.7b02176.
[116] H. Xie, C. Sheng, X. Chen, X. Wang, Z. Li, and J. Zhou, “Multi-wall carbon nanotube gas sensors modified with amino-group to detect low concentration of formaldehyde,” *Sensors and Actuators B: Chemical*, vol. 168, pp. 34–38, Jun. 2012, doi: 10.1016/j.snb.2011.12.112.
[117] I. Castro-Hurtado, J. Herrán, G. Ga Mandayo, and E. Castaño, “SnO2-nanowires grown by catalytic oxidation of tin sputtered thin films for formaldehyde detection,” *Thin Solid Films*, vol. 520, no. 14, pp. 4792–4796, May 2012, doi: 10.1016/j.tsf.2011.10.140.
[118] J. Su, “Label-Free Single Exosome Detection Using Frequency-Locked Microtoroid Optical Resonators,” *ACS Photonics*, vol. 2, no. 9, pp. 1241–1245, Sep. 2015, doi: 10.1021/acsphotonics.5b00142.
[119] Z. Ding *et al.*, “Distributed Optical Fiber Sensors Based on Optical Frequency Domain Reflectometry: A review,” *Sensors*, vol. 18, no. 4, Art. no. 4, Apr. 2018, doi: 10.3390/s18041072.
[120] A. J. Hymans and J. Lait, “Analysis of a frequency-modulated continuous-wave ranging system,” *Proceedings of the IEE - Part B: Electronic and Communication Engineering*, vol. 107, no. 34, pp. 365–372, Jul. 1960, doi: 10.1049/pi-b-2.1960.0130.
[121] Y. Du *et al.*, “Cryogenic Temperature Measurement Using Rayleigh Backscattering Spectra Shift by OFDR,” *IEEE Photonics Technology Letters*, vol. 26, no. 11, pp. 1150–1153, Jun. 2014, doi: 10.1109/LPT.2014.2317702.
[122] P. Lu *et al.*, “Distributed optical fiber sensing: Review and perspective,” *Applied Physics Reviews*, vol. 6, no. 4, p. 041302, Sep. 2019, doi: 10.1063/1.5113955.
[123] Z. Zhu, D. Ba, L. Liu, L. Qiu, and Y. Dong, “Temperature-compensated distributed refractive index sensor based on an etched multi-core fiber in optical frequency domain reflectometry,” *Opt. Lett., OL*, vol. 46, no. 17, pp. 4308–4311, Sep. 2021, doi: 10.1364/OL.432405.
[124] X. Lou, Y. Wang, and Y. Dong, “Multipoint dispersion spectroscopic gas sensing by optical FMCW interferometry,” *Opt. Lett., OL*, vol. 46, no. 23, pp. 5950–5953, Dec. 2021, doi: 10.1364/OL.443126.

[125] M. Froggatt and J. Moore, "High-spatial-resolution distributed strain measurement in optical fiber with Rayleigh scatter," *Appl. Opt., AO*, vol. 37, no. 10, pp. 1735–1740, Apr. 1998, doi: 10.1364/AO.37.001735.
[126] S. Loranger, M. Gagné, V. Lambin Iezzi, and R. Kashyap, "Rayleigh scatter based order of magnitude increase in distributed temperature and strain sensing by simple UV exposure of optical fibre," *Sci. Rep.*, vol. 5, Jun. 2015, doi: 10.1038/srep11177.
[127] S. T. Kreger, D. K. Gifford, M. E. Froggatt, B. J. Soller, and M. S. Wolfe, "High Resolution Distributed Strain or Temperature Measurements in Single-and Multi-mode Fiber Using Swept-Wavelength Interferometry," in *Optical Fiber Sensors (2006), paper ThE42*, Oct. 2006, p. ThE42. doi: 10.1364/OFS.2006.ThE42.
[128] J. Cui, S. Zhao, D. Yang, and Z. Ding, "Investigation of the interpolation method to improve the distributed strain measurement accuracy in optical frequency domain reflectometry systems," *Appl. Opt.*, vol. 57, no. 6, p. 1424, Feb. 2018, doi: 10.1364/AO.57.001424.
[129] X. Wang, W. Li, L. Chen, and X. Bao, "Thermal and mechanical properties of tapered single mode fiber measured by OFDR and its application for high-sensitivity force measurement," *Opt. Express, OE*, vol. 20, no. 14, pp. 14779–14788, Jul. 2012, doi: 10.1364/OE.20.014779.
[130] K. Yüksel, M. Wuilpart, and P. Mégret, "Analysis and suppression of nonlinear frequency modulation in an optical frequency-domain reflectometer," *Opt. Express, OE*, vol. 17, no. 7, pp. 5845–5851, Mar. 2009, doi: 10.1364/OE.17.005845.
[131] E. D. Moore and R. R. McLeod, "Correction of sampling errors due to laser tuning rate fluctuations in swept-wavelength interferometry," *Opt. Express, OE*, vol. 16, no. 17, pp. 13139–13149, Aug. 2008, doi: 10.1364/OE.16.013139.
[132] "Thorlabs - SM600 Single Mode Optical Fiber, 633 - 780 nm, Ø125 µm Cladding." https://www.thorlabs.com/thorproduct.cfm?partnumber=SM600 (accessed Apr. 05, 2022).